

UC Riverside

UC Riverside Electronic Theses and Dissertations

Title

Black Hole Feedback in Dwarf Galaxy Evolution

Permalink

<https://escholarship.org/uc/item/8z2387n2>

Author

King, Christina Manzano

Publication Date

2020

Peer reviewed|Thesis/dissertation

UNIVERSITY OF CALIFORNIA
RIVERSIDE

Black Hole Feedback in Dwarf Galaxy Evolution

A Dissertation submitted in partial satisfaction
of the requirements for the degree of

Doctor of Philosophy

in

Physics

by

Christina Manzano King

September 2020

Dissertation Committee:

Prof. Gabriela Canalizo, Chairperson
Prof. Frederick Hamann
Prof. Brian Siana

Copyright by
Christina Manzano King
2020

The Dissertation of Christina Manzano King is approved:

Committee Chairperson

University of California, Riverside

Acknowledgments

I would like to express my sincere gratitude to my advisor Prof. Canalizo for her continued patience and hard work mentoring me. I would also like to thank the rest of my thesis committee for their insightful comments, my group for their continued help throughout this project, and my friends in POWUR who held me up along the way. To those defending the sacred: Kū Kia'i Mauna!

I dedicate my work to Jose Lucero Manzano and Valentina Tuazon Manzano, who dreamt that their granddaughter would earn the family's first doctorate degree, and to Ruena Manzano, who supports me in all I do.

ABSTRACT OF THE DISSERTATION

Black Hole Feedback in Dwarf Galaxy Evolution

by

Christina Manzano King

Doctor of Philosophy, Graduate Program in Physics
University of California, Riverside, September 2020
Prof. Gabriela Canalizo, Chairperson

In a scenario where all galaxies form and evolve with supermassive black holes in their centers, it is thought that these central black holes play a vital role in limiting the growth of massive galaxies. In order to extend our understanding of black hole influence on galaxy evolution into the low mass regime, we collected spatially resolved spectra of 50 nearby ($z < 0.05$) dwarf ($M_{\star} < 10^{10} M_{\odot}$) galaxies, selected from SDSS DR7 and DR 8 followed-up with Keck/LRIS spectroscopy. We study the potential effects of active galactic nuclei (AGN) on galaxy-wide gas kinematics and integrated stellar properties by comparing measurements obtained from 29 galaxies containing AGN, and 21 control galaxies with no optical or infrared signs of AGN. We present the first direct measurements of AGN-driven gas outflows in the low mass regime. We also find a strong association between AGN and disturbed ionized gas kinematics and signs of star formation suppression. Our results provide evidence that AGN can have significant influence on large scale gas motions in their host galaxies and their global stellar populations. AGN feedback appears to be an

important, and perhaps dominant, mechanism that regulates dwarf galaxy evolution, and should be included in realistic galaxy formation models in the low-mass regime.

Contents

List of Figures	3
List of Tables	16
1 Introduction	1
Introduction	1
1.1 Small Scale Problems	2
1.2 An Overview of Baryonic Feedback	5
1.2.1 Stellar feedback	5
1.2.2 AGN feedback	5
1.3 This Work	7
2 Outflows	8
2.1 Introduction	9
2.2 Data	12
2.2.1 Sample Selection	12
2.2.2 Observations and Data Reduction	14
2.3 Analysis	17
2.3.1 Fitting the Stellar Continuum	18
2.3.2 Fitting Emission Lines	19
2.3.3 Detecting Outflows	21
2.3.4 Outflow Velocity	22
2.3.5 Decomposed Flux Ratios	23
2.4 Results	24
2.4.1 Classifying Outflows	24
2.4.2 Integrated Properties of Outflows	26
2.4.3 Spatially Resolved Properties of Outflows	29
2.5 Discussion	31
2.5.1 Ionization by Star Formation vs. AGN	31
2.5.2 Outflow Line Profiles	32
2.5.3 Gas Velocity	36
2.5.4 Feedback	37

2.6	Summary	40
3	Gas Kinematics	45
3.1	Introduction	46
3.2	Data	48
3.3	Analysis	55
3.3.1	Spatially Resolved Spectra	55
3.3.2	Emission Line Fluxes	57
3.3.3	Multi-Component Velocity Measurements	57
3.3.4	Circular Velocity Curves	58
3.4	Results	60
3.4.1	Comparison with NFW	60
3.4.2	Peculiar Gas	66
3.4.3	Star Formation Suppression	70
3.4.4	Environment	73
3.5	Summary	75
4	AGN Impact on Dwarf Galaxy Stellar Populations	81
4.1	Introduction	81
4.2	Data and Analysis	84
4.2.1	Star Formation History	84
4.2.2	Mass Weighted Stellar Ages and Abundances	87
4.3	Results and Discussion	88
4.3.1	Are AGN suppressing star formation in isolated galaxies?	90
4.3.2	The story behind counter-rotation	91
4.3.3	Stellar Activity and Outflows	94
4.4	Summary	95
5	Summary and Conclusions	100
5.1	AGN are able to expel gas from dwarf galaxies	100
5.2	AGN can affect global gas kinematics	101
5.3	AGN with disturbed gas are associated with star formation suppression	102
A		105
A.1	Black Hole Masses	105
A.2	Spatial Properties of Outflows	106
A.3	Inclination Correction	106
A.4	All rotation curves	108
	Bibliography	115

List of Figures

- 1.1 Figure 5 from the [47] Annual Review shows the discrepancy between predicted and observed stellar mass functions. The halo mass function predicted by dark-matter-only simulations is denoted by the thick black line, and the corresponding stellar mass function assuming a constant baryonic fraction and star formation efficiency for each halo ($M_{\star} = \epsilon_{\star} f_b M_{\text{halo}}$) is plotted as a dotted black line. In comparison, the observed stellar mass function of galaxies of [29] and [358] are shown as magenta stars and cyan squares, respectively. The gray shaded region depicts a range of possible faint-end slopes between $\alpha = -1.62$ to -1.32 . Note that the maximum star formation efficiency is reached in galaxies of roughly $10^{11} M_{\odot}$, while star formation becomes increasingly inefficient at the low- and high- mass end of the mass function. 3

2.1	Top: BPT line ratios from the central 0.2 kpc of each galaxy for dwarf galaxies in our sample observed with Keck/LRIS. 29 galaxies with optical signatures of AGN were selected from the samples of RGG13, M14, and S15. The remaining 21 are a control sample composed of star-forming dwarf galaxies. Dwarfs that present signatures of gas outflows are plotted with larger symbols. Bottom: Redshift and stellar mass distribution of our sample of dwarf galaxies. . . .	15
2.2	SDSS color images of the 13 dwarf galaxies with spatially extended outflows. All images were generated using the SDSS DR12 finding chart tool, with the exception of NGC 1569, which is outside of the SDSS footprint. The NGC 1569 thumbnail is a PanSTARS z,g band color image rendered in the Aladin Lite Viewer with a 3' field of view (~ 1 kpc on a side). Each SDSS image is scaled to 10 kpc on a side and the placement of the 1 arcsecond-wide slit is shown in light gray.	16

2.5	Narrow and broad emission line ratios are shown for each galaxy with outflows. The smaller symbols show the position of the bound gas (narrow component in spectrum) for each galaxy, and the larger symbols those of the outflow (broad component). In this paper, each galaxy is classified based on its position of the outflow component in the AGN (pink circles), composite (gray diamonds), or star forming regions (cyan triangles).	25
2.6	Details of the broad component fits to the [O III] doublets of each of the 13 galaxies with outflows are shown. The spectra are extracted from the region within the R_{50} of each galaxy and have all been normalized by the continuum flux just redward of [O III] λ 5007. AGN are grouped in the top figure and star forming galaxies are on the bottom. Average fit parameters, weighted by the luminosity of each narrow [O III] line, are shown in the last panel of each section. Panels shaded in gray are classified as composite and are excluded from the AGN outflow average. Values of v_0 , W_{80} , and v_{out} are listed for each of the 13 galaxies in Table 2.1.	27
2.7	Spatial properties of the AGN-driven outflow in J090613.75+561015.5. The outflow width W_{80} and offset v_0 as defined in Section 2.3.4 as a function of radius are shown in the top two panels, respectively. The ratio of the broad to narrow [O III] flux is shown in the bottom panel.	30

2.8	<p>A comparison between outflow component line profiles extracted from the central ~ 0.4 kpc and ~ 1.5 kpc from the center of J090613.75+561015.5 is shown. We speculate that the central outflow appears blueshifted due to denser material in the center of the galaxy obscuring emission from the redshifted gas escaping the far side of the galaxy. Farther from the center, the outflow profile widens and the velocity offset becomes less pronounced as galactic obscuration fades and both blue- and redshifted portions of the outflow is revealed.</p>	34
2.9	<p>Relation between the velocity measured for the outflows and the modeled escape velocity assuming galaxies live in massive dark matter halos consistent with the cosmological picture of ΛCDM. In all cases, the wind speed is comparable or above that needed to escape the dark matter halo. To guide the eye, the dashed line indicates a 1-to-1 relation.</p>	35
2.10	<p>The $u - r$ model magnitude colors from SDSS DR 8 are plotted against the MPA-JHU stellar mass. The colors are corrected for galactic extinction, following [280] and the contours are from [278]. The photometry for NGC 1569 were measured in GALEX [124] and converted to SDSS $ugriz$ via the Python code pysynphot. The outflow symbol sizes are scaled to the fraction of [O III] flux contained in the outflows.</p>	38

3.1	Top: BPT diagnostic for all 50 galaxies in this sample. The dotted line denotes the [163] classification cutoff, and the solid line is the [165] maximum starburst line. Blue circles indicate isolated galaxies with disturbed gas and with no neighbors of comparable mass (i.e. the neighboring galaxy is at least 0.75 times the stellar mass of the dwarf) within 1.5 Mpc (see Section 3.4.4). Galaxies with counter-rotating stellar and gas components are marked as orange triangles. Bottom: Stacked histograms of redshift and stellar mass of the galaxies presented in this paper. Dark gray represents AGN hosts and light gray represents star forming galaxies.	49
3.2	colour images of all 50 dwarf galaxies in our sample. All images were generated using the SDSS DR12 finding chart tool, with the exception of NGC 1569, which is outside of the SDSS footprint. The NGC 1569 thumbnail (second row, second column) is a PanSTARS z,g band colour image rendered in the Aladin Lite Viewer with a 3' field of view (~ 1 kpc on a side). Each SDSS image is scaled to 10 kpc on a side and the placement of the 1 arcsecond-wide slit is shown in light gray.	50

3.3	Pixel number along the spatial axis is shown on the x axis. The y axis shows the signal to noise ratio of a featureless portion of the spectrum red-ward of [O III] λ 5007. Moving along the slit, we summed pixel rows (black) until the integrated spectrum's signal to noise ratio (green) reached the target S/N (red) or the maximum bin size was reached. The minimum bin size is 3 pixel rows, which sometimes results in even higher S/N. Exposure times for each object were chosen with the intention of obtaining sufficient S/N in the outskirts, so the bin size is dependent on the observational setup used. . . .	56
3.4	Example PPF fits to each of the three spectral sections used to determine velocity curves. Each velocity curve consists of three components: stellar (red), hydrogen (orange), and forbidden (purple, green, and blue).	59
3.5	The object J170639.14+334103.4 was chosen randomly from our sample to provide an example of an orderly rotation curve, with a co-rotating disc of gas and stars. The stellar (gray stars), H β (orange circles) and [O III] (teal circles) velocities are shown as a function of normalized radius, where r_{50} is the r-band Petrosian 50% radius. The dotted black line indicates the expected velocity curve for an NFW profile with concentration parameter $c = 10$. The shaded gray region represents the NFW curve expected from halos with concentration parameter $c = 8 - 15$	61

- 3.6 Four stellar absolute circular velocity curves are shown to demonstrate the variety of inner slopes found in our sample. Two examples of AGN are displayed in the left panels and two star forming galaxies are shown on the right. Dashed black lines and shaded gray regions represent NFW velocity curves corresponding to a halo mass determined by abundance matching, with the MPA-JHU stellar mass as input. Stellar velocity curves showing agreement with the expected NFW profile are shown on the top two panels. The velocity profiles in the bottom panels rise slowly, indicating cored dark matter density profiles. 62
- 3.7 We define Δ_{off} to be the weighted absolute average of the velocity offset between stars and gas, divided by the average absolute stellar velocity. This metric is used to quantify the degree of separation between the stellar and forbidden gas component. Based on the bimodal distribution of Δ_{off} in our sample, we consider galaxies $\Delta_{\text{off}} \geq 0.75$ to have kinematically disturbed gas. 65
- 3.8 Examples of rotation curves where the gas is disturbed in different ways. In some instances, gas is offset from the stars without showing any clear sign of rotation (left). Some AGN have stratified narrow line components, where the Balmer and forbidden lines are kinematically distinct from one another (center). Five galaxies in our sample have gas and stellar discs rotating separately, and sometimes in opposite directions (right). 66

3.9	The rotation curves for five galaxies with counter-rotating gas are shown here. The colours are as in Figure 3.8, and the blue dots in the middle panel indicate gas velocities measured from the [SII] doublet.	69
3.10	Absolute line of sight velocity (v_{los}) measurements that far exceed the expected NFW velocity curves based on their stellar masses indicate overmassive dark matter haloes relative to the measured stellar mass, implying ongoing star formation suppression. Stellar (left), Balmer emission (center) and forbidden emission (right) components are shown for the three galaxies in our sample where this is most apparent. Green curves mark expected NFW velocity curves for galaxies with stellar mass $\log(M_{\star}) = 10.5, 11, \text{ and } 12$ and concentration parameter $c = 10$. Black dotted lines denote the expected NFW velocity curves based on each galaxy’s MPA-JHU stellar mass. All three of these galaxies host AGN, and two have counter-rotating gas components, which lends additional evidence potentially associating AGN with gas depletion and star formation suppression in dwarf galaxies.	71

4.1 The PPXF fit to the integrated spectrum of a galaxy is shown. The fully reduced 2D spectrum is shown in the top panel, with the integrated region highlighted in cyan. The middle panel displays the spectra integrated within the highlighted cyan region (black), superimposed with the best fit stellar (red) and gas (blue) model. Fit residuals are plotted in green. The third panel shows the PPXF solution for across stellar age and metallicity intervals. The regularized map shows the mass fraction of stars falling within each interval, with higher mass fractions in yellow. The bottom panel plots the stellar mass fraction over time, which traces the assembly history of the galaxy. 85

4.2 Top: The stellar mass growth is traced by the cumulative stellar mass fraction over time. SFHs of all galaxies in the sample are shown as faint gray lines and various groups of interest are highlighted in each panel. Top left: The red lines represent the SFHs of six isolated galaxies with AGN. The AGN galaxies with neighbors are indicated by brown lines and the SFHs for the star forming control sample are shown as faint gray lines. Top middle: The five galaxies in our sample with counter-rotating gas are emphasized. SFHs of counter-rotating galaxies that are satellites of massive ($M_{\star} > 10^{11} M_{\odot}$) galaxies are shown as purple dotted lines, while isolated counter-rotating galaxy SFHs are plotted in solid orange. Top right: Galaxies with outflows detected via broadened [O III] components are emphasized. SFHs for galaxies with AGN-driven (pink), star formation-driven (blue), and AGN hosting galaxies with star formation-driven outflows (composite; gray) are shown. Bottom: The stellar mass - metallicity relation for active (blue) and passive (red) galaxies is plotted [236]. In each bottom panel, the integrated stellar metal abundances of the galaxies shown in the corresponding top panel are plotted according to the same color schemes. 89

4.3	The full mass weighted stellar age - stellar metallicity grids for all five counter-rotating galaxies are shown, in order of increasing mass. The three galaxies in the top row are satellites and the two in the bottom are isolated. Each block in the grid is associated with a SSP with the specified stellar age and metallicity. The color scheme represents the mass fraction associated with each SSP, where yellow indicates the largest fraction.	91
A.1	Spatially resolved properties of outflows are presented for the remaining 12 galaxies, as in Fig. 2.7. Consistent with the scheme used throughout this paper, AGN-driven outflows are plotted with pink circles, star forming with cyan triangles, and AGN with SF outflows with black diamonds.	111
A.2	A diagram to illustrate how a disc with thickness c appears as an ellipse when viewed from the inclination angle θ_{inc} . The inclination angle can be estimated by measuring the ellipse semimajor and minor axes a , b and assuming the disc thickness c	111
A.3	Twenty of the 45 galaxies with rotation curves have gas that rotates with the stellar component. The shaded regions denote velocity curves following NFW profiles, assuming concentration parameters between $c = 8, 15$. Galaxies hosting AGN are shown in the top panel and star forming galaxies are in the bottom.	112

A.4	Twenty-five of the 45 galaxies with rotation curves have disturbed gas. See Section 3.4.2 for a discussion on how we classify galaxies as disturbed. Galaxies hosting AGN are shown in the top group and star forming galaxies are in the bottom.	113
A.5	Eight of the 45 galaxies with rotation curves show stratification in their emission lines. See Section 3.4.2 for a discussion on how we identify line stratification. Line of sight velocity gradients are shown for J0811+23 and J0842+03, as they are considered face-on based on their small inclination angles ($\theta < 20^\circ$) and thus are not corrected for inclination (as described in Appendix A.4). Rotational velocity curves (corrected for disc inclination) are shown for all other galaxies in this figure.	114

List of Tables

2.1 Details of fits to spectra extracted within R_{50} of each galaxy, unless otherwise specified. (1) Full SDSS names of all 13 galaxies with extended outflows (2) Redshift (3) Stellar mass reported in the MPA-JHU catalog (4) Halo mass determined via abundance matching using the method described in the text and the stellar mass listed in (2) (5) Mean velocity of the outflow, in km s^{-1} , relative to the center of the narrow component (negative=blueshifted) (6) Width containing 80% of the flux of the outflow component, in km s^{-1} . (7) Outflow velocity defined as $v_{\text{out}} = -v_0 + \frac{W_{80}}{2}$, in km s^{-1} (8) Velocity required to escape the dark matter halo (3) with an NFW profile from $r = 0$, in km s^{-1} (9) Fraction of [O III] flux in the outflow, calculated as the ratio of the flux in the broad component, F_b , to the total flux in broad + narrow components, F_{tot} (10,11) Decomposed BPT classifications for the bound and outflowing gas. In order to optimize S/N, these fits were performed on spectra extracted from customized apertures for each galaxy. 44

3.1 LRIS configuration for each object, using the 1" slit placed along the semimajor axis of each galaxy. For the blue side (LRIS-B), we used the 600 groove mm^{-1} grism blazed at 4000\AA , yielding a dispersion of $0.63\text{\AA pixel}^{-1}$. We used three setups on the red side (LRIS-R):

A: 600 groove mm^{-1} grating blazed at 5000\AA , 5600\AA dichroic, yielding a dispersion of $0.80\text{\AA pixel}^{-1}$

B: 900 groove mm^{-1} grating blazed at 5500\AA , 5600\AA dichroic, yielding a dispersion of $0.53\text{\AA pixel}^{-1}$

C: 1200 groove mm^{-1} grating blazed at 7500\AA , 5000\AA dichroic, yielding a dispersion of $0.40\text{\AA pixel}^{-1}$ 54

3.2	<p>(1) * indicates objects excluded from this study. (2) Redshift is calculated by fits to stellar absorption lines in LRIS spectra using PPXF. (3) Stellar mass reported in the MPA-JHU catalogue. (4) ^b Black hole mass lower limits derived using Eddington Luminosity arguments (M14) ^c Black hole mass estimated using as $M_{BH} \propto R\Delta V^2/G$, where ΔV is measured from broad $H\alpha$, extrapolating the BLR radius – luminosity relation extends into the low mass regime (R13) (5) SDSS Petrosian radius containing 50% of r-band flux, in kiloparsecs. (6) Classification of dominant ionization source based on Gaussian fits to emission lines using the process described in Section 3.3.2. The spectra were extracted from the central 1kpc of each galaxy. (7) Same as (6) but for HeII classification (S15) (8) Number of galaxies with comparable mass within 1.5 Mpc. (9) Classified as disturbed (see Section 3.4.2) (10) Gas is clearly rotating and offset from stellar component. (11) Has an outflow identified by an additional broad component in as defined in Paper I. (12) Narrow emission lines are stratified (see Section 3.4.2)</p>	77
3.3	<p>Seven galaxies in our sample have disturbed gas kinematics and no neighbors of comparable mass within 1.5 Mpc and $\pm 1000 \text{ km s}^{-1}$. Six of them host AGN, two have counter-rotating gas, and four have outflows indicated by broad wings in their [OIII]5007 emission line profiles. $u - r$ colour is based on SDSS cModelMag photometry.</p>	78
4.1	<p>The average integrated mass-weighted stellar age, metal abundance, and formation times for all 50 galaxies.</p>	99

Chapter 1

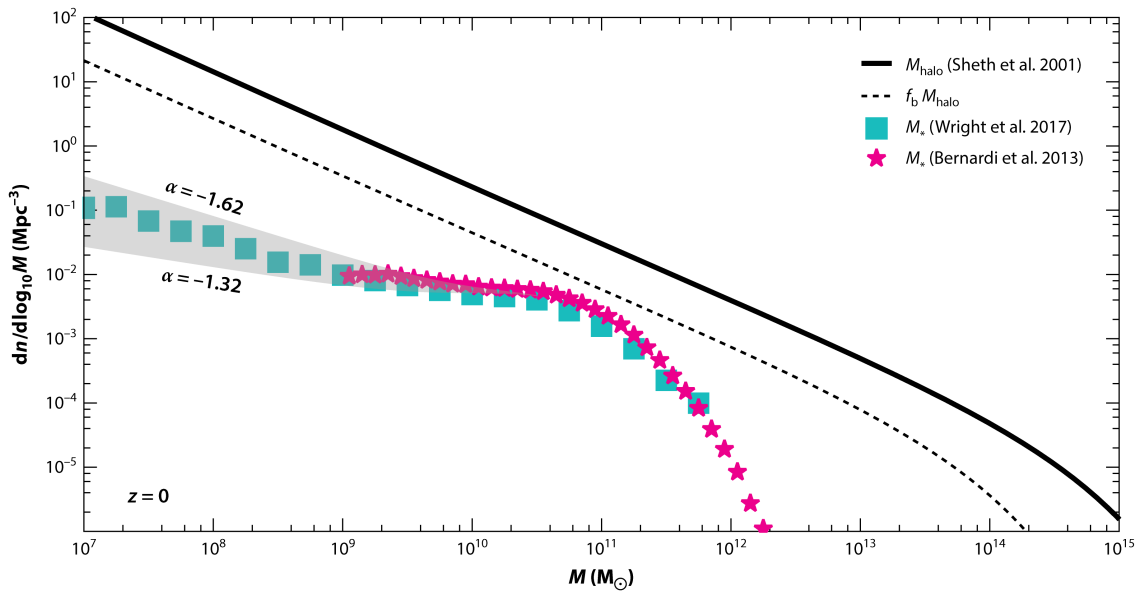
Introduction

The standard model of Big Bang cosmology Λ CDM model describes a universe consisting of three components: a cosmological constant denoted by Λ which describes dark energy, cold dark matter (CDM), and baryonic matter. Within this framework, primordial fluctuations seed large scale structure formation against an expanding background. As overdense regions collapse, they convert potential energy into kinetic energy and form virialized, dispersion-supported dark matter halos. Small halos collapse first, and merge together to form larger halos, building structure hierarchically. Pure dark matter (n-body) simulations provide a well-defined set of predictions about the numbers, clustering, and structure of dark matter halos [184]. The Λ CDM model is the simplest model that fits experimental observations of abundances of primordial elements (e.g. [35]), the structure and existence of the cosmic microwave background (e.g. [234, 171]), and large scale structure formation (e.g. [34]).

Baryons, which were well-mixed with dark matter in the early universe, collapse along with the dark matter halos. During this collapse, baryons cool via radiative processes and sink to the center of their dark matter halos, forming rotationally-supported gas disks. Stars then form from cool gas within these disks, resulting in galaxies with stellar, gas, and dark matter components. Generations of stars enrich their surroundings with heavy elements produced throughout their lives and at the moment of their deaths. These compounds produced within stars provide the conditions for life to arise, so understanding the origin of stars, and the galaxies in which they form, is fundamental to understanding our own existence.

1.1 Small Scale Problems

The Λ CDM model successfully describes conditions necessary to produce the large scale structure we observe today, but discrepancies between theory and observation arise on small scales. Assuming each dark matter halo has a constant fraction of baryons, f_b , and that those baryons are converted into stars with the same efficiency, ϵ_* , across all mass scales, one would expect stellar mass to scale linearly with halo mass. However, as shown in Figure 1.1, the predicted halo mass function deviates significantly from the observed stellar mass function. Maximum star formation efficiency is achieved at roughly the stellar mass of the Milky Way ($M_* \approx 10^{11} M_\odot$), while efficiency drops dramatically in the high- and low- mass ranges. This observed inefficiency, or suppression of star formation, particularly at the low-mass end of the mass function, is a topic of great interest in the field of galaxy evolution, and is known as the ‘missing satellites problem’ [354, 22, 290].



 Bullock JS, Boylan-Kolchin M. 2017. *Annu. Rev. Astron. Astrophys.* 55:343–87

Figure 1.1: Figure 5 from the [47] Annual Review shows the discrepancy between predicted and observed stellar mass functions. The halo mass function predicted by dark-matter-only simulations is denoted by the thick black line, and the corresponding stellar mass function assuming a constant baryonic fraction and star formation efficiency for each halo ($M_{\star} = \epsilon_{\star} f_b M_{\text{halo}}$) is plotted as a dotted black line. In comparison, the observed stellar mass function of galaxies of [29] and [358] are shown as magenta stars and cyan squares, respectively. The gray shaded region depicts a range of possible faint-end slopes between $\alpha = -1.62$ to -1.32 . Note that the maximum star formation efficiency is reached in galaxies of roughly $10^{11} M_{\odot}$, while star formation becomes increasingly inefficient at the low- and high- mass end of the mass function.

The clustering of CDM can be approximated at all masses by a simple formula known as the NFW profile, after Navarro, Frenk & White [219]. The NFW profile is characterized by a density profile that rises steeply at small radius, otherwise known as a cusp. However, observed dwarf galaxy rotational velocity profiles show a wide diversity of inner slopes, some of which rise linearly with radius [227]. These slowly rising rotation curves imply constant, underdense dark matter profiles in the galaxy centers, otherwise known as cores. This disparity between simulated and (some) observed dwarf galaxies is known as the ‘cusp vs. core’ problem, which has remained unsolved for decades.

Finally, the ‘too big to fail’ problem arises due to a shortage of galaxies with central densities indicative of halos of roughly $10^{10} M_{\odot}$. Such massive halos are believed to be too massive not to have formed stars, and the corresponding stellar mass of $10^6 M_{\odot}$ is likely too small for baryonic processes to disrupt the dark matter halo. This stellar mass range where this problem arises is beyond the scope of this study, but a detailed review of the challenges to the Λ CDM paradigm can be found in this detailed review [47].

These departures from the Λ CDM model have prompted some to look into warm (e.g. [193]) or self-interacting dark matter (e.g. [253]). A promising alternative to rethinking the nature of dark matter is to investigate the effects of baryonic feedback on star formation.

1.2 An Overview of Baryonic Feedback

A large amount of theoretical work has been done to understand the complex processes at work within galaxies, and has led to a wide variety of feedback models to consider. Careful observational measurements place valuable constraints on theoretical models and are necessary to fully understand the role of feedback in shaping dwarf galaxies.

1.2.1 Stellar feedback

High resolution simulations explore the effects of baryonic processes on dark matter halos and conclude that stellar processes are capable reconciling observed properties of dwarf galaxies with Λ CDM [350]. Bulk gas motions driven by bursty stellar feedback can cause fluctuations in the galaxy's gravitational, resulting in transformation from central dark matter cusps into cores [202, 127]. In these simulations, the removal of material from the galactic centers relies on strong outflow events, triggered by bursty star formation histories. Theoretical work also attributes star formation suppression in dwarf galaxies to heating and outflows driven by supernovae and stellar winds (e.g. [103, 150]). This scenario is supported by a large amount of observational evidence. Powerful outflows driven by star formation are observed in starbursting galaxies [198, 302], and it is often suggested that stellar feedback dominates in the dwarf regime [200].

1.2.2 AGN feedback

However, stellar feedback is not the only mechanism capable of influencing galaxy evolution. A large body of evidence supports the widely held notion that supermassive black

holes (SMBH) live at the centers of all massive galaxies, suggesting that they are directly connected to galaxy assembly (e.g. [296, 37]). Tight scaling relations between SMBH mass and large scale galaxy properties such as bulge mass and stellar velocity dispersion imply that the growth and evolution of SMBH and their host galaxies are linked. Energetic winds are often invoked to explain the connection between BH mass and galaxy properties far beyond the BH's gravitational influence. These winds are said to originate when the SMBH accretes material, which sheds its gravitational potential energy by radiative processes. At this point, the SMBH is referred to as an active galactic nucleus (AGN). Winds driven by AGN are thought to either heat or disperse cold gas, shutting down star formation in a process known as negative feedback. Alternatively, positive feedback might occur when these winds compress cold gas clouds and activate star formation.

These processes are extensively studied in high mass systems, but are not very well understood on the small scale. Dwarf galaxies ($M_{\star} \leq 10^{10} M_{\odot}$) have shallow gravitational wells which offer an ideal laboratory for studying various feedback processes. A deeper understanding of AGN activity in these environments will place valuable constraints on theoretical models of galactic feedback and extend our understanding of AGN processes into the low mass regime. Furthermore, dwarf galaxies are the building blocks of massive galaxies, meaning that understanding the processes that govern star formation in dwarfs is fundamental to understanding galaxy evolution as a whole.

Due to their small masses, BHs in dwarf galaxies are observationally difficult to study. As a result, AGN activity on dwarf galaxy scales has been largely unexplored until recently. Optical and IR signatures of hundreds of AGN candidates have been reported in

the last few years [249, 209, 273, 9, 31]. In fact, the infrared (IR)-selected AGN fraction is predicted to be 10 – 30% in galaxies in the stellar mass range $M_\star \sim 10^{8-10} M_\odot$, an order of magnitude higher than the established fraction in higher mass galaxies (1 – 3% for $M_\star > 10^{11} M_\odot$)[164]. Since there are several factors that hinder the detection of AGN in dwarf galaxies, this fraction can be regarded as a lower limit [275, 58]. Furthermore, observational evidence of AGN-driven outflows is rapidly accumulating [238, 41, 93, 195]. In the face of these new observations, it is becoming increasingly difficult to ignore the potentially important effects of AGN feedback in dwarf galaxy evolution.

1.3 This Work

This thesis project utilizes high resolution, spatially resolved spectroscopic observations of 50 dwarf galaxies with and without optical and IR signatures of AGN to investigate the potential for AGN to influence their low-mass hosts. We find several lines of evidence supporting the ability of AGN to effect large scale changes on their host galaxies in the dwarf regime. In Chapter 2, we report the first direct detection of AGN-driven ionized gas outflows in dwarf galaxies. We carefully measure the gas kinematics and show that the gaseous outflows have sufficient velocity to escape their hosts’ dark matter halos. In Chapter 3, we decompose galaxy kinematics into stellar and ionized gas components and analyze the various processes that can produce disturbed gas kinematics. In Chapter 4, we trace the star formation histories for each galaxy and discuss how various feedback processes are reflected in the observed stellar properties. Throughout this project, we assume the cosmological model $H_0 = 71 \text{ km s}^{-1} \text{ Mpc}^{-1}$, $\Omega_m = 0.27$, and $\Omega_\Lambda = 0.73$.

Chapter 2

Outflows

We present spatially resolved kinematic measurements of AGN-driven outflows in dwarf galaxies in the stellar mass range $\sim 6 \times 10^8 - 9 \times 10^9 M_{\odot}$, selected from SDSS DR7,8 and followed up with Keck/LRIS spectroscopy. We find spatially extended (~ 1 half light radius), high velocity ionized gas outflows (W_{80} up to $\sim 2000 \text{ km s}^{-1}$) in 13/50 dwarf galaxies with and without AGN. Nine of the galaxies with outflows have optical line ratios indicative of AGN, and six of these have outflow components with optical line ratios also consistent with AGN ionization. Outflow velocities in all 13 galaxies exceed the escape velocities of their halos. Nine of these 13 galaxies are classified as AGN according to their narrow line flux ratios. Of these, six have outflow components with emission line ratios consistent with AGN ionization. Although black holes have been known to populate the centers of at least a few dwarf galaxies, and indirect evidence of AGN quenching of star formation in dwarfs has begun to surface, our measurements constitute the first direct detection and measurement of AGN impact on the large scale kinematics and gas content in dwarf galaxies. Furthermore,

we find evidence suggestive of ongoing star formation suppression, possibly regulated by the AGN. Galaxy formation models must therefore be able to account not only for the formation and growth of black holes at the centers of dwarf galaxies, but should also be revised to include AGN as important – and perhaps dominant – sources of feedback in low mass galaxies.

2.1 Introduction

Well established correlations between black hole (BH) masses and global galactic properties imply a scenario where the growth and evolution of a BH and its host galaxy are connected and regulated by feedback from the active galactic nucleus (AGN) (e.g., [174]). In massive galaxies, the presence of AGNs has been shown to be linked to the development of powerful gas outflows (e.g., [140, 204, 64, 258]), which are a vital ingredient of galaxy formation models within the cosmological framework of Λ Cold Dark Matter (Λ CDM), as they regulate and suppress star formation [329, 279, 98, 241] and bring the luminosity function of galaxies into agreement with the predicted dark halo mass function [75, 212].

In the mass regime of dwarf galaxies ($M_* < 10^{10} M_\odot$), a large body of theoretical work attributes the regulation of star formation solely to reionization and stellar feedback, by means of radiation from young stars and supernova explosions [23, 37]. In fact, powerful outflows driven by star formation have been observed in starbursting dwarfs such as M82 [198, 302]. Further observational evidence suggests that supernova feedback is likely to dominate in dwarfs [200]. Quenched dwarf galaxies are rare, and the vast majority of them are found within 4 virial radii of a larger galaxy ($M_K < -23$) [122], so environmental

effects are likely largely responsible for gas removal from low mass galaxies. However, a small number of isolated dwarf galaxies are observed with no signs of recent star formation [154], showing that processes internal to dwarf galaxies cannot be ruled out as quenching mechanisms. Interestingly, evidence of AGN via optical and infrared (IR) indicators has been detected in hundreds of nearby dwarf galaxies [247, 209, 273]. [164] report the IR-selected AGN occupation fraction in high mass galaxies to be 1–3%, while the same criteria yield a 10–30% fraction in dwarf galaxies ($M_* \sim 10^{8-10} M_\odot$). Given that there are several factors that hinder the detection of AGN in dwarfs [275, 58], this large AGN fraction can be regarded as a lower limit. These studies suggest that AGN are common and potentially important phenomena in the low mass regime.

The role of AGN feedback in dwarf galaxy evolution is being explored theoretically, with diverse results. In idealized environments and using simplifying assumptions, such as spherical symmetry and single-phase ISM, [85] find that AGN can be more efficient than star formation at clearing dwarf galaxies of their gas. [175] explore a range of photoionization models and outflow geometries in isolated dwarfs, concluding that AGN are unlikely to regulate star formation but can boost the energetics of existing stellar-powered outflows. Cosmological simulations considering AGN feedback in high- z dwarf galaxies indicate that BHs can provide a significant amount of feedback, able to effectively quench star formation [13] and potentially reconcile observed dwarf galaxy anomalies with Λ CDM predictions [284]. Conversely, [313] find that even in the most extreme BH growth scenario, AGN feedback is negligible in comparison to ionizing starlight. In fact, they find that supernovae feedback stunts BH growth and quenches AGN feedback. This wide variation in theoretical

results demonstrates the need for observational constraints on the coupling of AGN energy to the interstellar medium (ISM) of dwarf galaxies.

Encouragingly, observational evidence of AGN feedback in dwarf galaxies is beginning to surface. In a study of 69 quenched dwarf galaxies from the MANGA survey [49], [238] find hints of a correlation between low star formation activity and the presence of AGN. Six quenched galaxies in their sample show signs of AGN, and five of their six AGN candidates show ionized gas kinematically decoupled from their stellar velocity fields, suggestive of either outflows or recently accreted gas. Additionally, [41] have found gas-depleted isolated dwarf galaxies with optical line ratios consistent with AGN, and [93] report AGN-like line ratios in a majority of the quiescent galaxies in their sample.

These promising results challenge current conceptions of feedback in dwarf galaxies and raise the question of whether the gas escapes the dark matter halo, permanently exhausting star formation in the galaxy, or stalls in the halo to cool and fall back later as part of a cycle of active and quiescent phases in a dwarf galaxy's life. This will ultimately depend on the mass removed by the outflow and its relative velocity compared to the velocity needed to escape the combined gravitational pull of the dwarf galaxy and its dark matter halo.

Additionally, dwarfs are expected to have a lower merger rate and a more quiet merger history than more massive galaxies [255], making their BHs closer relics of the initial BH seeds from which they originated (e.g., [324]). If AGN feedback influences the growth of BHs in dwarf galaxies, these objects will not be useful tracers of the seed BH population, and will have significant implications for BH seed formation models [206].

A complete understanding of AGN feedback will rely on thorough investigations of outflows affecting all phases of the interstellar medium (e.g. [67]). In the meantime, direct detection and measurement of any AGN-driven outflows in dwarf galaxies will be a crucial first step. In this work, we examine a sample of mostly isolated dwarf galaxies, both with and without optical and IR signs of AGN activity. We directly detect, measure and characterize ionized gas outflows in 13 dwarf galaxies and report the first velocity measurements of AGN-driven outflows in this mass regime.

We present our sample selection and observations in Section 2.2. We describe our fitting methods and kinematic analysis in Section 3.3, with the criteria for outflow detection presented in Section 2.3.3. We present the results of our fits in Section 2.4, provide our physical interpretation of our results in Section 2.5, and summarize in Section 2.6. Throughout the paper we assume the cosmological model $H_0 = 71 \text{ km s}^{-1} \text{ Mpc}^{-1}$, $\Omega_m = 0.27$, and $\Omega_\Lambda = 0.73$.

2.2 Data

2.2.1 Sample Selection

Drawing from the Sloan Digital Sky Survey Data Releases 7 and 8 (SDSS DR7,8), [247], [209], and [273] (hereafter RGG13, M14, and S15, respectively) have identified hundreds of nearby ($z < 0.1$) dwarf ($M_* < 10^{10} M_\odot$) galaxies that exhibit optical and IR signatures of AGN. RGG13, M14, and S15 selected their samples using standard optical emission line diagnostics which probe the hardness of the dominant ionizing source. RGG13 identified 151 AGN candidates using the Baldwin, Phillips & Terlevich (BPT) diagnostic

[11] and the presence of broad $H\alpha$ emission lines. M14 also drew from SDSS and used the BPT, He II, [S II], and [O I] AGN indicators to build their sample. They imposed further distance and photometry cuts in order to probe the low luminosity regime, resulting in a sample of 28 AGN. S15 extended the number of AGN candidates significantly (336) by including sources which have He II emission and redder mid-IR colors consistent with AGN [155, 299]. Due to their similar selection criteria, there is significant overlap between these three parent samples.

From the parent samples of RGG13, M14, and S15, we selected candidate AGN host galaxies for follow-up study based on (1) emission line ratios falling above the star forming sequence [163] on the BPT diagram and (2) presence of the high ionization He II emission line [282]. Priority was given to spatially extended galaxies, and face-on galaxies were excluded whenever possible, to facilitate spatially resolved kinematic and emission line diagnostic measurements. Other than this, galaxies were selected from the subsample based on the right-ascensions that could be observed during our observing time. The resulting observed sample contained 29 galaxies with optical signatures of AGN activity (Fig. 2.1). Fifteen of the AGN in our sample were selected from RGG13, an additional nine only from M14, and five more only from S15.

A control sample of galaxies with no optical or IR signatures of AGN was selected from the OSSY catalog [223], which provides spectral line analysis for the entire SDSS DR7 atlas. We matched the sample with the MPA-JHU catalog [44, 163, 314], in order to obtain stellar masses. We applied the same redshift and stellar mass cuts as the AGN sample and excluded all galaxies falling above the star forming sequence on the BPT diagram, as well as

all galaxies with detectable He II [282]. We also excluded potential AGN based on the WISE mid-IR color criteria [155, 299]. From this parent sample, we selected spatially extended galaxies to match the characteristics of the AGN sample. NGC 1569 was included specifically to facilitate comparison with previous kinematic studies [197]. The resulting sample of 21 star-forming dwarf galaxies were those with coordinates that could be observed during the Keck observing runs. BPT line ratios from the central 0.2 kpc and corresponding redshift and mass distributions of our targets are shown in Fig. 2.1. The full sample is described in detail in Chapter 3.

Note that the control sample could potentially contain AGN that elude the selection criteria we used. Several factors can hinder the detection of AGN in dwarf galaxies, including dilution by the host galaxy (e.g. [210]), low metallicity [166], and AGN variability [189]. In each case, the qualitative effect is to obscure existing AGN signifiers.

2.2.2 Observations and Data Reduction

We obtained longslit spectroscopy of the 50 targets using the Low Resolution Imaging Spectrometer (LRIS; [226, 50]) on the Keck I telescope on the nights of UT 2015 March 24–25, December 4–5, and 2017 June 24–25. We placed a 1 arcsecond-wide slit along the semimajor axis (see Fig. 3.2) of each galaxy, projecting to ~ 7 pixels on both the blue and red CCDs (Marconi on LRIS-B and LBNL on LRIS-R). The objects in our sample are located at distances between 3 and 209 Mpc ($z < 0.05$), which yield spatial scales between 14 and 965 pc arcsec⁻¹ [359]. For the blue side (LRIS-B), we used the 600 groove mm⁻¹ grism blazed at 4000Å, yielding a dispersion of 0.63Å pixel⁻¹. For the red side we used

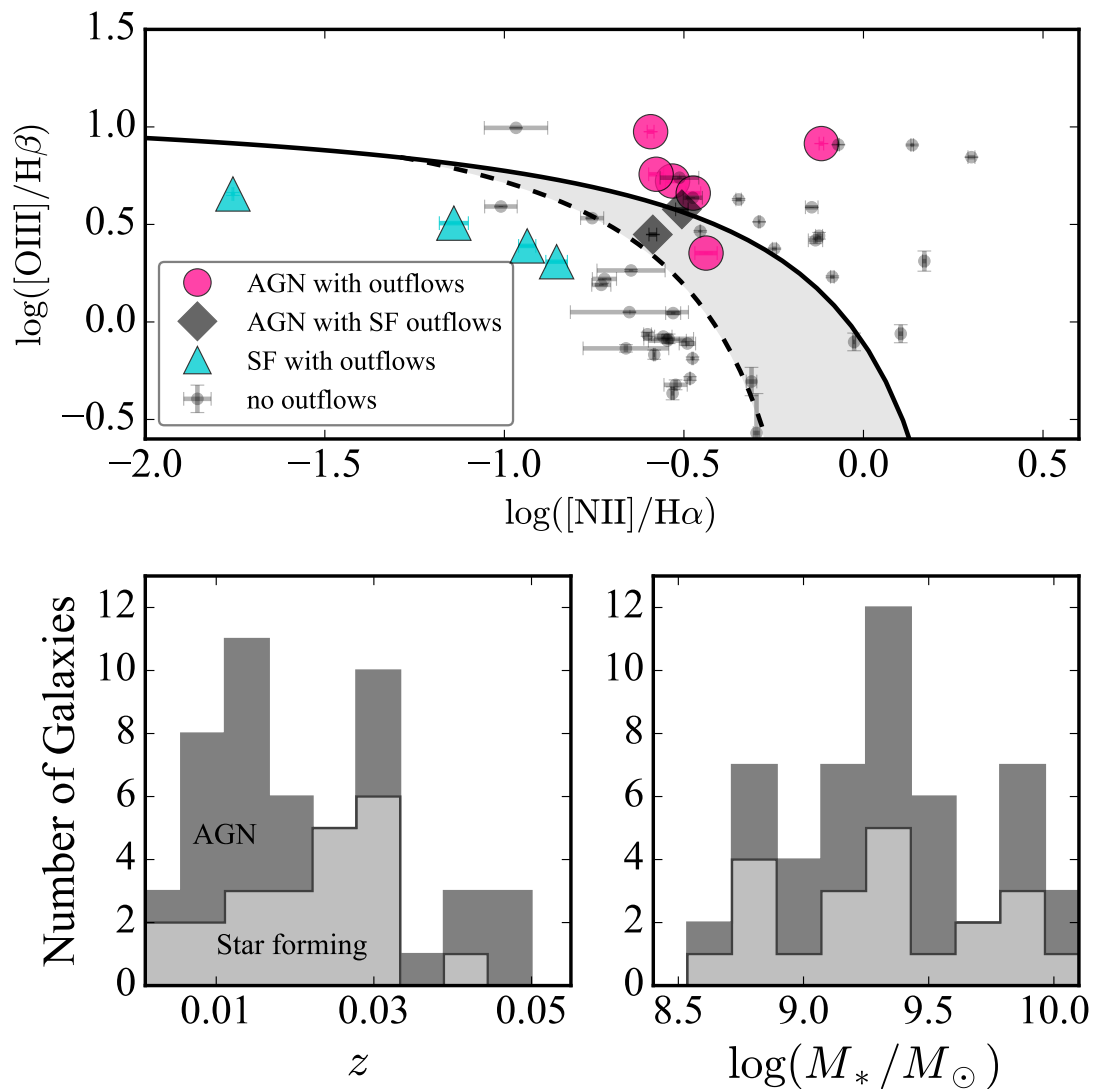


Figure 2.1: Top: BPT line ratios from the central 0.2 kpc of each galaxy for dwarf galaxies in our sample observed with Keck/LRIS. 29 galaxies with optical signatures of AGN were selected from the samples of RGG13, M14, and S15. The remaining 21 are a control sample composed of star-forming dwarf galaxies. Dwarfs that present signatures of gas outflows are plotted with larger symbols. Bottom: Redshift and stellar mass distribution of our sample of dwarf galaxies.

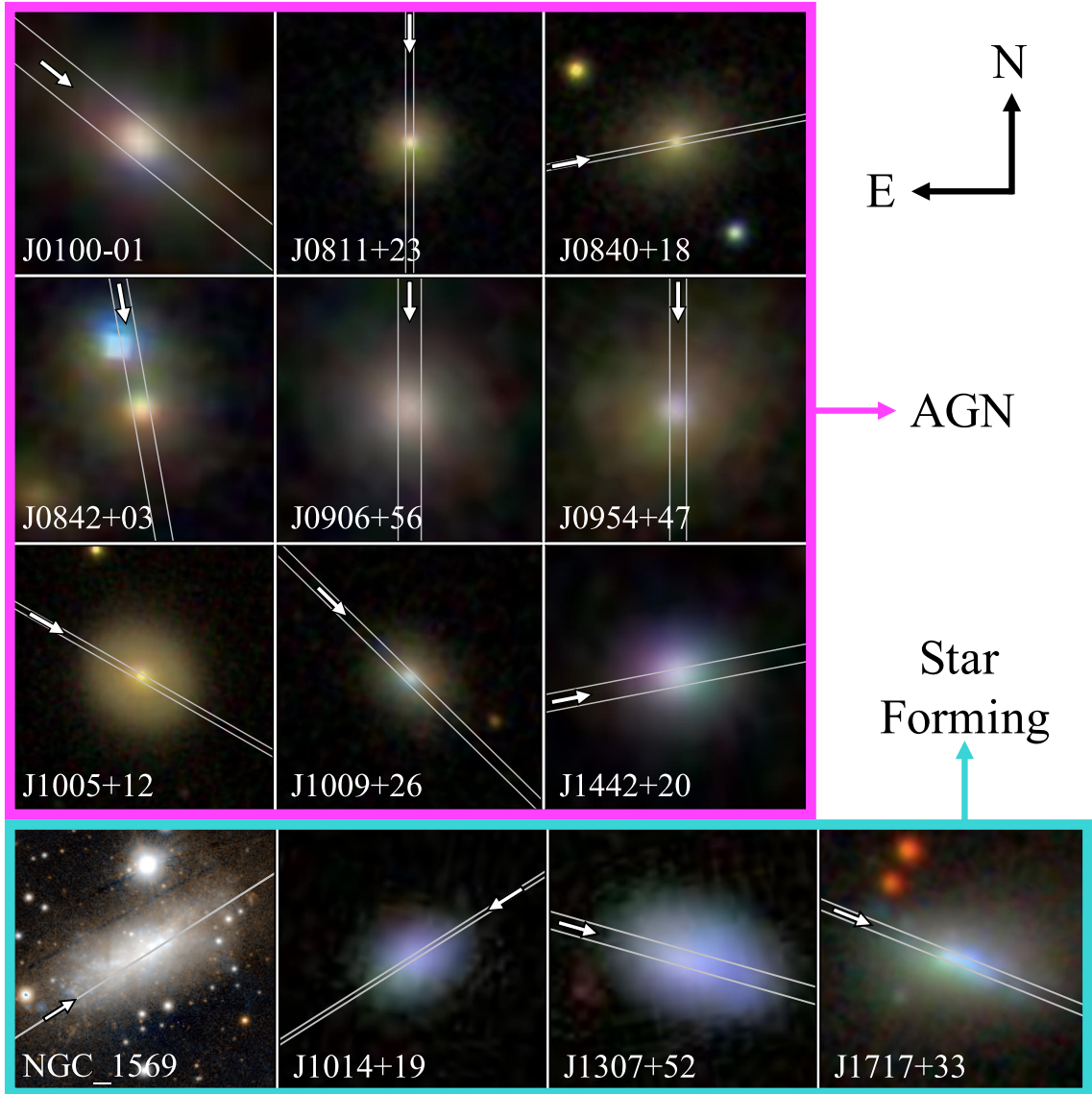


Figure 2.2: SDSS color images of the 13 dwarf galaxies with spatially extended outflows. All images were generated using the SDSS DR12 finding chart tool, with the exception of NGC 1569, which is outside of the SDSS footprint. The NGC 1569 thumbnail is a PanSTARS z,g band color image rendered in the Aladin Lite Viewer with a 3' field of view (~ 1 kpc on a side). Each SDSS image is scaled to 10 kpc on a side and the placement of the 1 arcsecond-wide slit is shown in light gray.

either the 600 groove mm^{-1} grating blazed at 5000\AA , the 900 groove mm^{-1} grating blazed at 5500\AA , with a 5600\AA dichroic, or the 1200 groove mm^{-1} grating blazed at 7500\AA , with a 5000\AA dichroic, yielding dispersions of 0.80, 0.53, and $0.40\text{\AA pixel}^{-1}$, respectively. We obtained one or two 1200 second exposures of each galaxy. To achieve the signal to noise ratio necessary for proper fitting of the spectra, a second exposure was necessary for galaxies with surface brightness $> 21.5 \text{ mag arcsec}^{-2}$. The weather was clear on all six nights, and the seeing was typically under 0.6 arcsec, except on UT 2015 March 24, when it was 0.7 arcsec. For details of observations of individual objects see Chapter 3. The data were reduced using a Python pipeline to automate the standard IRAF reduction tasks. Flexure on the red camera was corrected using the average shift in sky lines. There are not enough sky lines to correct for flexure on the blue CCD, so each galaxy spectrum on the blue side was redshift-corrected using the redshift measured from the flexure-corrected red spectrum. Flexure on the blue CCD was then calculated by comparing galaxy emission lines with their expected rest frame values. The longslit spectra were rectified along both the wavelength and spatial axes, creating 2-dimensional spectra where each pixel row is a fully reduced 1-dimensional spectrum. Customized extractions along the slit are obtained by summing pixel rows, allowing us to preserve spatial information by extracting small sections of the spectra or to sum over large apertures when higher signal to noise is required.

2.3 Analysis

Visual inspection of the emission line profiles of the galaxies in our sample revealed clear broadened, often blueshifted wings in some of the galaxies. Such line profiles are often

indicative of gas outflows. Thus, in order to systematically search for outflows in our sample, we conducted a detailed and consistent fitting process as described below.

2.3.1 Fitting the Stellar Continuum

For each of the 50 galaxies in our extended sample, we used the same fitting algorithm to systematically identify and measure outflows. For each source, we began by extracting a one-dimensional spectrum of the entire galaxy, when possible. Some galaxies in our sample have contaminating foreground stars, in which case we chose custom apertures to maximize the extraction region while excluding the contaminating sources.

In order to measure accurate emission line fluxes, it is necessary to account for stellar absorption, which primarily affects the Balmer emission lines. Penalized Pixel-Fitting method (pPXF) [59] is an algorithm designed to extract stellar kinematics using a maximum penalized likelihood approach to match stellar spectral templates to absorption features in galaxy spectra. In order to minimize template mismatch, stellar templates with relevant stellar types, negligible emission line contamination, and full wavelength coverage for the wavelength range in our galaxy spectra were chosen from the Indo-US Library of Coudé Feed Stellar Spectra [318]. pPXF is designed to choose the appropriate stellar templates automatically, but it is necessary to check that emission line contamination from the ISM in the templates does not skew the fit, ultimately resulting in underestimation of Balmer emission line fluxes. Visual inspection of the fit to features such as the Ca II $\lambda 3933$ line, which is free from contaminating emission lines, allows us to assess whether the stellar continuum and absorption features are being properly estimated. An example of a fit to the stellar spectrum of a galaxy is shown on the top panel of Fig. 2.3. Careful selection of

stellar templates is especially important for young stellar populations, whose fits are often much improved by considering only B and A-type stellar templates in order to carefully fit their prominent Balmer absorption features.

2.3.2 Fitting Emission Lines

After subtracting the best-fitting stellar population model of the galaxy, the residual emission lines were fit using a custom Bayesian MCMC maximum likelihood sampling algorithm, implemented using the Python package *emcee* [113]. Due to their strength and general isolation from other strong spectral features, we used the [O III] $\lambda\lambda 4959, 5007$ doublet to constrain line profiles for the rest of the emission lines in the spectra. The middle panels of Fig. 2.3 show that a single Gaussian produces a poor fit when broadened wings are visible in the [O III] doublet. To address this, we constructed a double-Gaussian model consisting of a narrow and a broad component. In order to reduce the number of free parameters in the [O III] line profile fit, we placed three constraints on each Gaussian component: (1) Based on transition probabilities, the flux ratio between [O III] $\lambda 4959$ and [O III] $\lambda 5007$ was fixed to 1:3; (2) the velocity widths derived from each Gaussian component were forced to be equal in both emission lines in the doublet; (3) the spacing between the emission lines was held fixed at $2869.35 \text{ km s}^{-1}$ or 47.92 \AA . Fe I $\lambda\lambda 4985, 4986, 5016$ lines contribute a small amount of additional flux which causes the fit to overestimate the width of the broad component. To address this contamination, we model them with independent amplitudes and widths equal to that of the narrow component of [O III]. The following were left as free parameters: (1,2) Amplitudes of narrow and broad components; (3,4) velocity widths of narrow and broad

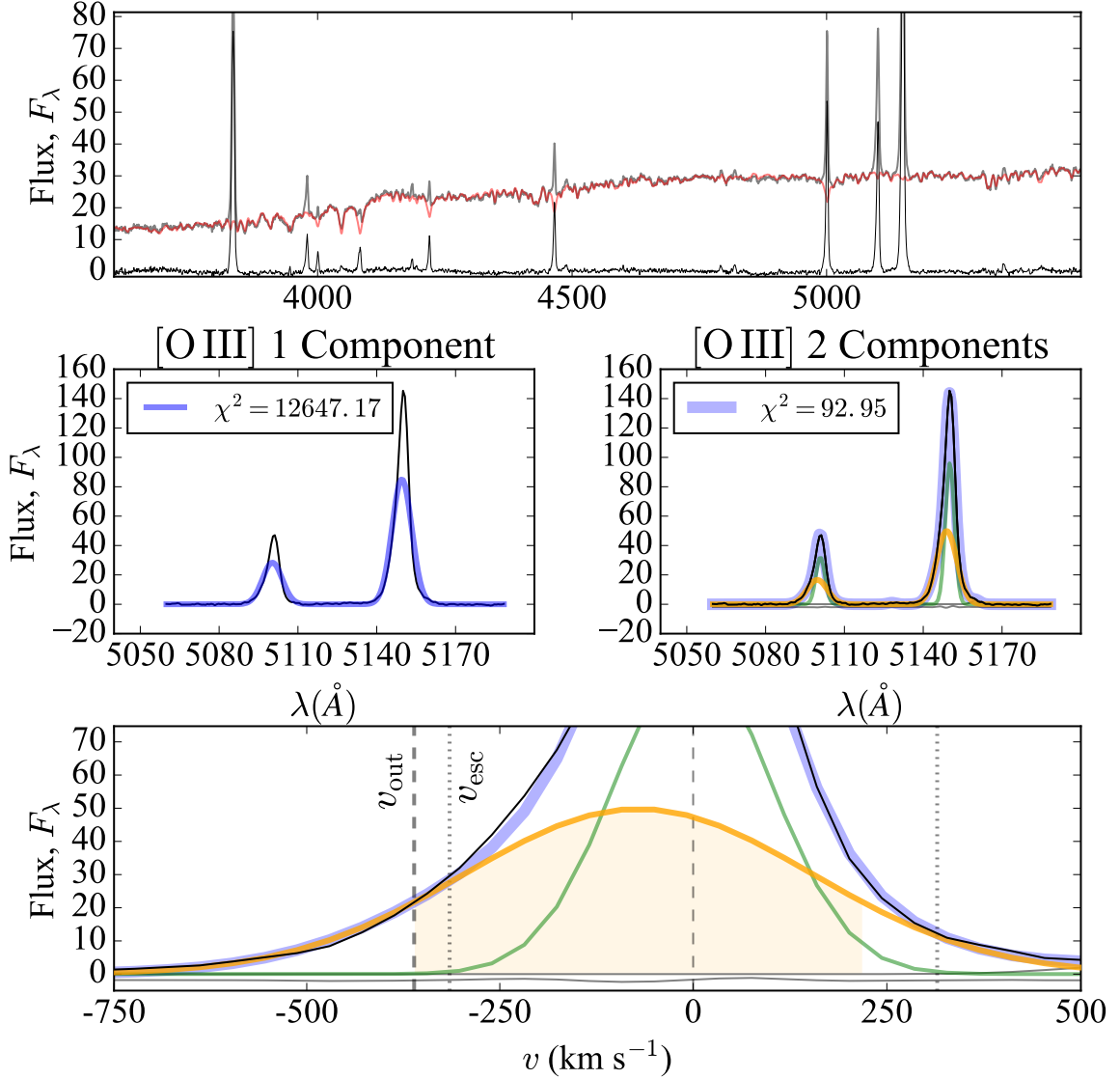


Figure 2.3: Top: The spectrum of J084234.51+031930.7 is extracted from within R_{50} (gray). The pPXF best fit stellar continuum (red) is subtracted, leaving the residual emission spectrum (black). The flux units in this figure are ($\text{erg cm}^{-2} \text{s}^{-1} \text{\AA}^{-1}$). Middle: One- and two-component Gaussian fits to the [O III] doublet are shown. The one-component model on the left is clearly a poor fit compared to the multicomponent fit on the right. The narrow (green) and broad (orange) component color scheme is used throughout this paper. Bottom: A close up of the outflow component of [O III] $\lambda 5007$ and its $W_{80} \sim \text{FWHM}$ shaded in orange, indicating the outflow velocity (dashed line) and escape velocity of this galaxy (dotted line).

components; (5) recession velocity of the doublet, set by the mean velocity of the narrow component of [O III] λ 5007; (6) velocity offset between narrow and broad components; and (7-9) amplitudes of contaminating Fe I lines.

2.3.3 Detecting Outflows

Broadened or shifted components in emission lines trace gas with different kinematics than the rest of the ionized gas in the galaxy. Such components potentially trace outflowing gas. In order to systematically detect outflows, we fit both single and double Gaussian models to the [O III] doublet in each of the 50 galaxies in our sample. Fits were performed on one-dimensional spectral extractions covering as much of each galaxy as possible, as described in Section 3.3.3. Details of the double Gaussian models are described in Section 2.3.2 and examples of the single- and double-component fits are shown in the two middle panels of Fig. 2.3.

An additional Gaussian component always reduced the χ^2 of the fits, so a rigid goodness-of-fit threshold to determine whether a line requires a second Gaussian would not yield robust results. Instead, we flagged each fit that produced a second kinematic component wider than the instrumental resolution ($\sigma > 80 \text{ km s}^{-1}$) and amplitude higher than the noise level of the spectrum. This approach yielded a subsample of 15 candidate outflow galaxies.

Next, we examined the spatial extent of these broad components by repeating the double Gaussian fits on smaller extraction regions along the slit in each of the 15 galaxies. We found that the broad [O III] components in two AGN-hosting galaxies, J094941.20+321315.9 and J141208.47+102953.8 are spatially unresolved. The remaining 13 galaxies,

however, show clear broadened components in their [O III] at all radii, as long as the emission line was detectable (typically out to one half light radius, or $\sim 1 - 3$ kpc). Based on their narrow component emission line ratios, nine of these 13 galaxies with spatially resolved broad components are classified as AGN and four are star forming (SF). Full names, redshifts, stellar masses, and narrow line BPT classifications for these 13 outflow galaxies are listed in Table 2.1.

Of our full sample of 50 galaxies, 31% (9/29) of the AGN and 19% (4/21) of the SF galaxies show spatially extended outflows. If we include the two AGN with spatially unresolved broad components, we observe outflows in 38% of the AGN in our sample.

2.3.4 Outflow Velocity

Table 2.1 lists fit outputs to one-dimensional spectrum extractions within the r-band Petrosian half light radius (hereafter R_{50}) of each of the 13 galaxies discussed in this work. W_{80} , the velocity width containing 80% of the flux of an emission line, is a widely used metric to describe outflow velocities [140]. For a single Gaussian profile, $W_{80} = 1.09$ FWHM. We define the outflow velocity

$$v_{\text{out}} = -v_0 + \frac{W_{80}}{2} \quad (2.1)$$

where v_0 is the velocity offset between the center of the narrow and broad components (see Fig. 2.3) and is negative when blueshifted.

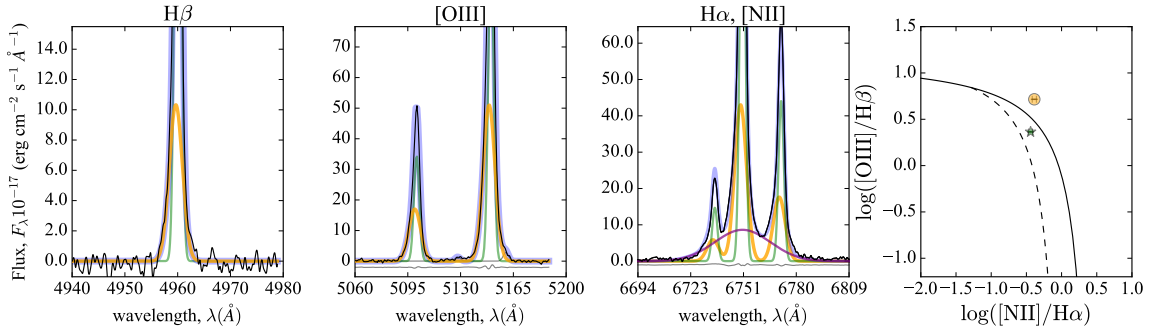


Figure 2.4: Emission lines for J084234.51+031930.7 are shown as an example of how the kinematic components can be decomposed and placed on the BPT diagram. As described in Section 2.3.2 and illustrated in Fig. 2.3, the stellar continuum is subtracted and the residual [O III] doublet is fit using a double Gaussian model which includes contaminating Fe I lines. The widths of H α , H β , and [N II] are fixed based on the [O III] model, but the fluxes for each kinematic component are left as free parameters. The resulting line flux ratios for the narrow (green star) and the broad component (orange circle) are plotted on the BPT diagram (right). In this case, the model required an additional broad H α component, which was used to obtain a black hole mass (See Appendix A.1).

2.3.5 Decomposed Flux Ratios

In most of the galaxies discussed here, the broad emission line component can be detected in several emission lines. When possible, we applied the two-component kinematic [O III] model to H α , H β , and [N II] in order to place the outflowing gas on the BPT diagram. The kinematic model (velocity offsets and widths) measured in [O III] are held fixed while the amplitudes of each kinematic component are allowed to vary independently. Due to their small separations, H α and the [N II] doublet were fit simultaneously, with the flux ratio of [N II] λ 6548 and [N II] λ 6563 fixed at 1:3 in accordance with their transition probabilities. Two galaxies (J084234.51+031930.7 and J100935.66+265648.9) required an additional broad H α component in order to constrain the outflow H α /[N II] flux ratio. See Appendix A.1 for further discussion on additional broad H α components associated with the broad line region (BLR). The full multicomponent fits to H β , [O III], H α , and [N II]

as well as the resulting kinematically decomposed BPT ratios for J084234.51+031930.7 are shown in Fig. 2.4.

2.4 Results

2.4.1 Classifying Outflows

In Fig. 2.5, we show the position of the narrow and broad components (small and large symbols, respectively) on the BPT diagram, obtained following the procedure described in Section 2.3.4. The two components for each galaxy are connected by a thin line of the same color.

The star forming galaxies (cyan triangles) were included in our control sample due to their narrow components' positions on the BPT star forming sequence. Two of the SF objects (J101440.21+192448.9 and J130724.63+523715.2) are from the RGG13 sample of BPT star forming galaxies with broad $H\alpha$ lines. Follow-up observations of these two objects found that these broad $H\alpha$ features were transient and likely due to Type II supernovae (also confirmed by our observations [8]). The outflows in all four galaxies fall within the star forming region of the BPT diagram.

Emission line ratios falling above the [163] (dotted) line are widely regarded as evidence of AGN activity. However, a well known limitation of the BPT diagram in definitively identifying AGN is that shock ionization with significant contribution from precursor gas can produce line ratios in star forming galaxies that mimic those of AGN [4]. Strong near IR detections of the [Si VI] coronal line provide independent confirmation of the presence

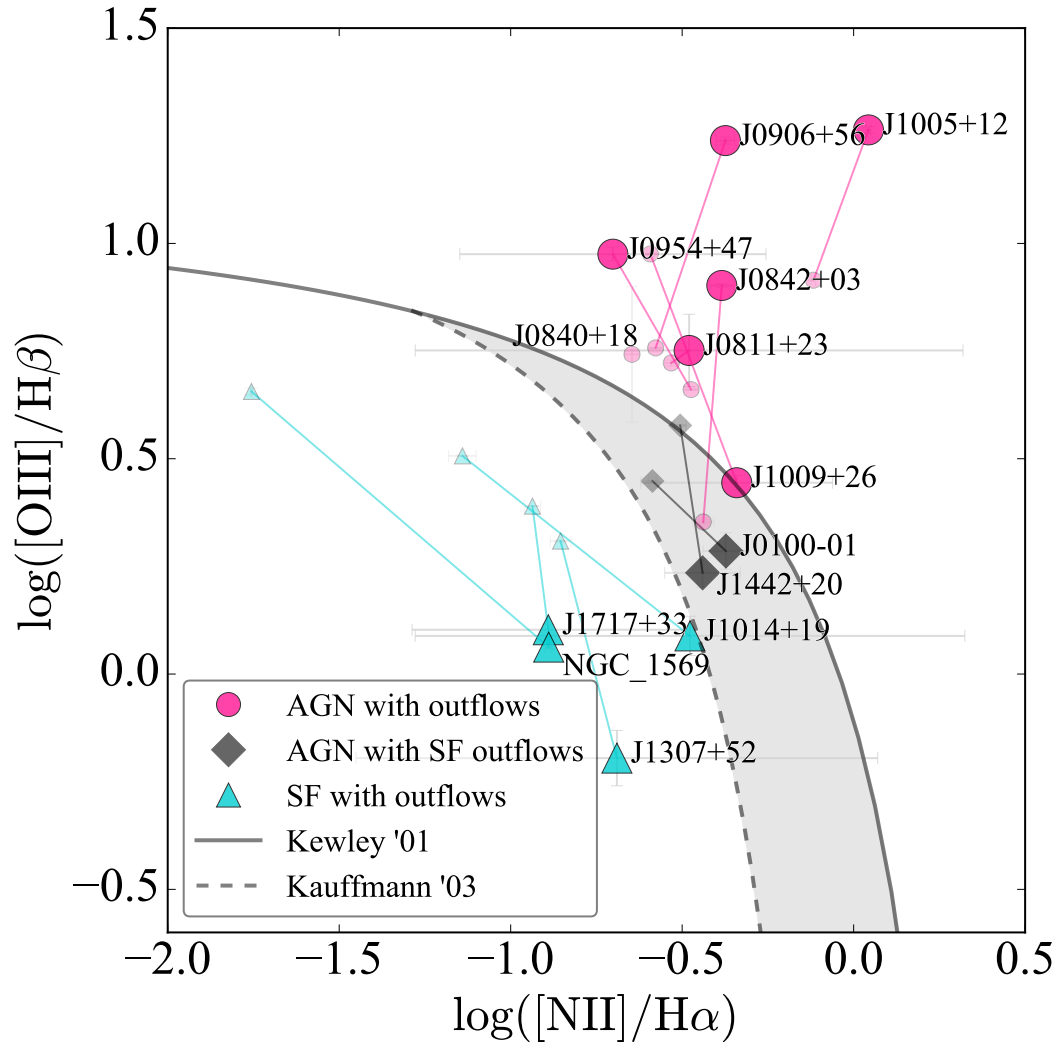


Figure 2.5: Narrow and broad emission line ratios are shown for each galaxy with outflows. The smaller symbols show the position of the bound gas (narrow component in spectrum) for each galaxy, and the larger symbols those of the outflow (broad component). In this paper, each galaxy is classified based on its position of the outflow component in the AGN (pink circles), composite (gray diamonds), or star forming regions (cyan triangles).

of AGN in four of the dwarfs with outflows (J090613.75+561015.5, J095418.16+471725.1, J100551.19+125740.6, and J100935.66+265648.9; Bohn et al., in prep). Near IR line ratio diagnostics confidently exclude shocks as the originating ionizing mechanism in these objects. The $[\text{Ne v}]\lambda 3426$ coronal line is also detected in these four AGN as well as J084025.54+181858.9. These measurements provide additional evidence for the presence of AGN at least in these five objects. In this work, we classify the nine objects with narrow emission lines above the dotted [163] line as AGN.

Six dwarfs with AGN have broad components that occupy the region above the [165] maximum starburst line (solid) on the BPT diagram, so we plot them as pink circles throughout this paper. J084025.54+181858.9 did not have a sufficiently high signal-to-noise ratio to fit the outflow in lines other than $[\text{O III}]$, so we count this object among the AGN-driven outflow sample based on its AGN-consistent narrow emission line ratios. Two of the AGN (gray diamonds) have outflow components that fall in the composite region, indicating a significant contribution from star formation.

Throughout this paper, we classify each outflow based on position of the broad component on the BPT diagram. Table 2.1 is sectioned according to the broad component BPT classification and lists the BPT classification for both narrow and broad components in the last two columns.

2.4.2 Integrated Properties of Outflows

In Fig. 2.6, we illustrate the difference in line profiles between galaxies with and without AGN. The galaxies are grouped according to the classification assigned in Sec-

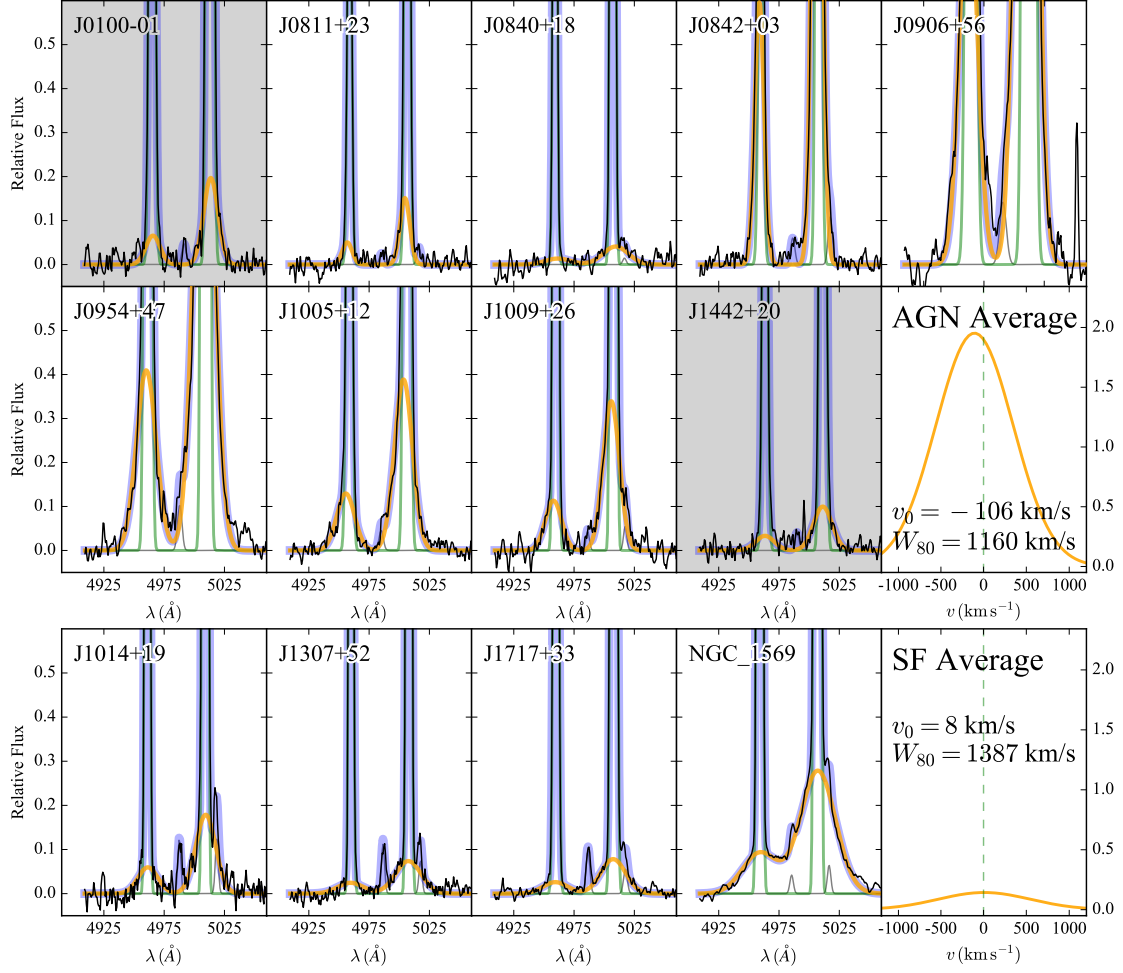


Figure 2.6: Details of the broad component fits to the [O III] doublets of each of the 13 galaxies with outflows are shown. The spectra are extracted from the region within the R_{50} of each galaxy and have all been normalized by the continuum flux just redward of [O III] λ 5007. AGN are grouped in the top figure and star forming galaxies are on the bottom. Average fit parameters, weighted by the luminosity of each narrow [O III] line, are shown in the last panel of each section. Panels shaded in gray are classified as composite and are excluded from the AGN outflow average. Values of v_0 , W_{80} , and v_{out} are listed for each of the 13 galaxies in Table 2.1.

tion 2.4.1, with nine objects hosting AGN on top and four SF galaxies on the bottom. Each panel shows multicomponent fits to the [O III] doublet of each galaxy. The spectra have been extracted from within R_{50} and normalized by the continuum flux just redward of [O III] λ 5007. As in Figs. 2.3 and 2.4, green curves trace the narrow component, orange curves indicate the outflow component, and contaminating Fe I lines are shown in gray. The orange curves in the two bottom right panels represent averages of the fits to AGN and star forming outflows, weighted by the luminosity of each narrow [O III] component. The composite outflow objects are shaded gray and are not included in the weighted average for AGN.

A comparison of the average AGN vs. star-forming emission line profiles reveals a fundamentally different line shape, with AGN outflows that are blueshifted with respect to the narrow component by $\sim 100 \text{ km s}^{-1}$, on average. This is in contrast with the outflows in star forming galaxies that show virtually no velocity offset. The broad component of the average AGN driven outflow line profile carries a larger percentage of the total [O III] flux than its star forming counterpart (22.8% and 4.9%, respectively).

There is no discernible difference between the stellar masses of the galaxies with and without outflows. However, the six galaxies with non-AGN driven outflows show signs of very active star formation relative to the rest of the sample. As we will further discuss in Section 2.5.4, the galaxies with AGN-driven outflows have redder colors than the four star forming galaxies and two AGN with stellar driven winds. These six galaxies with non-AGN-driven outflows have the highest specific star formation rates ($\log(\text{sSFR Gyr}^{-1}) > -0.5$) of

the entire sample of 50 dwarfs. The galaxies with AGN-driven outflows have sSFRs similar to the galaxies with no outflows ($-0.5 < \log(\text{sSFR Gyr}^{-1}) < -3$) [74].

2.4.3 Spatially Resolved Properties of Outflows

Common trends in the behavior of AGN-driven outflows as a function of radius are apparent. In general, the width of the broad component (W_{80}) broadens, the mean velocity offset of the broad component relative to the narrow (v_0) approaches zero, and the ratio of the broad to narrow component fluxes (F_b/F_n) increases with increasing radius. These trends are typical for the AGN in our sample. As an example, we show the spatial properties of the outflow in J090613.75+561015.5 in Fig. 2.7. This object was chosen due to its intermediate mass ($2 \times 10^9 M_\odot$) and color ($u - r_{\text{model}} \sim 1.7$), with respect to the rest of the galaxies hosting AGN driven outflows discussed here. The detailed spatial properties of the remaining galaxies are shown in Appendix A.2.

We confirm that the outflows extend all the way to the limit where our observations have a sufficiently high signal-to-noise ratio to fit [O III] (between 1.5 and 3 kpc from the center). In addition, their integrated line flux ratios are consistent with AGN out to these distances, indicating that the effect of the central AGN in these dwarfs is largely non-local.

Greene, et al. [130] use spatially resolved longslit spectroscopy of luminous obscured quasars to extend the relation between NLR size and [O III] luminosity and linewidth by an order of magnitude. To test whether the AGN would be able to ionize gas out to the distances in their host galaxies where we detect signal, we estimate the expected sizes of the narrow line regions (NLR) using this relation. We find that the NLR sizes range between

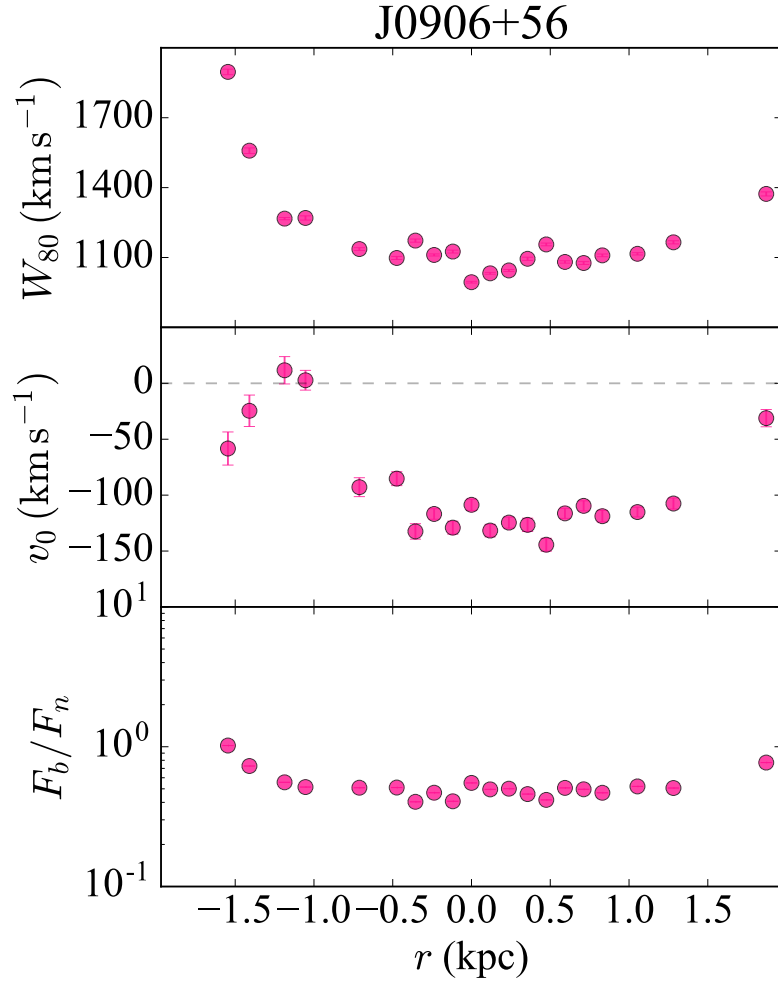


Figure 2.7: Spatial properties of the AGN-driven outflow in J090613.75+561015.5. The outflow width W_{80} and offset v_0 as defined in Section 2.3.4 as a function of radius are shown in the top two panels, respectively. The ratio of the broad to narrow [O III] flux is shown in the bottom panel.

3.1 and 3.5 kpc, well beyond the distances where we are able to measure line ratios (<3 kpc in all cases).

2.5 Discussion

2.5.1 Ionization by Star Formation vs. AGN

For simplicity, the outflows in this paper are classified as SF, composite, and AGN-driven based on the position of their broad components on the BPT diagram in Fig. 2.5.

We see that the broad outflow components for all four SF galaxies (cyan triangles) fall below and to the right of their corresponding narrow components, likely due to the contribution from shock-induced photoionization [4]. Stellar-driven outflows are commonly observed in massive starburst galaxies [257] and, at least in those galaxies, shocks often propagate through the ISM [291]. Thus, it is likely that the fast outflows in these four star forming galaxies are driven by stellar processes and at least partially ionized by shock heating. Though we cannot positively rule out the presence of faint or extremely variable AGN, we find no optical or IR evidence of AGN that could be driving the outflows in these control sample galaxies.

Six objects in our sample have broad components falling on or above the [165] line on the BPT diagram (solid black line in Fig. 2.5), indicating that they exceed the theoretical maximum ionization possible with star formation alone. We consider AGN to be the most likely mechanism for driving the outflows in these objects.

Two AGNs have outflow components that fall in the composite region, indicating a significant contribution from star formation to the ionization of these components. This

star formation contribution is more pronounced in the outflowing gas than the bulk of the bound gas (narrow component) in the galaxy. Thus, we regard these two objects as dwarfs that likely contain AGN, but whose outflows might be at least partially powered by star formation.

As mentioned above, we were not able to measure line flux ratios for the broad component of the remaining object, J084025.54+181858.9, due to their lower signal-to-noise ratio.

Note that J100935.66+265648.9 follows a similar trend to the two objects with composite broad components (gray diamonds) in that its broad component falls closer to the composite region of the BPT diagram relative to its narrow component. The inclusion of an additional broad $H\alpha$ component with $\text{FWHM} = 298 \text{ km s}^{-1}$ to the $H\alpha + [\text{N II}]$ model described in Section 2.3.2 was necessary to properly fit the outflow component fluxes for this object. This additional component is too narrow to convincingly be associated with the broad line region, and is possibly tracing an additional kinematic component of the outflow or a velocity gradient along the slit introduced by rotation. Though the broad emission line ratios appear to show significant dilution by star formation, the outflow remains on or above the [165] maximum starburst line. Thus, we count this object among those with AGN-driven outflows in our sample.

2.5.2 Outflow Line Profiles

Additional evidence of outflow origin could be inferred from the different structure of the spectral lines for AGN vs. star formation powered outflows. The average line profiles of AGN shown in Fig. 2.6 are more blueshifted and slightly less broad than those of SF

galaxies. This could be interpreted by considering the physical position of the source of the winds. In any given galaxy with radial outflows, the blueshifted gas will be easier to detect since the gas suffers from less galactic obscuration than the gas moving away from the observer (e.g., [291, 80]).

We speculate that the blueshifted outflow component can be explained by considering obscuration from denser material in the central regions of the galaxy. If there is only one source, and it is positioned in the center of the galaxy (as would be the case for AGN), most of the gas we observe will be blueshifted. However, if there are multiple sources scattered around the galaxy, with some of them being on the near side of the galaxy, closer to the observer (as would be the case with supernovae and regions of star formation), then we will be more likely to observe both the blue- and redshifted emission.

In Fig. 2.8, we illustrate the difference in AGN-driven outflow line profiles extracted from the center and the outskirts of a galaxy, using J090613.75+561015.5 as an example. The first panel shows the fit to $[\text{O III}]\lambda 5007$, extracted from the central ~ 0.4 kpc— note the blueshifted broad component. An extraction ~ 1.5 kpc from the center reveals a broad component with a smaller velocity offset and a slightly wider profile, consistent with the scenario where obscuration decreases with radius, revealing emission from both approaching and receding material. The typical radial trends of AGN-driven outflow properties introduced in Section 2.4.3 and Fig. 2.7 would be a natural consequence of the proposed model.

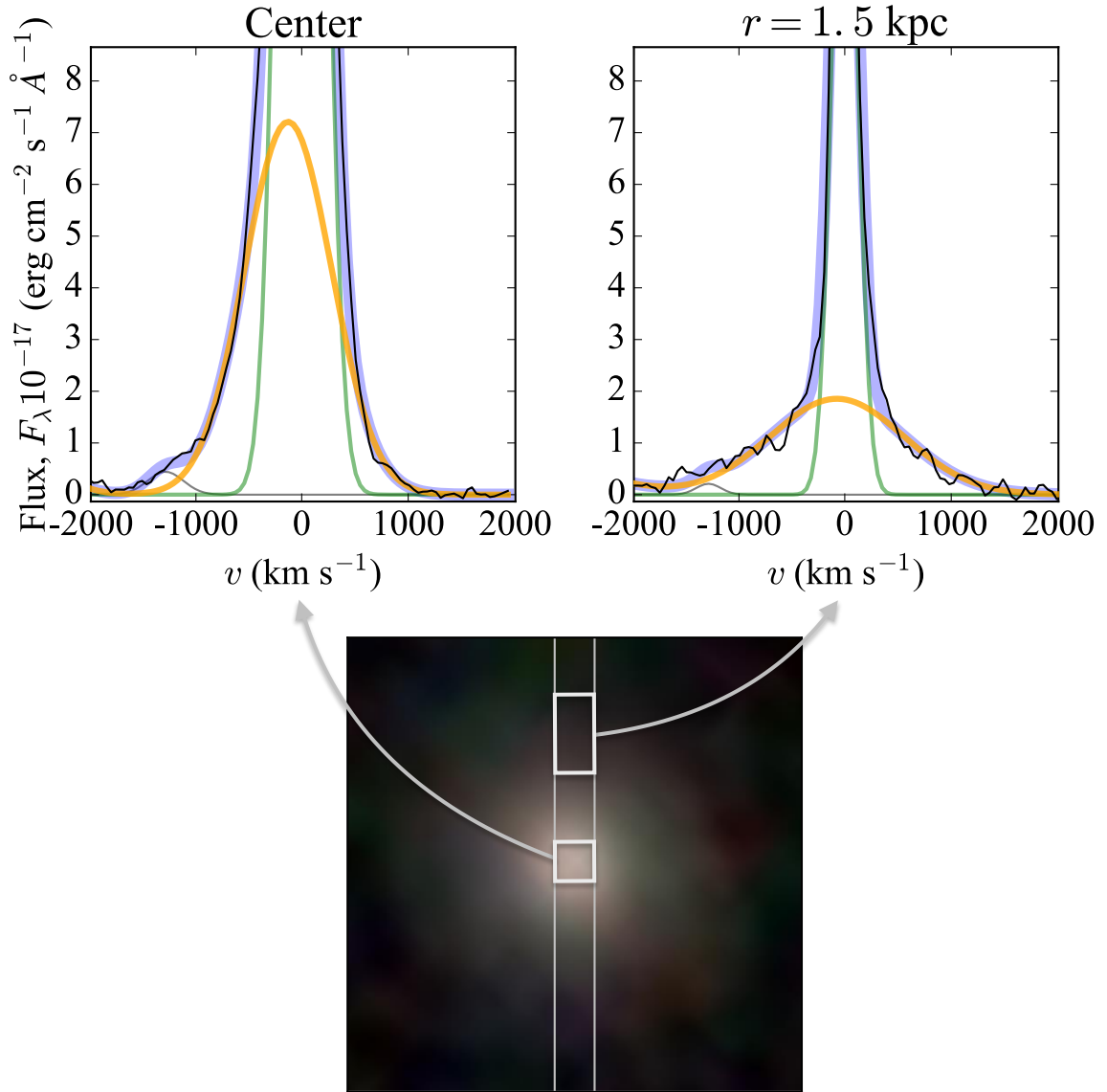


Figure 2.8: A comparison between outflow component line profiles extracted from the central ~ 0.4 kpc and ~ 1.5 kpc from the center of J090613.75+561015.5 is shown. We speculate that the central outflow appears blueshifted due to denser material in the center of the galaxy obscuring emission from the redshifted gas escaping the far side of the galaxy. Farther from the center, the outflow profile widens and the velocity offset becomes less pronounced as galactic obscuration fades and both blue- and redshifted portions of the outflow is revealed.

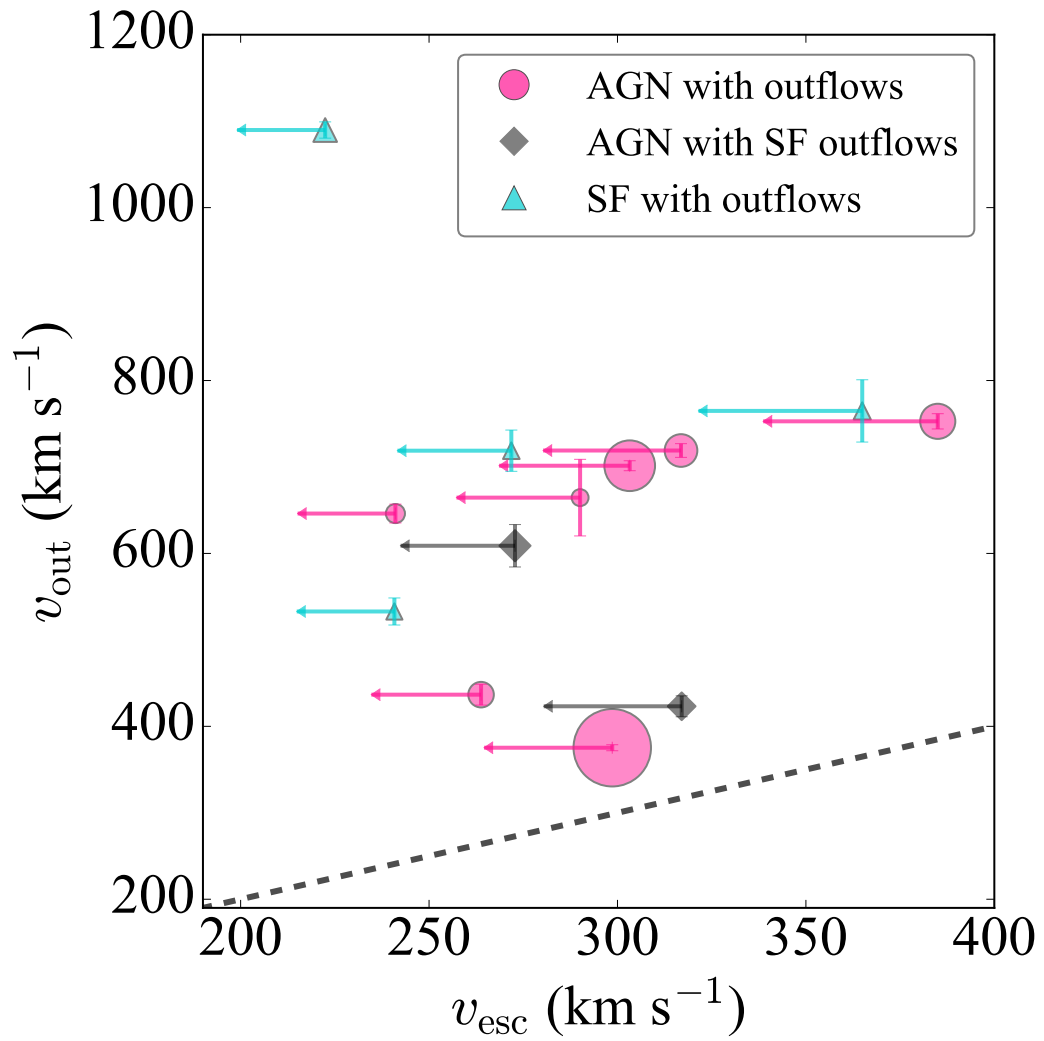


Figure 2.9: Relation between the velocity measured for the outflows and the modeled escape velocity assuming galaxies live in massive dark matter halos consistent with the cosmological picture of Λ CDM. In all cases, the wind speed is comparable or above that needed to escape the dark matter halo. To guide the eye, the dashed line indicates a 1-to-1 relation.

2.5.3 Gas Velocity

In order to test whether these winds are capable of escaping the gravitational potential of their host halos, we calculated the escape velocity of each galaxy. We assume an NFW dark matter density profile [219] and use abundance matching [212] to estimate the halo mass from stellar mass for each galaxy. The escape velocity is

$$v_{\text{esc}}(r)^2 = 2 |\Phi(r)| \quad (2.2)$$

where Φ is the gravitational potential corresponding to a spherical NFW profile [190]. The escape velocities for all 13 outflow galaxies were calculated at $r = 0$ kpc. Calculating escape velocity from the center of a cuspy dark matter halo constitutes an upper limit, as escape velocity decreases with radius. A cored dark matter profile for dwarfs, as has been suggested from observations of some dwarf galaxies [2, 227], will also result on a lower escape speed, facilitating the gas removal. Halo mass predictions and escape velocities for each outflow galaxy are listed in Table 2.1.

Figure 2.9 compares the velocity of the outflow v_{out} to an upper limit of the escape velocity v_{esc} . As discussed in Section 2.3.4, we measure v_{out} in our targets by taking the velocity blueshift corresponding to the 80% width of the detected broad lines plus the offset from the system's velocity (Fig. 2.3). The fit is performed on spectra extracted from within R_{50} . The length of the horizontal arrows in Fig. 2.9 shows the impact of changing the assumption of halo concentration from $c = 15$ to $c = 8$. The symbol sizes in Figs 2.9 and 2.10 are proportional to the percentage of [O III] flux in the outflow (i.e. the ratio of the flux of the broad component to the total [O III] line flux). The velocities plotted in Fig. 2.9

as well as the flux ratios that determine the symbol sizes are listed in Table 2.1 and the details of their calculations can be found in Section 2.3.4.

In all cases the outflow velocities surpass v_{esc} , suggesting that the ionized gas entrained in the outflow will become unbound from the galaxy and, later, its dark matter halo.

2.5.4 Feedback

AGN feedback has been studied extensively at higher masses, invoking winds to explain both suppressing [92, 105] and enhancing [91, 114, 153] effects on star formation. Studies of galaxy evolution placing AGN on the color-mass diagram imply a scenario where AGN mark a sudden transition from blue, star forming galaxies into quiescent red galaxies [199]. A large body of theoretical [167, 312, 305] and observational [270, 218, 96] work has been conducted in the high mass regime to investigate whether AGN can regulate star formation by means of expelling gas or by disrupting cooling flows that would otherwise fall in and fuel star formation.

Figure 2.10 shows that dwarfs with detected outflows associated with AGN (pink circles) have intermediate colors that strike between the blue, actively star forming population, and the redder, quiescent population. Their position is at least qualitatively consistent with the evolutionary scenario proposed at higher masses. Non-AGN star forming galaxies with outflows (cyan triangles) are among the bluest in our sample, as is expected from very young and active stellar populations. In the bluest AGN hosts discussed here, the outflows

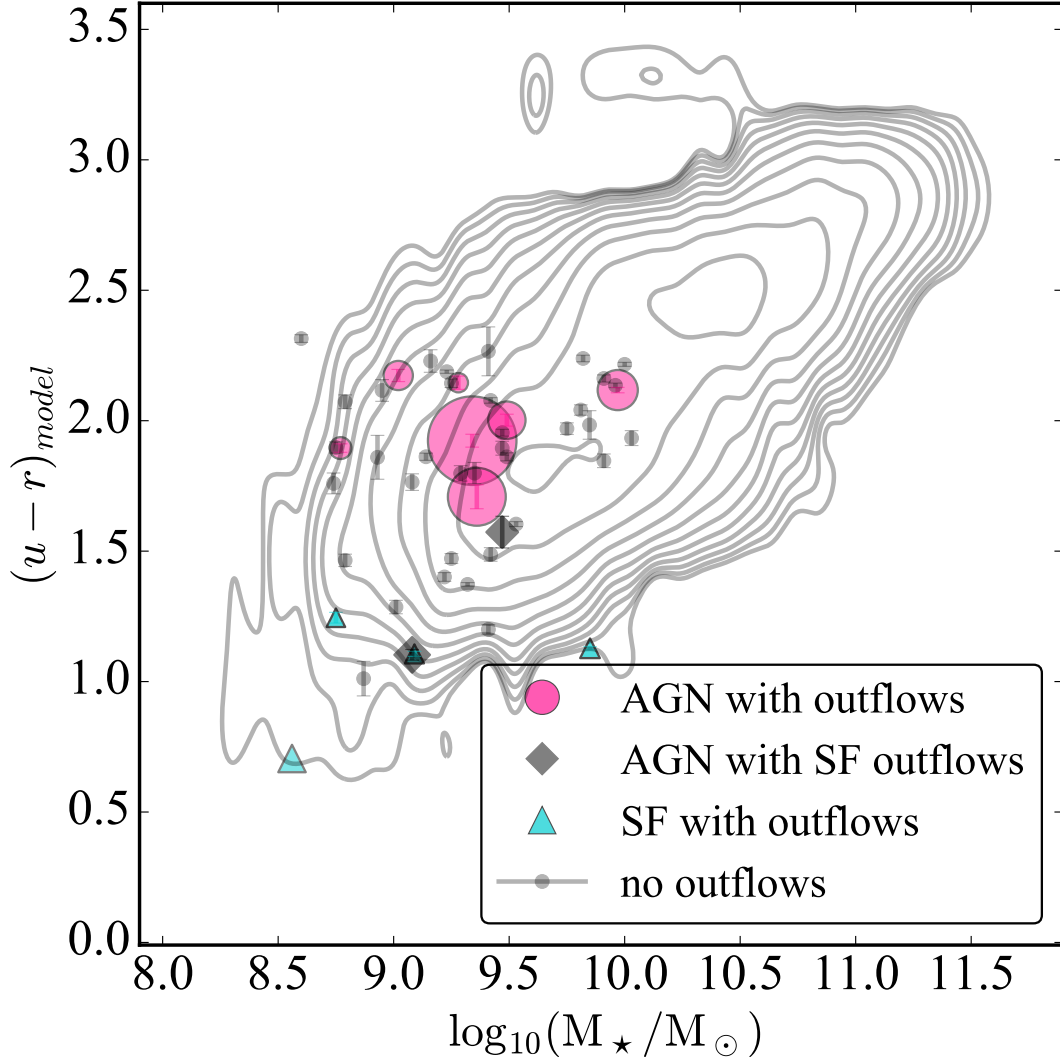


Figure 2.10: The $u - r$ model magnitude colors from SDSS DR 8 are plotted against the MPA-JHU stellar mass. The colors are corrected for galactic extinction, following [280] and the contours are from [278]. The photometry for NGC 1569 were measured in GALEX [124] and converted to SDSS $ugriz$ via the Python code `pysynphot`. The outflow symbol sizes are scaled to the fraction of $[\text{O III}]$ flux contained in the outflows.

appear to be at least partially powered by coincident stellar processes (gray diamonds). These galaxies retain their blue colors despite having fast outflows. This could imply that the outflows are not quenching the star formation, or it could be that the timescale for galaxy color evolution is longer than the specific stage of the outflows at which we are capturing these objects.

In a scenario where AGN-driven outflows suppress star formation, one might expect to find such outflows in redder galaxies. An alternative explanation for this trend is that optically selected AGN are more easily detected in galaxies with lower star formation rates. Though our selection criteria relies exclusively on emission line properties and does not consider photometry at all, contribution to gas ionization from young stellar populations can obscure optical emission line signatures of AGN. Our star forming galaxies lack all available indicators of AGN; however, we cannot definitively rule out the presence of faint AGN activity coincident with active star formation in our control sample.

All of the outflow galaxies discussed here have $H\alpha$ equivalent widths ($EW_{H\alpha}$) well above 3 \AA , and thus cannot be considered retired ($EW_{H\alpha} < 3 \text{ \AA}$) or quenched ($EW_{H\alpha} < 0.5 \text{ \AA}$) [69]. If the presence of outflows does imply removal of all of the gas in the dwarf galaxy, we are likely catching these galaxies in a phase prior to quenching. This is in contrast to other observational work suggesting AGN feedback works to suppress star formation after an initial quenching event, likely due to tidal stripping by a neighboring galaxy [238].

AGN-driven outflows are suspected to play a major role in quenching star formation in the most massive galaxies. The AGN-driven outflow velocities we report in this work are comparable to those measured in some higher mass galaxies (e.g., [140, 258, 15]).

If AGN-powered winds are suspected to quench star formation in those high mass galaxies, the similar wind velocities that we measure could be a plausible quenching mechanism in the dwarf regime as well. The ability of these AGN to quench their host galaxies ultimately depends on the fraction of gas mass involved in the outflow. Due to substantial slit losses and unconstrained electron densities, estimates of outflow gas mass using our current data would span many orders of magnitude. Follow-up observations of two of the AGN presented here and a thorough discussion of mass, kinetic energy, and ionization conditions of the outflows will be presented in a follow up paper (W. Liu et al., in prep.)

2.6 Summary

We have presented the detection and kinematic measurements of extended outflows in isolated dwarf galaxies. Our Keck LRIS longslit data provided spatially resolved spectroscopy, in all cases revealing galaxy-wide winds with velocities exceeding the escape velocities of their dark matter halos. Based on emission line ratios of the outflow components, we found the central AGN to be the dominant driving mechanism in at least six of 13 galaxies. We summarize our conclusions below.

1. Thirteen of 50 dwarf galaxies both with and without optical signs of AGN show galaxy-wide winds. Nine of these 13 galaxies are classified as AGN according to their narrow line flux ratios. The remaining four have no optical or IR signatures of AGN activity and are thus classified as star forming.
2. We were able to measure BPT emission line ratios for the broad components of 12 of the 13 galaxies with outflows. The four galaxies classified as SF based on their

narrow line ratios have outflow line ratios consistent with SF ionization plus some contribution from shocks.

Of the nine AGN, two have outflow line ratios that fall in the BPT composite region, indicating that their outflows might be at least partially powered by star formation.

One AGN had insufficient outflow flux to place it on the BPT diagram. The remaining six AGN have outflow line ratios that exceed the theoretical maximum ionization possible with star formation alone. Therefore, we report the detection of AGN driven outflows in at least six dwarf galaxies.

3. Outflow velocities were measured to be $375\text{--}1090\text{ km s}^{-1}$ for galaxies with and without AGN, ranging in stellar mass $\sim 4 \times 10^8 - 9 \times 10^9 M_{\odot}$. The outflow velocities in all 13 galaxies are sufficient to escape their dark matter halos.
4. SF galaxies and AGN show differences in the line profiles of their outflow components. AGN outflow profiles tend to be more blueshifted and slightly narrower than those of SF galaxies. Outflows with BPT composite line ratios have line profiles similar to those in SF galaxies. We speculate that the differences may be due to the differing physical placement of the wind sources for each of these type of objects.
5. AGN-driven outflows tend to carry a larger fraction (5 – 50%) of the total amount of [O III] flux than the SF outflows (4 – 8%). The outflows carrying the largest fractions of ionized gas tend to populate redder galaxies. The placement of the AGN-driven outflows on the color-mass diagram is suggestive of ongoing star formation suppression due to the influence of the AGN.

The outflow velocities reported here serve as the first directly observed AGN-driven outflows in dwarf galaxies and offer vital observational constraints necessary to extend realistic feedback models into the low mass regime. Detailed observational followup is needed to constrain the gas mass, spatial extent, and energetics of the outflows in these galaxies. Careful consideration of the potential contribution of shock heating to line ratios is also necessary.

Fast outflows exist in a third of the low-mass AGN hosts in our sample of 50 dwarfs, so a systematic search for AGN-driven outflows in a much larger parent sample of dwarf galaxies is warranted.

Acknowledgements

We thank the anonymous referee, whose careful reading and constructive suggestions helped improve and clarify this manuscript. Support for this program was provided by the National Science Foundation, under grant number AST 1817233. Additional support was provided by NASA through a grant from the Space Telescope Science Institute (Program AR- 14582.001-A), which is operated by the Association of Universities for Research in Astronomy, Incorporated, under NASA contract NAS5-26555. LVS acknowledges support from the Hellman Foundation. The data presented herein were obtained at the W. M. Keck Observatory, which is operated as a scientific partnership among the California Institute of Technology, the University of California and the National Aeronautics and Space Administration. The Observatory was made possible by the generous financial support of the W. M. Keck Foundation. The authors wish to recognize and acknowledge the very significant cultural role and reverence that the summit of Mauna Kea has always had within the In-

digenous Hawaiian community. We are most fortunate to have the opportunity to conduct observations from this mountain. Some of the data presented herein were obtained using the UCI Remote Observing Facility, made possible by a generous gift from John and Ruth Ann Evans. This research has made use of the NASA/IPAC Extragalactic Database (NED), which is operated by the Jet Propulsion Laboratory, California Institute of Technology, under contract with the National Aeronautics and Space Administration.

Name (1)	z (2)	M_* (3)	M_{halo} (4)	v_0 (5)	W_{80} (6)	v_{out} (7)	v_{esc} (8)	F_b/F_{tot} (9)	narrow (10)	broad (11)
AGN										
J081145.29+232825.7	0.016	9.02	11.02	-120 ± 11	634 ± 12	437 ± 167	264 ± 29	0.1002	AGN	AGN
J084025.54+181858.9	0.015	9.28	11.13	149 ± 44	1627 ± 44	665 ± 62	290 ± 33	0.0467	AGN	—
J084234.51+031930.7	0.028	9.34	11.17	-72 ± 2.5	607 ± 3.5	375 ± 4.3	299 ± 34	0.5060	Comp	AGN
J090613.75+561015.5	0.045	9.36	11.19	-128 ± 4.4	1147 ± 5.8	701 ± 7.2	303 ± 35	0.3046	AGN	AGN
J095418.16+471725.1	0.032	9.49	11.24	-79 ± 5.4	1280 ± 7.9	719 ± 9.6	317 ± 37	0.1542	AGN	AGN
J100551.19+125740.6	0.0093	9.97	11.49	-176 ± 7.6	1154 ± 8.8	753 ± 17	385 ± 46	0.1740	AGN	AGN
J100935.66+265648.9	0.014	8.77	10.90	-119 ± 9.8	1055 ± 11	646 ± 15	241 ± 26	0.0587	AGN	AGN
AGN w/SF outflows										
J010005.94-011059.0	0.050	9.47	11.24	41 ± 11	929 ± 12	423 ± 16	317 ± 37	0.0616	Comp	Comp
J144252.78+205451.6	0.043	9.08	11.06	-8 ± 23	1201 ± 25	609 ± 34	273 ± 30	0.0765	AGN	Comp
Star Forming										
J101440.21+192448.9	0.028	8.75	10.90	24 ± 14	1114 ± 16	533 ± 21	241 ± 26	0.0431	SF	SF
J130724.63+523715.2	0.026	9.09	11.05	2 ± 22	1442 ± 24	719 ± 33	272 ± 30	0.0452	SF	SF
J171759.66+332003.8	0.015	9.85	11.42	-11 ± 35	1509 ± 36	765 ± 50	365 ± 44	0.0482	SF	SF
NGC 1569	2 Mpc	8.56	10.81	23 ± 8.8	2225 ± 9.4	1090 ± 13	222 ± 23	0.0878	SF	SF

Table 2.1: Details of fits to spectra extracted within R_{50} of each galaxy, unless otherwise specified. (1) Full SDSS names of all 13 galaxies with extended outflows (2) Redshift (3) Stellar mass reported in the MPA-JHU catalog (4) Halo mass determined via abundance matching using the method described in the text and the stellar mass listed in (2) (5) Mean velocity of the outflow, in km s^{-1} , relative to the center of the narrow component (negative=blueshifted) (6) Width containing 80% of the flux of the outflow component, in km s^{-1} . (7) Outflow velocity defined as $v_{\text{out}} = -v_0 + \frac{W_{80}}{2}$, in km s^{-1} (8) Velocity required to escape the dark matter halo (3) with an NFW profile from $r = 0$, in km s^{-1} (9) Fraction of [O III] flux in the outflow, calculated as the ratio of the flux in the broad component, F_b , to the total flux in broad + narrow components, F_{tot} (10,11) Decomposed BPT classifications for the bound and outflowing gas. In order to optimize S/N, these fits were performed on spectra extracted from customized apertures for each galaxy.

Chapter 3

Gas Kinematics

We present spatially resolved kinematic measurements of stellar and ionized gas components of dwarf galaxies in the stellar mass range $10^{8.5} - 10^{10} M_{\odot}$, selected from SDSS DR7 and DR8 and followed-up with Keck/LRIS spectroscopy. We study the potential effects of active galactic nuclei (AGN) on galaxy-wide gas kinematics by comparing rotation curves of 26 galaxies containing AGN, and 19 control galaxies with no optical or infrared signs of AGN. We find a strong association between AGN activity and disturbed gas kinematics in the host galaxies. While star forming galaxies in this sample tend to have orderly gas discs that co-rotate with the stars, 73% of the AGN have disturbed gas. We find five out of 45 galaxies have gaseous components in counter-rotation with their stars, and all galaxies exhibiting counter-rotation contain AGN. Six out of seven isolated galaxies with disturbed ionized gas host AGN. At least three AGN fall clearly below the stellar-halo mass relation, which could be interpreted as evidence for ongoing star formation suppression. Taken together, these results provide new evidence supporting the ability of AGN to influence gas

kinematics and suppress star formation in dwarf galaxies. This further demonstrates the importance of including AGN as a feedback mechanism in galaxy formation models in the low-mass regime.

3.1 Introduction

In the Λ CDM model of structure formation, dark matter halos form from the gravitational collapse of primordial density fluctuations. Within these halos, baryons collapse into a rotating disc with the same angular momentum as the dark matter halo. With sufficient radiative cooling, the gas is able to collapse and form stars, resulting in a co-rotating disc of gas and stars within a dark matter halo with a density profile which can be approximated by a simple formula [219, 220]. On large scales, the Λ CDM model of structure formation agrees well with observations of massive galaxies and clusters.

However, large discrepancies in the low-mass regime raise doubts about Λ CDM. For example, there is a large disagreement between the number of small dark matter halos and observed dwarfs (missing satellite problem, [207, 170]). There is also a conspicuous absence of observed large satellites compared to predictions (too big to fail problem, [245, 40]). Finally, rotation profiles of dwarfs show a variety of inner slopes, indicating a diversity of dark matter halo profiles, many of which are in disagreement with the predicted NFW dark matter density profile (cusp vs. core problem, [111, 288, 224]). These departures from the Λ CDM model have prompted some to look into warm (e.g. [193]) or self-interacting dark matter (e.g. [253]). A promising alternative to re-thinking the nature of dark matter is to investigate the effects of baryonic feedback on star formation.

High resolution simulations conclude that baryonic processes can be used to reconcile the observed properties of dwarf galaxies with Λ CDM [350]. Theoretical work commonly attributes star formation suppression in dwarf galaxies to heating from the UV background during reionization (e.g. [162]), stellar radiation (e.g. [103]), and supernovae feedback (e.g. [150]). Indeed, powerful star-formation driven outflows are observed in starbursting dwarf galaxies [197, 302], and some observational evidence suggests that stellar feedback may dominate in dwarf galaxies [200].

Stellar feedback is only part of the picture, as the role of AGN feedback in dwarfs becomes harder to ignore. Evidence of AGN via optical and infrared (IR) indicators has been detected in hundreds of nearby dwarf galaxies [247, 209, 273, 9, 31]. Kaviraj et al, [164] report the IR-selected AGN occupation fraction in high mass galaxies to be 1 – 3%, while the same criteria yield a 10 – 30% fraction in dwarf galaxies ($M_* \sim 10^{8-10} M_\odot$). Given that there are several factors that hinder the detection of AGN in dwarfs [275, 58], this large AGN fraction can be regarded as a lower limit. These studies suggest that AGN are common and potentially important phenomena in the low mass regime.

Additionally, observational evidence of AGN-driven outflows in dwarf galaxies has begun to surface [238, 41, 93, 195]. Each of these studies present observations of AGN coexisting with kinematically disturbed gas. Such disturbances are distinguished by broadened components in their emission line profiles and velocity measurements indicating gas that is disconnected or even counter-rotating with respect to their stars. For example, [298] (henceforth S19) use data from Illustris [328, 123] to investigate the origin of star-gas counter-rotation in dwarf galaxies. By examining the evolutionary history of simulated

galaxies with counter-rotating gas, they found that such counter-rotating components require removal of the original gas reservoir and re-accretion of new gas, with misaligned angular momentum. S19 identify two plausible mechanisms for gas removal: stripping from an encounter with a neighboring galaxy, or AGN outflow events.

The role of AGN feedback in galaxy formation and evolution is not well understood in general. The shallow potential wells of dwarf galaxies leave them particularly susceptible to feedback, making them ideal laboratories to study how the energy output of an AGN couples to the gas in the host galaxy. The discovery of AGN-driven outflows in the dwarf regime challenges current conceptions of feedback in dwarf galaxies and raises the question of whether the gas in these outflows permanently escapes the halo. In this paper, we explore the connection between AGN and kinematically disturbed gas and present further evidence of AGN feedback in dwarf galaxies.

Throughout the paper we assume the cosmological model $H_0 = 71 \text{ km s}^{-1} \text{ Mpc}^{-1}$, $\Omega_m = 0.27$, and $\Omega_\Lambda = 0.73$.

3.2 Data

Our complete sample contains 50 nearby ($z = 0.05$) dwarf galaxies (roughly $M_\star < 10^{10} M_\odot$) drawn from the Sloan Digital Sky Survey (SDSS). SDSS is 95% complete to r band magnitude of 22.2, which is well below the magnitude range covered in this sample ($r \approx 12 - 17$). Twenty-nine of the galaxies in our sample are classified as AGN based on

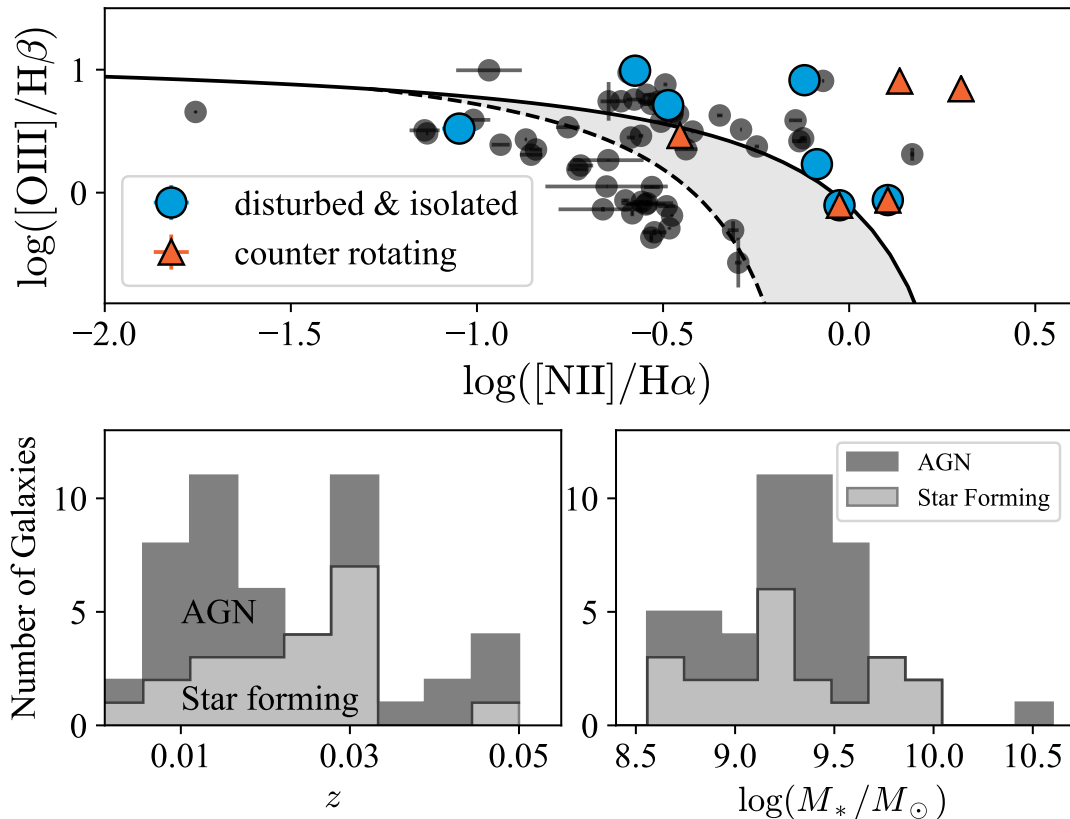


Figure 3.1: Top: BPT diagnostic for all 50 galaxies in this sample. The dotted line denotes the [163] classification cutoff, and the solid line is the [165] maximum starburst line. Blue circles indicate isolated galaxies with disturbed gas and with no neighbors of comparable mass (i.e. the neighboring galaxy is at least 0.75 times the stellar mass of the dwarf) within 1.5 Mpc (see Section 3.4.4). Galaxies with counter-rotating stellar and gas components are marked as orange triangles. Bottom: Stacked histograms of redshift and stellar mass of the galaxies presented in this paper. Dark gray represents AGN hosts and light gray represents star forming galaxies.

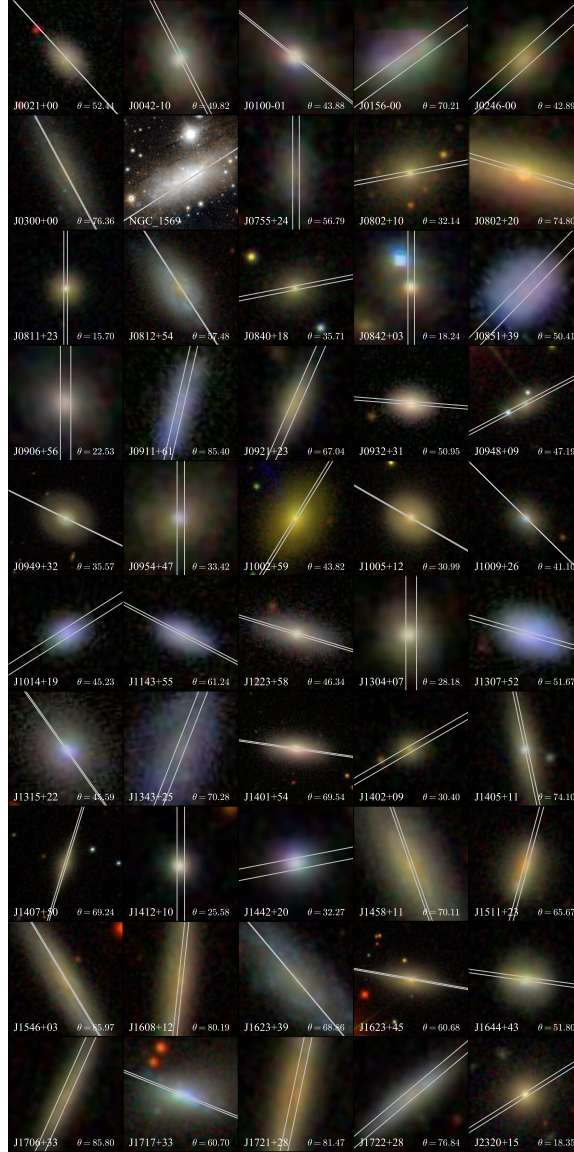


Figure 3.2: colour images of all 50 dwarf galaxies in our sample. All images were generated using the SDSS DR12 finding chart tool, with the exception of NGC 1569, which is outside of the SDSS footprint. The NGC 1569 thumbnail (second row, second column) is a PanSTARS z,g band colour image rendered in the Aladin Lite Viewer with a 3' field of view (~ 1 kpc on a side). Each SDSS image is scaled to 10 kpc on a side and the placement of the 1 arcsecond-wide slit is shown in light gray.

emission line flux ratios that fall above the [163] star forming sequence on the Baldwin, Phillips & Terlevich (BPT) diagnostic [11] or the presence of detectable He II emission [282]. This sample of 29 dwarf galaxies hosting AGN was selected from the parent samples of [247, 209, 273, 225] based on right ascensions that could be observed during our allotted Keck time. In order to facilitate spatially resolved kinematic measurements, we prioritized spatially extended galaxies and excluded face-on galaxies whenever possible.

To enable comparison between galaxies with and without AGN, we selected a control sample of 21 star forming galaxies from SDSS Data Release 8, based on their absence of optical and infrared (IR) signatures of AGN. The control sample was selected by applying the same stellar mass and redshift cuts used to build the AGN sample, then excluding objects with emission line flux ratios falling above the star forming sequence on the BPT diagram. We also excluded all potential AGN using the WISE mid-IR color criteria [155, 299] and further excluded all galaxies with detectable He II emission. The BPT diagnostic diagram and distributions of the redshifts and stellar masses of our full sample are shown in Figure 3.1.

We collected long-slit spectroscopy of 50 galaxies using the Low Resolution Imaging Spectrometer on the Keck I telescope (LRIS, [226, 50]). Observation dates, conditions, and spectrograph setups for each object are listed in Table 3.1. The DIMM seeing (Full Width at Half Maximum value of a star observed at zenith, at 5000\AA) is listed for each night. The slit position angles (PA) were determined by fitting r -band SDSS photometry using the IRAF ellipse task. By placing the slit along the semi-major axes determined by these ellipse fits,

as shown in Figure 3.2, we obtained spatially resolved spectra, presumably perpendicular to the rotation axis of each galaxy.

Name in SDSS	Observation Date	Seeing arcsec	slit PA CCW N	red setup	exposure time s
J002145.80+003327.3	2015-12-05	0.59	42.4	B	1200
J004214.99-104415.0	2015-12-04	0.55	26.9	B	1200
J010005.94-011059.0	2015-12-04	0.55	51.2	B	1200
J015645.30-003737.8	2015-12-04	0.55	126	B	1200
J024656.39-003304.8*	2015-12-04	0.55	131.9	B	1200
J030040.20+000113.3	2015-12-04	0.55	28.3	B	2400
NGC 1569*	2015-12-04	0.55	122.5	B	2400
J075538.19+240103.5	2015-12-04	0.55	0	B	2400
J080212.06+103234.1	2015-12-05	0.59	100.7	B	2400
J080228.83+203050.2	2015-12-04	0.55	73.3	B	2400
J081145.29+232825.7	2015-12-04	0.55	0	B	2400
J081256.37+545808.4	2015-12-05	0.59	32.77	B	1200
J084025.54+181858.9	2015-12-04	0.55	101	B	2400
J084234.51+031930.7	2015-12-05	0.59	0	B	1200
J085125.81+393541.7	2015-03-24	0.70	-43.96	C	1200
J090613.75+561015.5	2015-12-04	0.55	0	B	2400
J091122.24+615245.2	2015-03-24	0.70	-13	C	2400
J092149.44+233438.7	2015-12-05	0.59	156.3	B	1200
J093251.11+314145.0	2015-03-25	0.58	-94.6	B	1200
J094800.79+095815.4	2015-12-05	0.59	117.8	B	1200
J094941.20+321315.9	2015-12-04	0.55	64	B	1200
J095418.16+471725.1	2015-12-05	0.59	0	B	2400
J100200.96+591508.3	2015-12-04	0.55	148.5	B	1200
J100551.19+125740.6	2015-12-04	0.55	60.1	B	1200
J100935.66+265648.9	2015-12-05	0.59	45.5	B	1200
J101440.21+192448.9	2015-03-25	0.58	-57.58	B	1200
J114343.76+550019.2	2015-03-25	0.58	-117.58	B	1200
J122342.82+581446.2*	2015-03-24	0.70	-106.86	C	1200
J130434.92+075505.0	2017-06-24	1.17	0	B	1200

Name in SDSS	Observation Date	Seeing arcsec	slit PA CCW N	red setup	exposure time s
J130724.63+523715.2	2015-03-25	0.58	74.09	B	2400
J131503.77+223522.7*	2015-03-24	0.70	-144.8	C	1200
J134332.09+253157.7	2015-03-24	0.70	-21.33	C	2400
J140116.03+542507.4	2015-03-25	0.58	81.76	B	1200
J140228.72+091856.4	2017-06-24	1.17	120	B	1200
J140510.39+114616.9	2017-06-25	0.85	12	A	1200
J140735.47+503242.7	2017-06-25	0.85	163	A	2400
J141208.47+102953.8	2017-06-24	1.17	0.0	B	1200
J144252.78+205451.6	2017-06-24	1.17	101	B	1200
J145843.39+113745.4	2017-06-25	0.85	19	A	1200
J151116.53+233421.6	2017-06-25	0.85	165	A	1200
J154603.78+031339.4	2017-06-24	1.17	31	B	1200
J160839.57+120038.5	2017-06-25	0.85	174	A	1200
J162307.88+391847.5	2017-06-24	1.17	80	B	1200
J162335.06+454443.6	2017-06-25	0.85	40	A	1200
J164428.48+435904.2	2017-06-24	1.17	82	B	1200
J170639.14+334103.4	2017-06-25	0.85	156	A	1200
J171759.66+332003.8	2017-06-24	1.17	68	B	1200
J172125.92+281134.9	2017-06-24	1.17	168	B	1200
J172208.82+280155.8	2017-06-24	1.17	130	B	1200
J232028.21+150420.9*	2015-12-04	0.55	122.2	B	1200

Table 3.1: LRIS configuration for each object, using the 1" slit placed along the semimajor axis of each galaxy. For the blue side (LRIS-B), we used the 600 groove mm^{-1} grism blazed at 4000Å, yielding a dispersion of 0.63Å pixel^{-1} . We used three setups on the red side (LRIS-R):

- A: 600 groove mm^{-1} grating blazed at 5000Å, 5600Å dichroic, yielding a dispersion of 0.80Å pixel^{-1}
- B: 900 groove mm^{-1} grating blazed at 5500Å, 5600Å dichroic, yielding a dispersion of 0.53Å pixel^{-1}
- C: 1200 groove mm^{-1} grating blazed at 7500Å, 5000Å dichroic, yielding a dispersion of 0.40Å pixel^{-1}

The LRIS data were reduced using a Python pipeline to automate the standard IRAF reduction tasks. Flexure on the red camera was corrected using the average shift in sky lines. Sky lines are sparse in the wavelength range covered by the blue CCD, so each galaxy spectrum on the blue side was redshift-corrected using the redshift measured from the flexure-corrected red spectrum. Flexure on the blue CCD was then calculated by comparing redshift-corrected galaxy emission lines with their expected rest frame values. The longslit spectra were rectified along both the wavelength and spatial axes, yielding 2-dimensional spectra where each pixel row along the spatial axis is a fully reduced 1-dimensional spectrum.

3.3 Analysis

3.3.1 Spatially Resolved Spectra

The longslit spectra have been rectified along both the wavelength and spatial axes, creating a 2D spectrum where each pixel row is a fully reduced 1D spectrum. Much of our analysis depends on fitting subtle spectral features, and thus require high signal to noise (S/N), especially in the dim outskirts of each galaxy. To achieve the required S/N, we spatially bin the spectra, using larger bins on the outskirts of the galaxy, as shown in Figure 3.3.

Spectra were extracted along the slit by summing pixel rows until the target S/N ratio (typically 15–20) or maximum bin size was reached. In order to prevent summing the entire image and losing spatial data, the maximum bin size is set to be 20% of the spatial axis. The signal to noise was measured using the mean and standard deviation of

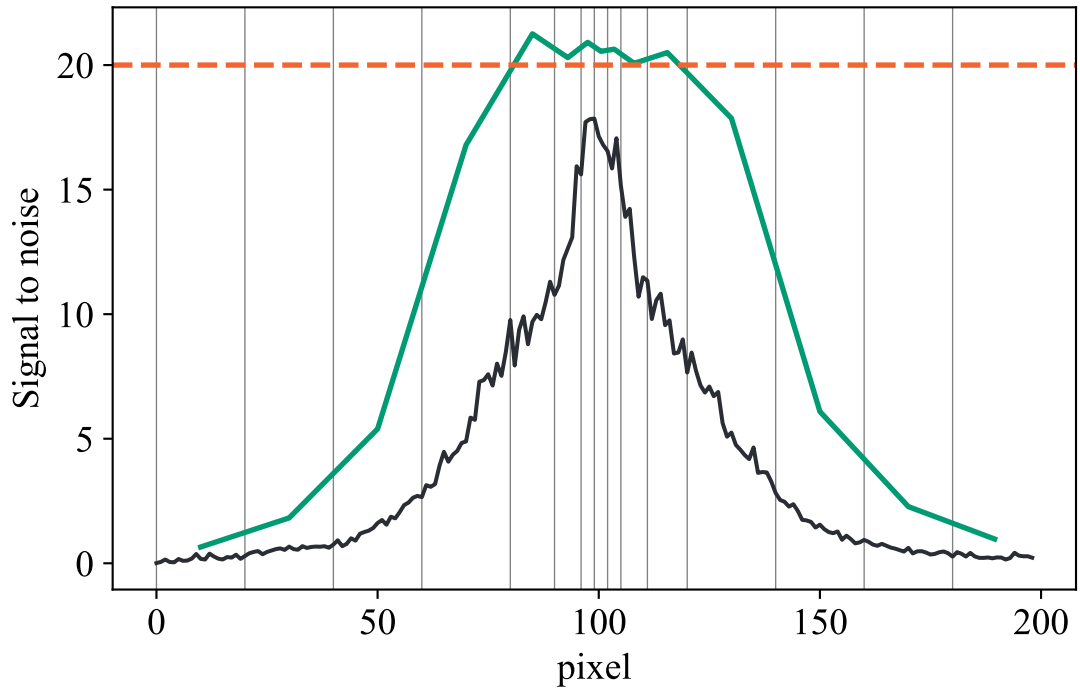


Figure 3.3: Pixel number along the spatial axis is shown on the x axis. The y axis shows the signal to noise ratio of a featureless portion of the spectrum red-ward of $[\text{O III}]\lambda 5007$. Moving along the slit, we summed pixel rows (black) until the integrated spectrum's signal to noise ratio (green) reached the target S/N (red) or the maximum bin size was reached. The minimum bin size is 3 pixel rows, which sometimes results in even higher S/N. Exposure times for each object were chosen with the intention of obtaining sufficient S/N in the outskirts, so the bin size is dependent on the observational setup used.

a relatively featureless portion of the stellar spectrum, just red-ward of $[\text{O III}]\lambda 5007$. The next bin would begin at the central pixel of the last bin. Figure 3.3 shows the signal to noise of each pixel row along the spatial axis (black). Vertical gray lines mark the divisions between bins, and the green line indicates the signal to noise when all pixel rows within each bin is summed.

3.3.2 Emission Line Fluxes

In order to measure accurate emission line fluxes, it is necessary to account for stellar absorption, which primarily affects the Balmer emission lines. The Penalized Pixel-Fitting software (PPXF) [59] is used to fit and subtract the stellar continuum following the method described in [195] (henceforth Paper I), Section 3.1.

After subtracting the best-fitting stellar population model of the galaxy, the residual emission lines were fit using a custom Bayesian MCMC maximum likelihood sampling algorithm, implemented using the Python package *emcee* [113]. A single-Gaussian model was used to fit emission lines for each galaxy in this sample, except in 13 cases when a second Gaussian component was needed (Paper I). In these 13 cases the BPT flux ratios of the narrow component of the emission lines are shown in Figure 3.1 and used when classifying these galaxies as AGN or star forming.

3.3.3 Multi-Component Velocity Measurements

In the PPXF software, emission lines are modeled as Gaussians and fit simultaneously with stellar templates. Each stellar and gas template can be matched to a unique kinematic component, enabling the decomposition of multiple distinct line of sight velocities for stars and various species of emission lines. Each spatially resolved velocity measurement presented in this work consists of three components: stellar, ionized hydrogen, and forbidden gas emission.

To avoid systematic errors introduced by wavelength calibration on the blue CCD, we fit $\sim 1000\text{\AA}$ sections of the spectrum using PPXF. Due to the strength of the $H\beta$ and

[O III] emission lines, and their proximity to the stellar feature MgIb, we measured line of sight velocities using the spectral region at rest wavelength $4500 - 5560\text{\AA}$ whenever favorable. Five galaxies were observed using the 5000\AA dichroic, which disrupts the H β , [O III] region of the spectrum. In these cases, stellar and gas kinematics were measured by fitting the portion of the spectrum containing [O II] and Balmer break ($3650 - 4550\text{\AA}$). In cases where the [O III] lines were faint, the fitting area containing H α , [N II], and [S II] ($6400 - 6800\text{\AA}$) enabled gas velocity measurements to extend to a larger radius than fitting the $4500 - 5560\text{\AA}$ region. An example of fits to these three regions is shown in Figure 3.4.

Thirteen galaxies in our sample have gas profiles that cannot be accurately modeled by a single Gaussian. In these cases, two Gaussian components were used for each emission line: a narrow and a broad. The velocity measurements presented in this work were obtained from the narrow Gaussian components.

3.3.4 Circular Velocity Curves

We extracted spatially resolved spectra along the semimajor axis of each galaxy by summing pixel rows, as described in Section 3.3.1. Multicomponent line of sight velocity measurements were then taken from each spectrum following the method outlined in Section 3.3.3. To convert line of sight velocity measured in PPXF into rotational velocity, we correct for the disc inclination angle (see Appendix A.3). Zero velocity is measured at the galaxy’s kinematic center, which is determined by the point of symmetry in the stellar velocity curve.

Figure 3.5 shows the resulting rotational velocity curve for J170639.14+334103.4 as an example. Stellar velocity measurements are plotted as gray stars and the ionized gas

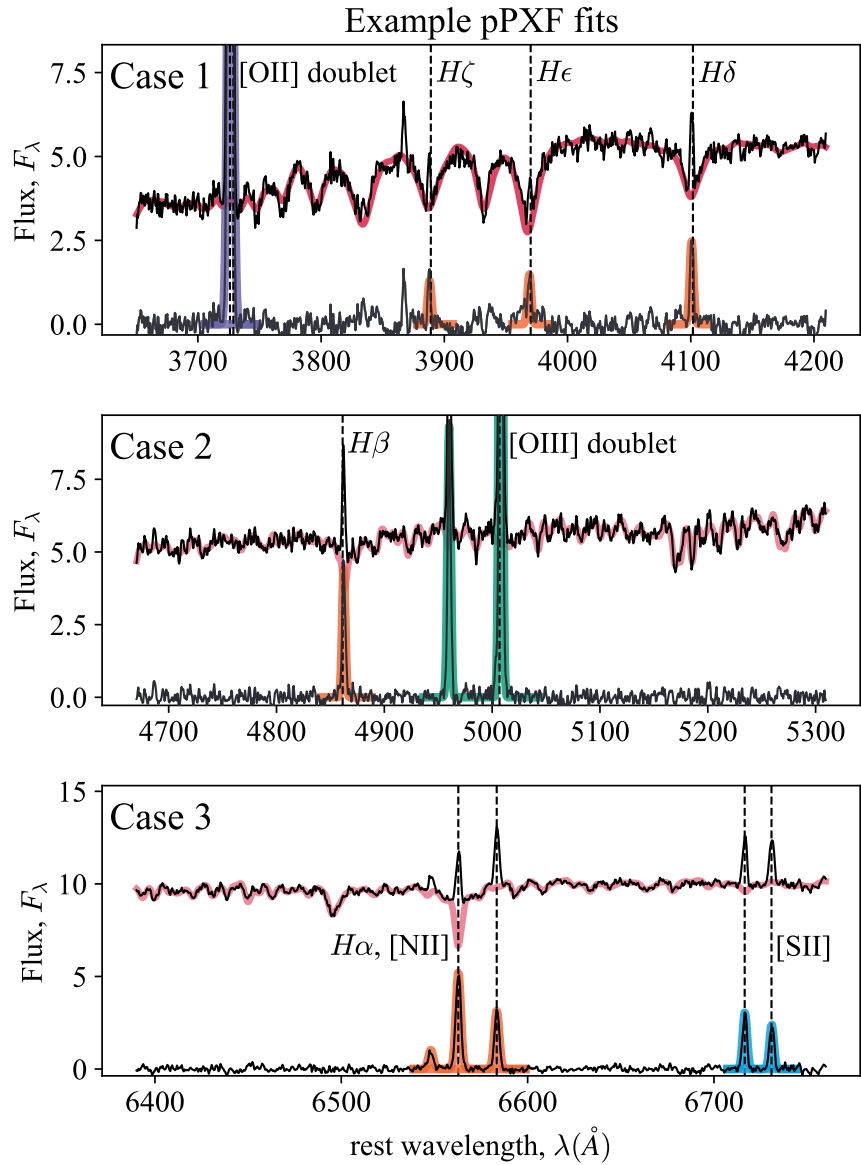


Figure 3.4: Example pPXF fits to each of the three spectral sections used to determine velocity curves. Each velocity curve consists of three components: stellar (red), hydrogen (orange), and forbidden (purple, green, and blue).

velocities for $H\beta$ and $[O\ III]$ are shown as orange and teal circles, respectively. r_{50} refers to the 50% SDSS r-band Petrosian radius. The gray shaded region shows the analytic prediction of the rotation curve assuming the dark matter halo follows an NFW density profile (see Section 3.4.1).

3.4 Results

We obtained circular velocity curves for the stellar and ionized gas components of all 50 galaxies. Five galaxies are excluded from the rest of this analysis based on the limited spatial extent of their stellar velocity curves. For three galaxies (J024656.39-003304.8, J131503.77+223522.7, and J232028.21+150420.9), the spatial extent of their velocity curves were comparable (within 0.3 arcsec) with the seeing. NGC 1569 was excluded because the slit only covered the central 0.25 kpc of the galaxy. J122342.82+581446.2 was excluded because we were unable to achieve a sufficient S/N ratio to obtain more than two stellar velocity measurements. Rotation curves for the remaining 45 galaxies (26 AGN and 19 star forming) included in this analysis are shown in Appendix A.4.

3.4.1 Comparison with NFW

The Λ CDM model predicts that dark matter halos will follow an NFW profile, where the density steepens quickly in the inner regions and more slowly in the outer regions, forming a ‘cusp’ profile. However, observed dwarf galaxy rotation curves show a variety of slopes in their velocity profiles, some of which rise linearly with radius [227], implying

Rotation Curve Example

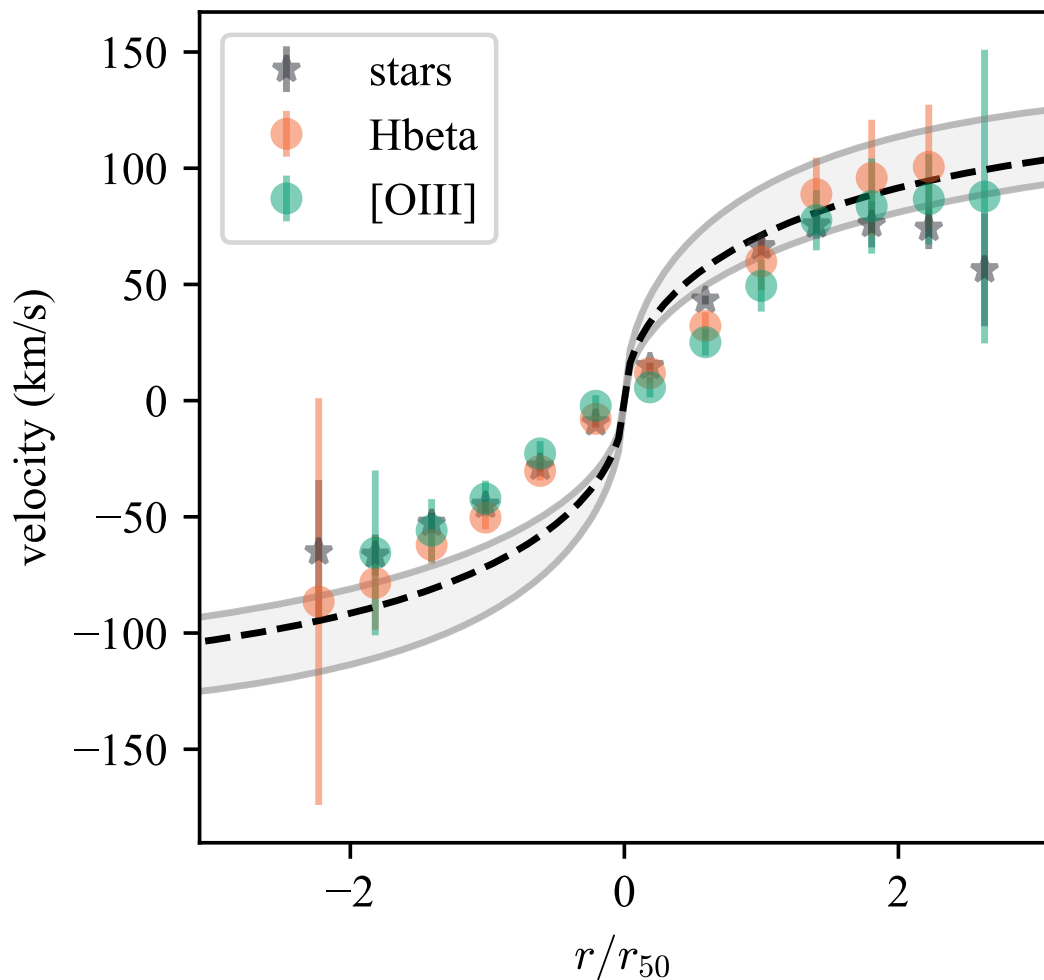


Figure 3.5: The object J170639.14+334103.4 was chosen randomly from our sample to provide an example of an orderly rotation curve, with a co-rotating disc of gas and stars. The stellar (gray stars), $H\beta$ (orange circles) and $[O\ III]$ (teal circles) velocities are shown as a function of normalized radius, where r_{50} is the r-band Petrosian 50% radius. The dotted black line indicates the expected velocity curve for an NFW profile with concentration parameter $c = 10$. The shaded gray region represents the NFW curve expected from halos with concentration parameter $c = 8 - 15$.

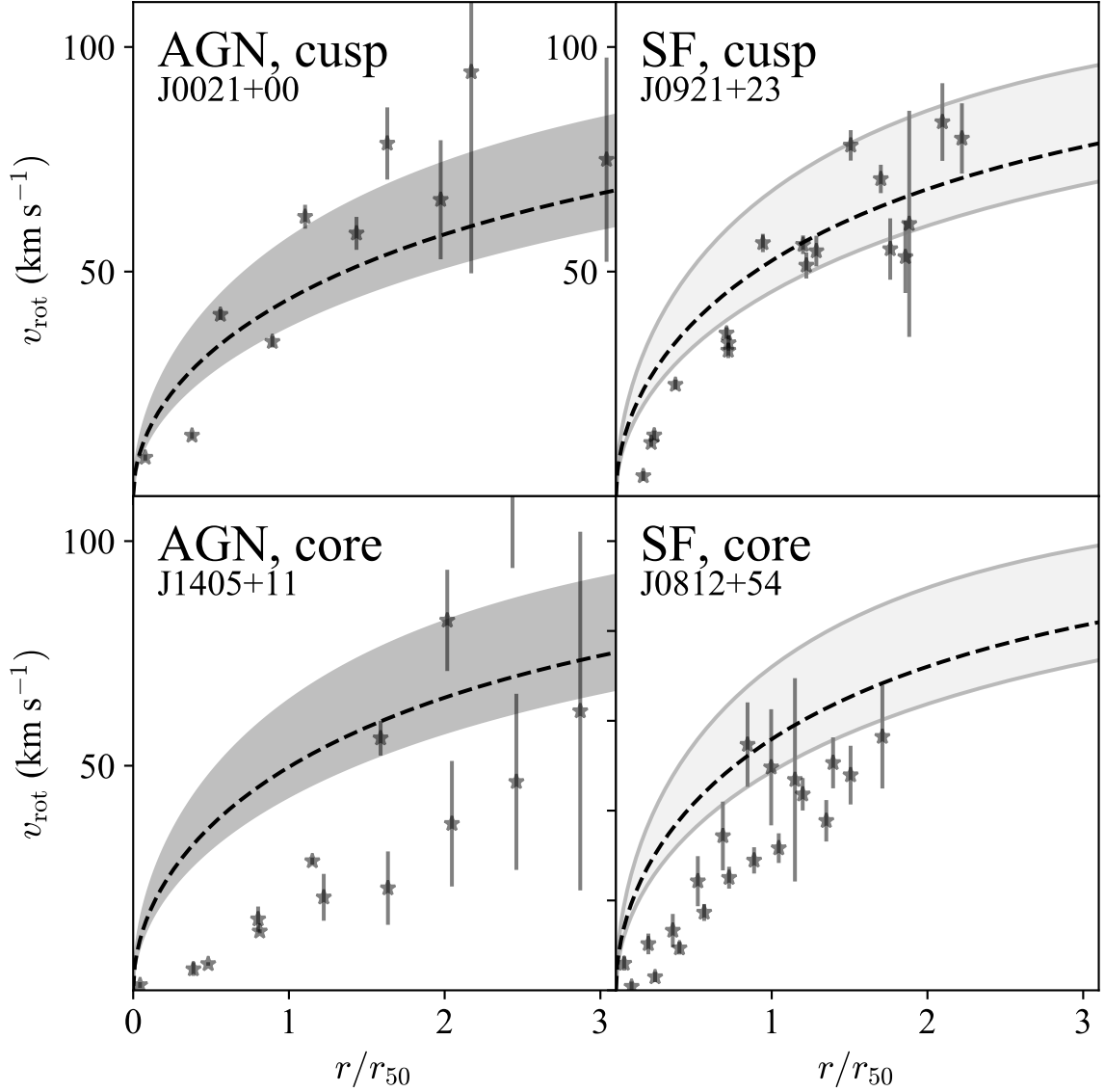


Figure 3.6: Four stellar absolute circular velocity curves are shown to demonstrate the variety of inner slopes found in our sample. Two examples of AGN are displayed in the left panels and two star forming galaxies are shown on the right. Dashed black lines and shaded gray regions represent NFW velocity curves corresponding to a halo mass determined by abundance matching, with the MPA-JHU stellar mass as input. Stellar velocity curves showing agreement with the expected NFW profile are shown on the top two panels. The velocity profiles in the bottom panels rise slowly, indicating cored dark matter density profiles.

underdense dark matter, or ‘cores,’ in some galactic centers. This diversity in inferred dark matter profiles reported in a large number of observational studies and is yet to be explained by baryonic feedback models (e.g. [272]). Since both AGN and stellar feedback have been shown to move large quantities of gas, and thus would be capable of altering the dark matter distribution of their host galaxies (e.g. [127, 201]), the process of forming cores might be a complex interplay between multiple feedback modes. Any observed association between velocity curve shapes and AGN activity could help disentangle role of AGN in shaping dwarf galaxy dark matter halos.

To aid in visual identification of cores in our sample, we plot the NFW velocity curve of a Λ CDM halo corresponding to the predicted halo mass of each galaxy as gray shaded regions in Figures 3.5, 3.6, and all other velocity curve plots in Appendix A.4.

It is difficult to observationally constrain the halo mass of a galaxy, so one popular approach is to use abundance matching (e.g. [212]). Abundance matching assumes a monotonic relation between stellar and halo mass and matches the cumulative abundance of galaxies on that relation. We used abundance matching to estimate the halo mass corresponding to each galaxy’s stellar mass reported in the MPA-JHU catalogue [44, 163, 314]. The only observational input is the stellar mass M_* , so the halo mass M_h can be estimated using abundance matching ([212], Equation 2):

$$M_* = M_h \left[2N \left(\frac{M_*}{M_1} \right)^{-\beta} + \left(\frac{M_h}{M_1} \right)^\gamma \right]^{-1} \quad (3.1)$$

with four free parameters: N , the normalization parameter, a characteristic mass M_1 and low and high mass slopes β and γ .

From these estimated halo masses, we estimate a virial radius

$$r_v = \left(\frac{3}{4} \frac{M_h}{\pi v \rho_c^0} \right)^{1/3} \quad (3.2)$$

where $v = 200$ km/s, and $\rho_c^0 = 277.5 M_\odot/\text{kpc}$. Assuming an NFW dark matter density profile, we construct a radial mass distribution ([190], Equation 8):

$$M(r) = g(c) \left[\ln(1 + cs) - \frac{cs}{1 + cs} \right] M_h \quad (3.3)$$

where c is the concentration parameter, $s = r/r_v$, and $g(c) = [\ln(1+c) - c/(1+c)]^{-1}$.

We estimate the circular velocity curve from the radial mass distribution using $v(r) = \sqrt{GM(r)/r}$. The dotted black line in Figure 3.5 represents the rotation curve expected with an NFW profile with concentration parameter $c = 10$, and the shaded gray region was calculated assuming a concentration parameter between $c = 8, 15$.

There is no clear correlation between rotational velocity slopes and AGN activity in our sample. Figure 3.6 shows examples of two AGN and two star forming stellar absolute velocity curves in varying levels of agreement with their predicted NFW profiles. The lack of any association between current AGN activity and central mass deficits could be attributed to a difference in time scales for AGN activity and core formation, or a number of other proposed factors not related to AGN (e.g. [88]). A solution to the cusp-core dilemma appears to be beyond the scope of this work, and it remains to be seen whether AGN play a role in carving out cores in dwarf galaxies.

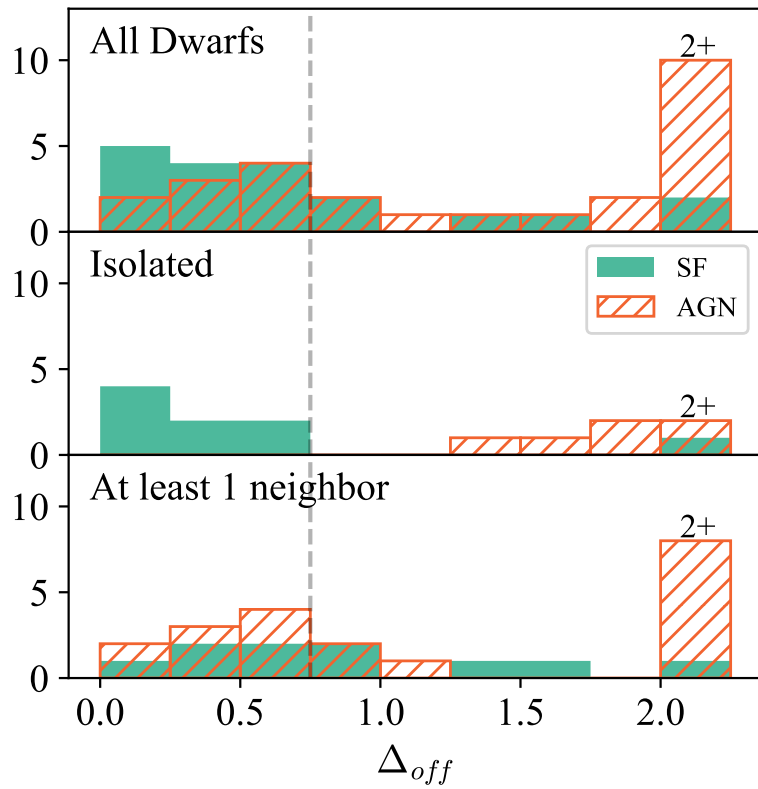


Figure 3.7: We define Δ_{off} to be the weighted absolute average of the velocity offset between stars and gas, divided by the average absolute stellar velocity. This metric is used to quantify the degree of separation between the stellar and forbidden gas component. Based on the bimodal distribution of Δ_{off} in our sample, we consider galaxies $\Delta_{off} \geq 0.75$ to have kinematically disturbed gas.

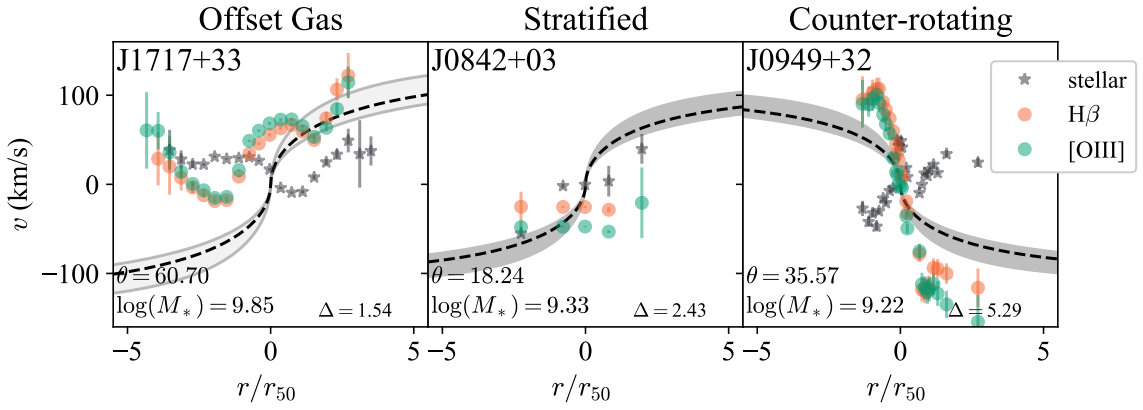


Figure 3.8: Examples of rotation curves where the gas is disturbed in different ways. In some instances, gas is offset from the stars without showing any clear sign of rotation (left). Some AGN have stratified narrow line components, where the Balmer and forbidden lines are kinematically distinct from one another (center). Five galaxies in our sample have gas and stellar discs rotating separately, and sometimes in opposite directions (right).

3.4.2 Peculiar Gas

The gas in these dwarfs show several distinct indications of non-rotational motion, which could be interpreted as inflows, outflows, or recently accreted gas. To identify disturbed gas kinematics, we designed a metric to quantify the relative offset between the gas and stellar rotation curves. Δ_{off} is the weighted average of the absolute velocity offset between the stellar and gas component, divided by the average absolute stellar velocity.

$$\Delta_{\text{off}} = \frac{|\bar{\Delta}_v|}{|\bar{v}_*|} \quad (3.4)$$

where the weighted average of the absolute velocity offset is

$$|\bar{\Delta}_v| = \frac{\sum_i |v_{*,i} - v_{\text{gas},i}| w_i}{\sum_i w_i} \quad (3.5)$$

and the weights are the inverse of the combined errors of each velocity measurement, $w_i = (\Delta v_{*,i}^2 + \Delta v_{\text{gas},i}^2)^{-\frac{1}{2}}$

This calculation considers the offset between the stellar and forbidden gas component because the [O II], [O III], and [S II] doublets are less affected by the subtraction of the stellar continuum and absorption than Balmer lines. Faint broad lines associated with the AGN may also contribute to the line profiles, adding further uncertainty in velocities measured using Balmer emission lines. The forbidden [O II], [O III], and [S II] doublets are not affected by such absorption or broad line region features and therefore give more accurate velocity measurements.

Histograms of Δ_{off} are shown in Figure 3.7 and individual Δ_{off} values are reported in the figures for each galaxy in Appendix A.4. The top panel shows Δ_{off} for all 45 galaxies with rotation curves, the middle panel shows the distribution for all isolated galaxies, and the bottom shows the distribution for all galaxies that have at least one neighbor of comparable (or greater) mass (see Section 3.4.4 for a discussion on galaxy environment). The histograms show a bimodal distribution, which is most pronounced in the middle panel. Based on this bimodality, we classify a galaxy as ‘disturbed’ when $\Delta_{\text{off}} \geq 0.75$ (dotted gray line).

Two galaxies (J010005.94-011059.0 and J090613.75+561015.5) have $\Delta_{\text{off}} < 0.75$ between the stars and forbidden emission lines, but the Balmer and forbidden gas components are offset from one another. Following the same approach, we determine the threshold for offset Balmer and forbidden emission components to be ($\text{H}\beta - [\text{O III}] \Delta_{\text{off}} > 0.5$). Distinct kinematics associated with higher ionization emission lines is known as line stratification

(see Section 3.4.2), and we count galaxies with stratified emission lines among the galaxies with disturbed gas. By this criteria, 25 of the 45 galaxies with rotation curves are disturbed. All rotation curves are plotted in Appendix A.4. The rotation curves showing orderly, co-rotating discs are shown in Figure A.3 and 25 disturbed rotation curves are shown in Figure A.4.

Of the 25 galaxies with disturbed gas, 19 host AGN and 6 do not. The majority (73%) the AGN in our sample have disturbed gas, while only 32% of star forming galaxies have $\Delta_{\text{off}} > 0.75$. We noticed distinct properties in the non-rotational motion exhibited in the disturbed gas, and we show examples of rotation curves exhibiting different types of disturbances. We observe gas that is generally offset from the stellar component, stratified emission lines, and counter-rotating gas. Examples of each type of disturbance are shown in Figure 3.8.

Line Stratification

In the stratified model of the narrow line region (NLR), lower ionization gas resides on the outer parts of the NLR while higher ionization lines are generated closer to the AGN (e.g. [81, 5]). Distinct kinematics associated with emission lines of different ionization potentials imply a complex narrow line region that is stratified in ionization and wind speed. We observe stratified gas components in seven AGN in our sample, with higher ionization lines showing higher velocities than lower ionization lines. This implies a decelerating outflow: where a high velocity, high ionization wind is generated near the AGN, and while the low ionization gas in the outer region of the NLR flows more slowly.

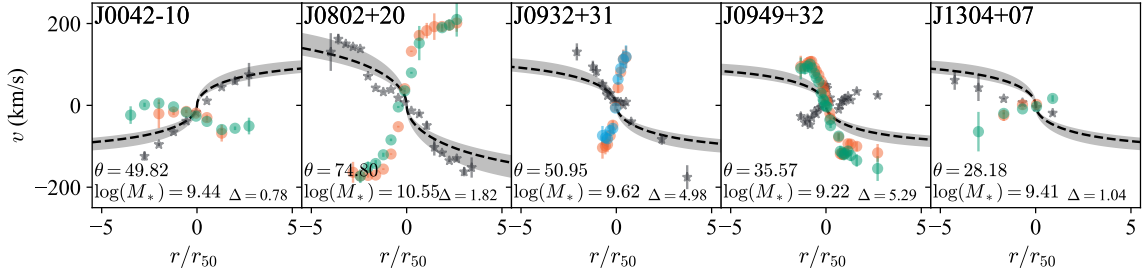


Figure 3.9: The rotation curves for five galaxies with counter-rotating gas are shown here. The colours are as in Figure 3.8, and the blue dots in the middle panel indicate gas velocities measured from the [SII] doublet.

We observe no correlation between wind speed and AGN luminosity, though the line stratification we observe in these seven galaxies preferentially occurs in galaxies that have outflows indicated by broad [O III] components. Plots of the stratified gas kinematics in these seven galaxies can be found in the Appendix, Figure A.5.

Counter-Rotating

Of the 45 galaxies with rotation curves, five have counter-rotating gas and stellar components, shown in Figure 3.9. Counter rotating gas and stars have long been explained as the effect of the accretion of gas clouds or small satellites after the formation of the stellar disc (e.g. [307, 309, 161]). As mentioned in the introduction, S19 found that counter-rotating gas in dwarf galaxies requires substantial gas removal, either via black hole feedback or environmental effects from fly-by interactions with more massive systems. Interestingly, all five counter-rotating dwarfs in our sample host AGN.

S19 also make several predictions about the present-day properties of counter-rotating dwarfs. In cases where re-accretion of gas is gradual, they find that counter-rotation can be very long lived (up to ~ 2 Gyr). As a result, S19 predict no significant correla-

tion with environment. Three counter-rotating galaxies are isolated (J004214.99-104415.0, J080228.83+203050.2, J093251.11+314145.0) and two (J094941.20+321315.9, J130434.92+075505.0) have at least one neighbor with comparable mass.

An event that removes most of the original gas reservoir would quench star formation, making it likely that counter-rotating dwarfs will have older stellar populations and appear redder in colour. All five counter-rotating galaxies discussed here have colours $u-r > 2$, which is redder than the average for our sample ($u-r = 1.83$). S19 also find a 30% gas deficit in counter-rotating dwarfs at $z = 0$, relative to control galaxies at fixed stellar mass. Though most of the galaxies in our sample lack gas mass estimates, we can turn our attention to the six galaxies with HI masses measured in the ALFALFA survey [41]. Of these six, five are not disturbed and one is counter-rotating (J094941.20+321315.9). The five co-rotating galaxies with HI measurements have a wide range of gas fractions ($\frac{M_{HI}}{M_*} \sim 0.23 - 7.3$), and the one counter-rotating has the smallest gas fraction ($\frac{M_{HI}}{M_*} = 0.16$). The gas component of J094941.20+321315.9 reaches velocities that exceed the predicted NFW curve, suggesting that this galaxy inhabits a more massive halo than predicted from its stellar mass.

3.4.3 Star Formation Suppression

While abundance matching enables us to infer halo masses based on stellar masses, maximum line of sight velocity measurements can be used to place lower limits on the true halo mass of each galaxy. If the measured lower limit of the halo mass of a galaxy exceeds the halo mass inferred from abundance matching to stellar mass, the galaxy can be said to have a lower star formation rate than expected. Figure 3.10 shows absolute line of

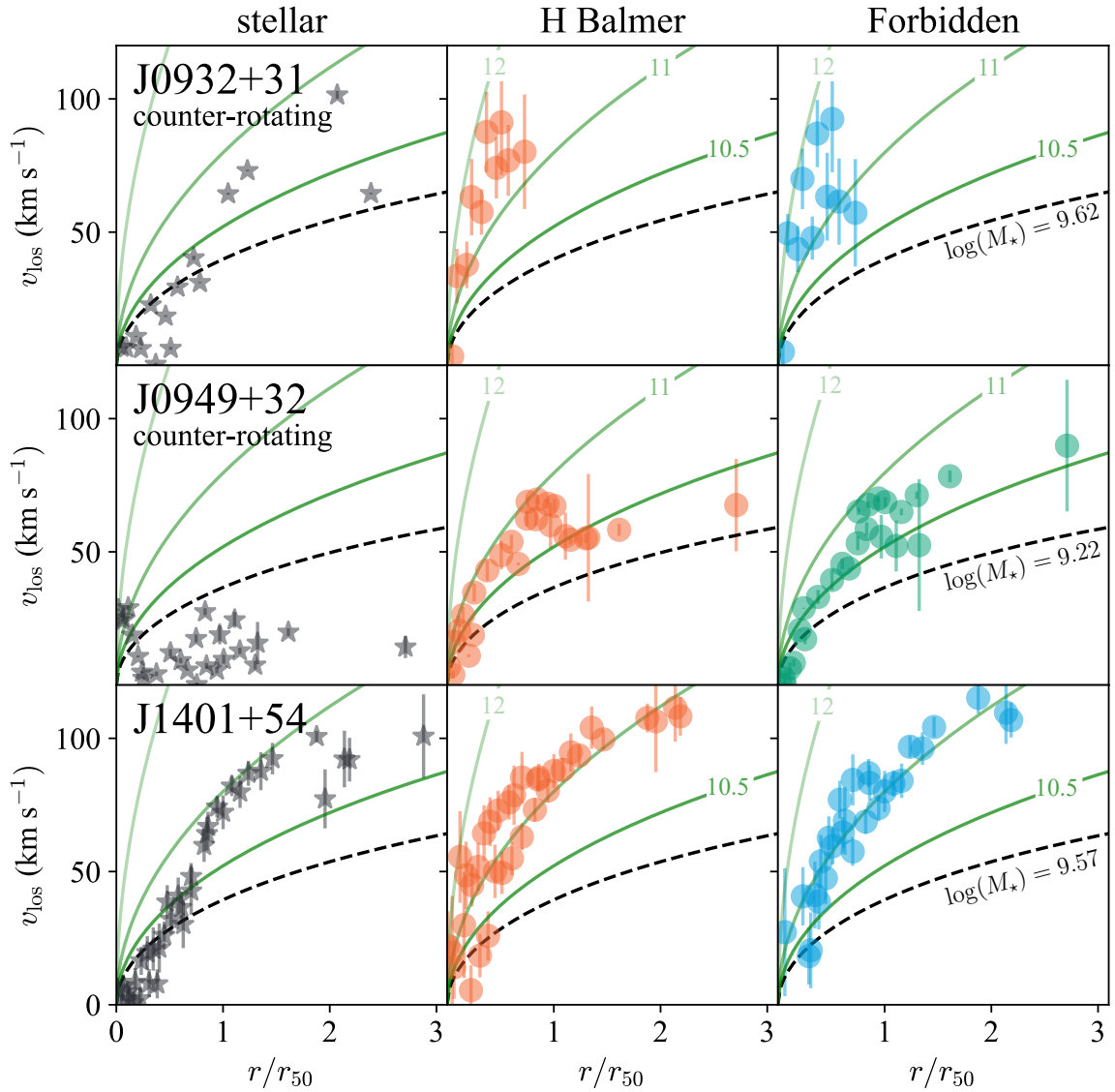


Figure 3.10: Absolute line of sight velocity (v_{los}) measurements that far exceed the expected NFW velocity curves based on their stellar masses indicate overmassive dark matter haloes relative to the measured stellar mass, implying ongoing star formation suppression. Stellar (left), Balmer emission (center) and forbidden emission (right) components are shown for the three galaxies in our sample where this is most apparent. Green curves mark expected NFW velocity curves for galaxies with stellar mass $\log(M_{\star}) = 10.5, 11,$ and 12 and concentration parameter $c = 10$. Black dotted lines denote the expected NFW velocity curves based on each galaxy’s MPA-JHU stellar mass. All three of these galaxies host AGN, and two have counter-rotating gas components, which lends additional evidence potentially associating AGN with gas depletion and star formation suppression in dwarf galaxies.

sight velocity curves for the three galaxies in our sample where this is most apparent. As in previous figures, black dotted lines indicate the NFW curve predicted based on each galaxy’s stellar mass. Green curves mark the NFW curves associated with stellar masses $\log(M_*/M_\odot) = 10.5, 11, \text{ and } 12$ and concentration parameter $c = 10$. The absolute line of sight velocity curves for the stellar (left), hydrogen Balmer emission (middle), and forbidden emission (right) components are shown. Line of sight velocities are plotted here in place of circular velocities to avoid errors introduced when correcting for disc inclination (Appendix A.3).

The three galaxies shown in Figure 3.10 were selected from our sample using a similar approach to the one used to identify disturbed gas in Section 3.4.2. We calculated the offset between each kinematic component (v_{los}) and the predicted NFW curve v_{NFW} :

$$\Delta_{v_{\text{los}}, \text{NFW}} = \frac{\sum_i (v_{\text{los},i} - v_{\text{NFW}}) w_{\text{los},i}}{\sum_i w_{\text{los},i}} \quad (3.6)$$

The distribution of $\Delta_{v_{\text{los}}, \text{NFW}}$ values for each component revealed three outlying galaxies that consistently fell above the threshold $\Delta_{v_{\text{los}}, \text{NFW}} > 0.5$: J093251.11+314145.0, J094941.20+321315.9, and J140116.03+542507.4.

These galaxies have measured velocity curves that far exceed the expected NFW profile, indicating that they inhabit much larger halos than expected based on their stellar masses. Their small stellar masses and red colours ($u - r \geq 2.23$) suggest ongoing or recent star formation suppression. It is interesting to note that all three galaxies host AGN, and two have counter-rotating gas, consistent with the scenario where AGN clear a substantial amount of gas from their hosts, limiting star formation.

3.4.4 Environment

To distinguish between the effects of environmental and secular processes on gas kinematics, we searched for luminous galaxies in the regions surrounding each dwarf. Following the method and criteria employed by [154], we queried the SDSS DR12 and 2MASS Redshift survey catalogues for luminous neighbors with $M_{K_S} < -21.5$ mag and SDSS $r < -16$ mag. The completeness limit of this search is $M_{K_S} = -21.5$ mag at $z = 0.02$; corresponding to $M_* \sim 8 \times 10^9 M_\odot$ [122]. This limit is well below the magnitudes expected for galaxies in the mass range explored in this work, so extending the search to the redshift limit of our sample ($z = 0.05$) has no effect on completeness. The 2MASS Redshift Survey search revealed matches overlooked in the SDSS search due to missing redshifts, but SDSS optical counterparts existed for all 2MASS matches. We use SDSS DR12 g- and r-band photometry and the mass-magnitude relation of [30] to estimate the masses of neighboring galaxies.

We identify galaxies within 1.5 Mpc and ± 1000 km s⁻¹ of each dwarf in this sample as neighbors. Using the g- and r-band mass-magnitude relation, we estimate the mass of each neighbor. In order to identify isolated galaxies, we count the number of neighbors with comparable mass (i.e. stellar mass $M_{*,\text{neighbor}} \geq 0.75 \times M_{\odot,\text{dwarf}}$) within 1.5 Mpc and ± 1000 km s⁻¹. The number of neighbors for each dwarf can be found in Table 3.2.

A recent study of 62,258 dwarf ($M_* < 5 \times 10^9 M_\odot$) galaxies finds no discernible difference between the environments of AGN and non-AGN dwarf galaxies, suggesting that environmental factors may not play a dominant role in triggering AGN [177]. Similarly, we

find no statistically significant link between AGN and environment. However, [177] suggest that remnants of past interactions may be reflected in gas kinematics.

The importance of environment in disturbing gas kinematics can be explored by considering the bottom panel of Figure 3.7, which shows the distribution of Δ_{off} for galaxies with at least one neighbor of comparable (or greater) mass within 1.5 Mpc. Star forming and AGN-hosting galaxies with neighbors show varying degrees of gas disturbance, further supporting the notion that environment may not play a dominant role in triggering AGN activity. The most extreme values of Δ_{off} are associated with AGN, suggesting that AGN are capable of generating large scale disturbances in their host galaxies' ISM, though the presence of AGN-hosting galaxies with undisturbed gas implies this is not always the case.

On the other hand, isolated galaxies show a distinct bimodal distribution, where star forming galaxies tend to have orderly rotating discs, and disturbed gas is almost always associated with AGN. Table 3.3 lists the seven disturbed, isolated galaxies, six of which host AGN. Two of these six isolated AGN have counter rotating gas, and three have outflows indicated by distinct broadened components in $[\text{O III}]\lambda 5007$, as in Paper I. To clarify, the outflows in these four galaxies are identified with multicomponent Gaussian fits to the $[\text{O III}]$ line profile; disturbed gas is determined here by a velocity offset between the narrow component of the emission lines from the stellar component.

The single isolated and disturbed star forming galaxy, J101440.21+192448.9, was originally included in our sample based on broad lines in $\text{H}\alpha$ [247], which later faded, likely due to transient stellar activity [8]. This object is classified as an outflow galaxy in Paper I based on broadened wings in its $[\text{O III}]$ emission line profile. Follow-up Integral Field Unit

(IFU) observations with KCWI revealed that the rotation axis of J101440.21+192448.9 is in fact parallel to the slit position in our LRIS observations (Liu et al., in prep). Since the slit is not aligned with the stellar disc, these velocity measurements do not reflect the true rotational velocity of this galaxy.

Follow-up KCWI observations were obtained for eight objects in this sample (Liu et al., in prep). These IFU observations produce line of sight velocities that agree with our longslit measurements and confirm that in all other cases, the LRIS slit was oriented perpendicular to the rotational axes, as intended. Proper slit orientation for the remainder of the sample should be verified with similar follow-up IFU observations, though the confirmation of correct slit placement in all but one galaxy is encouraging. Since J101440.21+192448.9 is an active star forming galaxy with supernova-driven outflows, it is reasonable to surmise that bright star forming regions could outshine the rest of the disc, confusing the photometric fit used to determine slit placement. This calls into question the slit placement for other galaxies with non-rotational kinematics and signs of active star formation, such as J171759.66+332003.8.

3.5 Summary

From Keck LRIS longslit spectroscopy, we measured rotational velocity curves of 45 dwarf galaxies. Our sample consists of 26 galaxies with AGN and a control sample of 19 star forming galaxies with no optical or IR evidence of AGN. The rotation curves are

Abbreviated Name	Redshift	$\log(M_*)$	$\log(M_{\text{BH}})$	r_{50} (kpc)	BPT	HeII	neigh- bors	dist- urbed	counter- rotating	outflow	strat- ified
(1)	(2)	(3)	(4)	(5)	(6)	(7)	(8)	(9)	(10)	(11)	(12)
J0021+00	0.0180	9.15	—	0.89	AGN	AGN	7	—	—	—	—
J0042-10	0.0359	9.44	—	1.34	AGN	AGN	5	x	x	—	—
J0100-01	0.0515	9.44	—	0.99	Comp.	Comp.	5	x	—	x	—
J0156-00	0.0450	9.39	—	1.91	SF	SF	13	x	—	—	—
J0246-00	0.0464	9.35	5.7 ^c	1.34	AGN	AGN	37	—	—	—	—
J0300+00	0.0095	8.72	—	2.11	SF	SF	0	—	—	—	—
NGC 1569	—80 km s ⁻¹	8.56	—	7.09	SF	SF	—	—	—	x	—
J0755+24	0.0290	8.85	—	1.78	SF	SF	3	—	—	—	—
J0802+10	0.0145	9.60	3.6 ^b	1.29	AGN	AGN	3	—	—	—	—
J0802+20	0.0286	10.6	—	1.97	Comp.	AGN	0	x	x	—	—
J0811+23	0.0157	9.06	4.4 ^c	0.58	AGN	AGN	2	x	—	x	x
J0812+54	0.0086	9.29	—	1.49	SF	SF	0	—	—	—	—
J0840+18	0.0149	9.13	4.3 ^c	0.94	AGN	AGN	2	x	—	x	—
J0842+03	0.0289	9.33	—	0.75	Comp.	AGN	2	x	—	x	x
J0851+39	0.0407	9.28	5.4 ^c	1.70	AGN	AGN	2	—	—	—	—
J0906+56	0.0465	9.37	5.4 ^c	1.51	AGN	AGN	5	x	—	x	—
J0911+61	0.0263	8.95	—	2.03	SF	SF	7	x	—	—	—
J0921+23	0.0281	9.27	—	1.27	SF	SF	0	—	—	—	—
J0932+31	0.0153	9.62	3.5 ^b	0.58	AGN	AGN	0	x	x	—	—
J0948+09	0.0103	8.73	4.2 ^b	0.73	Comp.	AGN	5	x	—	—	x
J0949+32	0.0051	9.22	4.1 ^b	0.58	Comp.	AGN	6	x	x	—	—
J0954+47	0.0326	9.47	4.9 ^c	1.75	AGN	AGN	0	x	—	x	—
J1002+59	0.0093	9.60	4.1 ^b	1.12	AGN	Comp.	1	x	—	—	x
J1005+12	0.0093	9.64	4.8 ^b	0.97	AGN	AGN	0	x	—	x	—
J1009+26	0.0143	8.75	5.1 ^c	0.62	AGN	AGN	0	x	—	x	—
J1014+19	0.0284	8.56	—	0.88	SF	SF	0	x	—	x	—
J1143+55	0.0269	8.92	—	1.03	SF	SF	1	—	—	—	—
J1223+58	0.0146	9.39	6.1 ^b	1.01	AGN	AGN	6	—	—	—	—
J1304+07	0.0479	9.41	—	1.13	AGN	AGN	16	x	x	—	—

Abbreviated Name	Redshift	$\log(M_*)$	$\log(M_{\text{BH}})$	r_{50} (kpc)	BPT	HeII	neighbors	disturbed	counter-rotating	outflow	stratified
J1307+52	0.0259	9.10	—	1.18	SF	SF	2	—	—	—	—
J1315+22	0.0226	9.20	—	1.58	SF	SF	1	—	—	—	—
J1343+25	0.0280	9.19	—	3.09	SF	SF	3	—	—	—	—
J1401+54	0.0059	9.57	3.2 ^b	0.59	AGN	AGN	5	—	—	—	—
J1402+09	0.0195	8.83	—	0.79	AGN	AGN	26	s	—	—	—
J1405+11	0.0178	9.23	—	1.15	AGN	AGN	4	—	—	—	—
J1407+50	0.0070	8.72	—	0.77	Comp.	AGN	8	—	—	—	—
J1412+10	0.0324	8.99	—	0.56	AGN	AGN	3	x	—	—	—
J1442+20	0.0426	8.89	—	0.89	AGN	AGN	1	x	—	x	x
J1458+11	0.0198	9.91	—	2.40	SF	SF	0	—	—	—	—
J1511+23	0.0143	9.68	—	1.01	SF	SF	0	—	—	—	—
J1546+03	0.0132	9.49	—	2.05	SF	AGN	3	—	—	—	—
J1608+12	0.0166	9.75	—	2.65	SF	SF	0	—	—	—	—
J1623+39	0.0172	9.22	—	2.68	SF	SF	2	x	—	—	—
J1623+45	0.0064	9.41	—	0.82	AGN	AGN	0	x	—	—	—
J1644+43	0.0178	9.53	—	0.86	SF	SF	0	—	—	—	—
J1706+33	0.0301	9.41	—	1.95	SF	SF	7	—	—	—	—
J1717+33	0.0151	9.85	—	1.03	SF	SF	1	x	—	x	—
J1721+28	0.0280	10.0	—	3.49	SF	SF	0	—	—	—	—
J1722+28	0.0281	9.23	—	1.71	SF	SF	3	x	—	—	—
J2320+15	0.0130	9.57	3.7 ^b	0.59	AGN	AGN	6	—	—	—	—

Table 3.2: (1) * indicates objects excluded from this study. (2) Redshift is calculated by fits to stellar absorption lines in LRIS spectra using PPXF. (3) Stellar mass reported in the MPA-JHU catalogue. (4)^b Black hole mass lower limits derived using Eddington Luminosity arguments (M14)^c Black hole mass estimated using $M_{\text{BH}} \propto R\Delta V^2/G$, where ΔV is measured from broad H α , extrapolating the BLR radius – luminosity relation extends into the low mass regime (R13) (5) SDSS Petrosian radius containing 50% of r-band flux, in kiloparsecs. (6) Classification of dominant ionization source based on Gaussian fits to emission lines using the process described in Section 3.3.2. The spectra were extracted from the central 1kpc of each galaxy. (7) Same as (6) but for HeII classification (S15) (8) Number of galaxies with comparable mass within 1.5 Mpc. (9) Classified as disturbed (see Section 3.4.2) (10) Gas is clearly rotating and offset from stellar component. (11) Has an outflow identified by an additional broad component in as defined in Paper I. (12) Narrow emission lines are stratified (see Section 3.4.2)

name	$\log(M_*)$	AGN	counter-rotating	outflow (Paper I)	u-r colour
J0802+20	10.6	x	x		2.39
J0932+31	9.6	x	x		2.23
J0954+47	9.5	x		x	2.20
J1005+12	9.6	x		x	2.16
J1009+26	8.7	x		x	1.91
J1014+19	8.6			x	1.25
J1623+45	9.4	x			2.13

Table 3.3: Seven galaxies in our sample have disturbed gas kinematics and no neighbors of comparable mass within 1.5 Mpc and $\pm 1000 \text{ km s}^{-1}$. Six of them host AGN, two have counter-rotating gas, and four have outflows indicated by broad wings in their [OIII]5007 emission line profiles. $u - r$ colour is based on SDSS cModelMag photometry.

decomposed into stellar, Balmer emission, and forbidden emission components. In order to investigate the potential effects of AGN on gas kinematics in this sample, we quantified velocity offsets between stellar and gas components. We summarize our conclusions below.

1. We detect counter-rotating gas in five of 45 galaxies, and AGN are present in all five cases. A study of the occurrence, properties, and evolutionary history of counter-rotating galaxies in Illustris [298] finds that removal and re-accretion of gas is necessary for counter-rotating gas discs to form, and that periods of AGN activity are sometimes associated with large drops in gas mass. We find that the properties of the counter-rotating dwarfs in our sample agree with present-day properties of counter-rotating dwarf galaxies predicted from Illustris.
2. We use the weighted average of velocity offsets between stellar spectra and emission lines to identify disturbed gas kinematics. We find disturbed gas in 25 out of 45 galaxies in our sample. Of the 26 AGN in our sample, 19 (or 73%) have disturbed

gas. Star forming galaxies tend to have orderly, co-rotating gas discs, with only 32% showing disturbed gas.

3. At least three galaxies in our sample have line of sight velocities far exceeding those expected based on their stellar masses. These line of sight velocities constitute a lower limit estimate of true halo mass, indicating that these galaxies inhabit much more massive dark matter haloes than expected based on their small stellar masses. This potential evidence of ongoing star formation suppression is most apparent in three AGN-hosting galaxies within our sample, two of which have counter-rotating gas. This suggests that AGN could be associated with gas removal and star formation suppression in dwarf galaxies. A detailed study of the star formation histories of these galaxies is warranted.
4. In the absence of environmental influence, kinematically disturbed gas is expected to be caused by secular processes. Fifteen dwarfs in our sample are isolated, with no neighboring galaxies of comparable mass within 1.5 Mpc and $\pm 1000 \text{ km s}^{-1}$. Of these, seven galaxies have disturbed gas. We find that six out of seven isolated galaxies with disturbed gas host AGN.

Our findings imply that AGN play an important, and perhaps dominant, role in disturbing gas and limiting star formation in dwarf galaxies. This represents additional evidence of the importance of AGN-driven winds in dwarf galaxy evolution and further highlights the importance of including AGN feedback in galaxy formation models. A detailed follow-up IFU study of ionized gas kinematics in a subset of these galaxies is in progress (Liu et. al., in prep). Multiphase gas kinematic measurements, gas mass measurements,

and comparison with simulations run with detailed AGN feedback models are necessary for a full understanding of AGN feedback in dwarf galaxies.

Acknowledgements We would like to thank the anonymous referee, whose careful reading and thoughtful feedback has helped to improve and clarify this manuscript. Support for this program was provided by the National Science Foundation, under grant number AST 1817233. Additional support was provided by NASA through a grant from the Space Telescope Science Institute (Program AR- 14582.001-A), which is operated by the Association of Universities for Research in Astronomy, Incorporated, under NASA contract NAS5-26555. The data presented herein were obtained at the W. M. Keck Observatory, which is operated as a scientific partnership among the California Institute of Technology, the University of California and the National Aeronautics and Space Administration. The Observatory was made possible by the generous financial support of the W. M. Keck Foundation. The authors wish to recognize and acknowledge the very significant cultural role and reverence that the summit of Mauna Kea has always had within the Indigenous Hawaiian community. We are most fortunate to have the opportunity to conduct observations from this mountain. Some of the data presented herein were obtained using the UCI Remote Observing Facility, made possible by a generous gift from John and Ruth Ann Evans. This research has made use of the NASA/IPAC Extragalactic Database (NED), which is operated by the Jet Propulsion Laboratory, California Institute of Technology, under contract with the National Aeronautics and Space Administration.

Chapter 4

AGN Impact on Dwarf Galaxy

Stellar Populations

4.1 Introduction

One of the fundamental aims in the study of galaxy evolution is to understand the mechanisms that govern star formation activity. Cold gas collapses inside of molecular clouds to form stars, which then produce and inject metals into the interstellar medium (ISM). These metals form dust and enrich the the next generation of stars as well as the gas in and around the galaxy.

Historically, dwarf galaxies have been classified according to their morphologies, which is related to their star formation activity [148]: dwarf spheroidal systems have no gas or ongoing star formation, dwarf irregular systems have high star formation rates, and ‘transition’ galaxies exhibit recent star formation but host no massive stars [310]. These

categorizations can be useful when examining galaxy morphology but provide little physical insight into the galaxy’s evolutionary history.

Assuming the spectral features of a galaxy contain imprints of the galaxy’s evolution, the decomposition of these features could be used to trace that evolution over time [332], [77]. A galaxy’s star formation history (SFH) describes the mass-weighted record of stellar formation times, thus providing a comprehensive view of the assembly history of the galaxy. It reveals information about stellar populations that would be difficult to interpret solely based on average values. For example, does the presence of young stars among a more mature population signal a recent rejuvenation of star formation, or are they the final generation to form before star formation shuts down?

Star formation histories of low mass galaxies have already revealed a wealth of information about galaxy formation on small scales. For instance, ultrafaint dwarfs have universally old populations and stunted growth for most of their lives, which supports the notion that they were quenched by reionization (e.g. [48]). By contrast, the SFHs of more massive dwarf galaxies appear to depend on environment. All but the most massive satellites of the Milky Way and M31 have ceased star formation, yet isolated dwarfs are nearly always star forming [122], [115]. Yet, the existence of quenched, isolated dwarf galaxies [154] and the lack of dependence of satellite star formation shut-off times and distance to the host [347] indicate that the processes regulating star formation in dwarfs are still not fully understood. Perhaps AGN activity can account for some of the observed diversity in dwarf galaxy SFHs.

The same spectral fitting methods used to probe star formation histories can also produce chemical evolution histories. Each star retains the metal content of the gas at the

time of its formation, so absorption features from metals in stellar atmospheres reveal the average metal-to-hydrogen ratio of the ISM at the time of formation, providing insight into the early epochs of chemical enrichment. Stellar metallicity has been found to correlate with mass, with high mass galaxies exhibiting higher metal content than low mass galaxies [116], [229]. This scaling relation could place important constraints on galaxy formation and chemical evolution models, but the physical processes governing growth and chemical evolution are still an active area of study. It is thought that low mass galaxies may efficiently remove metal enriched gas from their shallow potential wells, preventing the accumulation of metals in their gas reservoirs. Alternatively, metal-poor gas inflows may dilute existing metals, decreasing the metal-to-hydrogen ratio in the stars born from this gas [84], [86]. Yet another possibility is that star formation efficiency is mass dependant, and that higher mass galaxies are more efficient at converting their gas into stars, boosting metal abundance [45], [51].

So far, this project has focused on the movement of gas within dwarf galaxies, drawing the conclusion that AGN play a significant role in driving winds. Ultimately, we are interested in understanding whether AGN feedback can explain inefficient star formation in dwarfs. In this chapter, I study the stellar properties of our sample and investigate the relationship between AGN and the many observable properties of the stars in their host galaxies.

4.2 Data and Analysis

In this chapter, we further analyze the sample introduced in Chapters 2 and 3. The longslit data for 50 dwarf galaxies were collected from the Low Resolution Imaging Spectrometer (LRIS) on Keck I, and were reduced using standard IRAF tasks. For a discussion of sample selection and data reduction, see Section 2 of Chapter 2. For details about the observations, please consult Section 2 of Chapter 3. An example of a fully reduced 2D spectrum is shown in the top panels of Figure 4.1. Each pixel row is a fully reduced 1D spectrum, and customized extractions along the slit are obtained by summing pixel rows. The cyan highlights in the top panels of Figure 4.1 indicate the regions integrated to produce the spectra shown in the middle panels. In this chapter, I refer to the integrated properties of dwarf galaxies, meaning the entire profile of the galaxy is integrated as a single spectrum and fit using the following method.

4.2.1 Star Formation History

I used the Penalized Pixel Fitting software (PPXF) [59] to fit a linear combination of single-stellar population (SSP) model spectra from the Miles Library of Stellar Spectra ([271]; [106]). A total of 144 spectra form a rectangular grid that spans the age range of 0.06 – 12.6 Gyr and metallicity $[Z/H] = -1.71 - 0.2$, which are then fit to our LRIS spectra using a maximum penalized likelihood approach.

The age-metallicity parameter space is constructed by decomposing each parameter into single bursts of star formation. Each SF burst produces a single stellar population, born at the same time from the same gas with the same metal abundance. A Salpeter initial

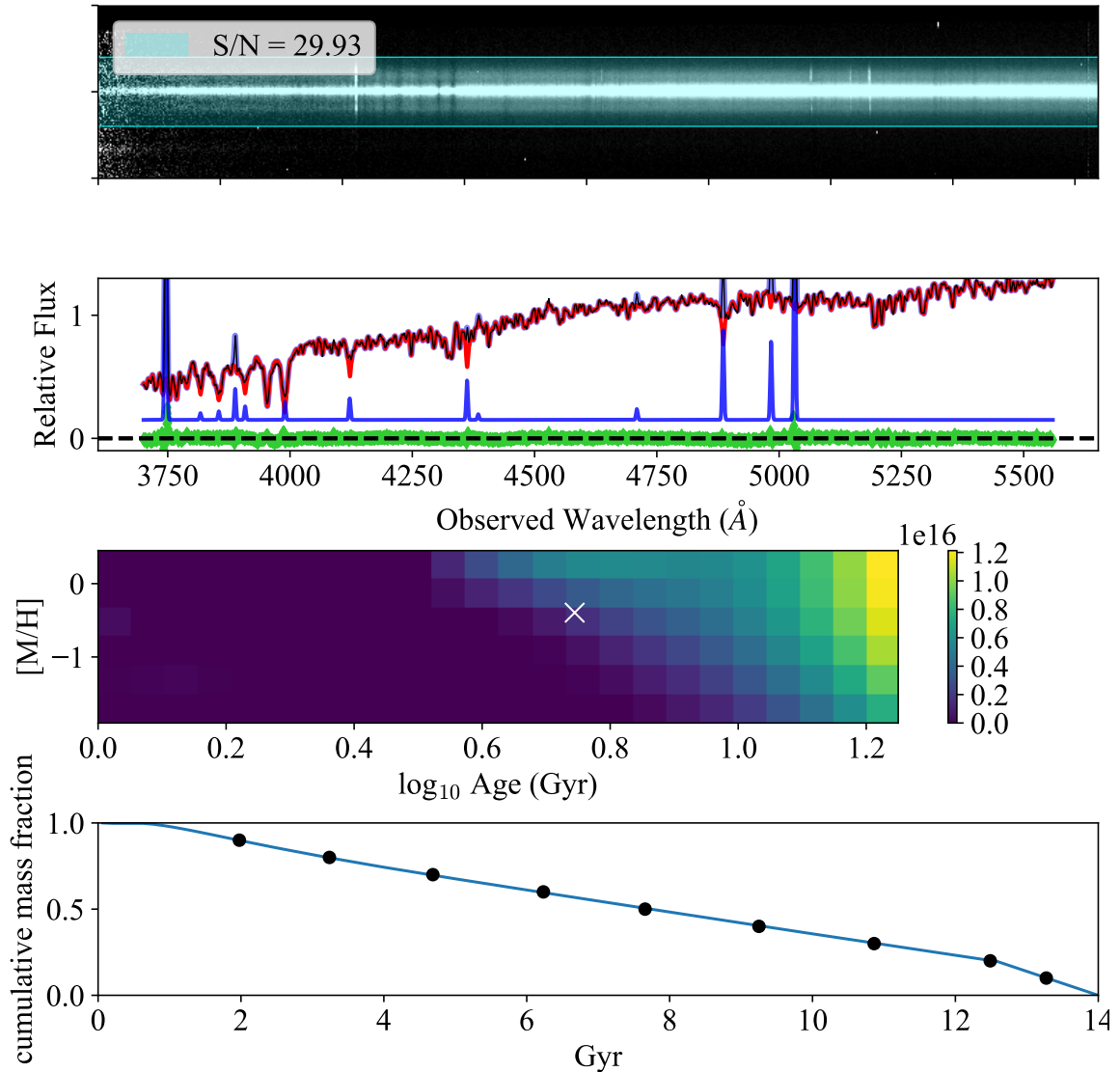


Figure 4.1: The PPXF fit to the integrated spectrum of a galaxy is shown. The fully reduced 2D spectrum is shown in the top panel, with the integrated region highlighted in cyan. The middle panel displays the spectra integrated within the highlighted cyan region (black), superimposed with the best fit stellar (red) and gas (blue) model. Fit residuals are plotted in green. The third panel shows the PPXF solution for across stellar age and metallicity intervals. The regularized map shows the mass fraction of stars falling within each interval, with higher mass fractions in yellow. The bottom panel plots the stellar mass fraction over time, which traces the assembly history of the galaxy.

mass function (IMF) is assumed when building the library of synthesized SSP spectra, each of which represents a stellar population with a single specified mass, age, and metal abundance. The SSP template spectra are then combined to reproduce the shape and absorption features in the observed spectra by assigning weights to each template. If each SSP is born from a SF burst of equal mass, the weights will represent the mass fraction of each population.

Inferring the SFH from integrated galaxy light is an ill-posed problem that can result in degeneracies. This can be addressed via linear regularization, using the ‘REGUL’ parameter in PPF. This parameter imposes a smoothness constraint on the solution, defining the weights assigned to each model spectrum in the age-metallicity grid, and ensuring that the weights of adjacent models in the grid vary smoothly. The grid contains one SSP model spectrum per unit mass, meaning the fitted weights represent relative mass contributions of each population. When integrated along the metallicity axis, the relative mass to light ratios for each population reveal the stellar mass contribution as a function of age, or the stellar mass assembly history of the galaxy.

The integrated spectrum of each galaxy was fit using the SSP model grid described above, along with an order 2 multiplicative polynomial to account for the AGN continuum and Gaussian templates for all strong Ne, O, and H emission lines in the rest wavelength range 3700 – 5560. Hydrogen Balmer emission lines were modeled as a single template, enabling a simultaneous fit for dust reddening using the ‘gas_reddening’ parameter, which assumes a Calzetti extinction curve [52].

The results of this non-parametric approach should be interpreted with care, as the results depend on the stellar template libraries chosen and the propagation of other variables included in the fit (e.g. [126],[68]). For this reason, I reduce the number of free parameters in the fit by performing a preliminary fit to each spectrum to determine the stellar kinematics. I then perform a second fit with stellar kinematics fixed in order to extract the SFH. Another limitation to this method is that it relies on the assumption that the SSP templates are eigenvectors, when in reality, they are not. However, this limitation is unavoidable in all existing techniques for estimating SFH.

4.2.2 Mass Weighted Stellar Ages and Abundances

The mass weighted age and metallicity are derived from the SFHs discussed in the previous section, and are given by Equations 1 and 2 in [203]:

$$\log(\text{Age}_{\text{SFH}}) = \frac{\sum w_i \log(t_{\text{SSP},i})}{\sum w_i} \quad (4.1)$$

$$[Z/H]_{\text{SFH}} = \frac{\sum w_i [Z/H]_{\text{SSP},i}}{\sum w_i} \quad (4.2)$$

where w_i are the weights of the i th template of age t_{SSP} and metallicity $[Z/H]_{\text{SSP},i}$. By analyzing PPF fits to mock spectra, [121] find that the bias and scatter (P) in these mass-weighted quantities depend heavily on the signal to noise (SN) of the spectrum

$$P = \frac{k_p}{\text{SN}} \quad (4.3)$$

where k_p at various SSP ages can be found in Table 1 of [121]. This value was added in quadrature with the fit errors when reporting uncertainties in mass weighted average quantities.

4.3 Results and Discussion

In previous chapters, SDSS photometry provided rough approximations of the star formation activity in this sample of dwarf galaxies. We found some intriguing associations between AGN-driven gas disturbances and red galaxy colors, which is suggestive of AGN-induced star formation suppression in some galaxies in our sample. In this section, I present a more robust analysis of the stellar populations in isolated galaxies with AGN, galaxies with counter-rotating gas, and galaxies with outflows.

The results of this analysis is summarized in Figure 4.2. The top row of Figure 4.2 shows star formation histories of three groups of galaxies which are potentially affected by AGN feedback. Cumulative mass fractions trace the stellar mass assembly of each galaxy over time, providing insight into the mechanisms driving their evolution.

A simple way to approach the analysis of global stellar properties is to classify galaxies as ‘blue and active’ or ‘red and passive’ based on a dividing line in $(U - B)_{AB}$ colors [237]. This approach is simplistic, but it enables the comparison between the galaxies in this sample to the active and passive mass-metallicity relations for local galaxies shown in the bottom row of Figure 4.2 [236]. The divergence of the passive (red) and star forming (blue) relations in galaxies below $M_\star \sim 10^{11} M_\odot$ supports the notion that low mass galaxies often quench by a process known as strangulation. In this scenario, the quenching mechanism

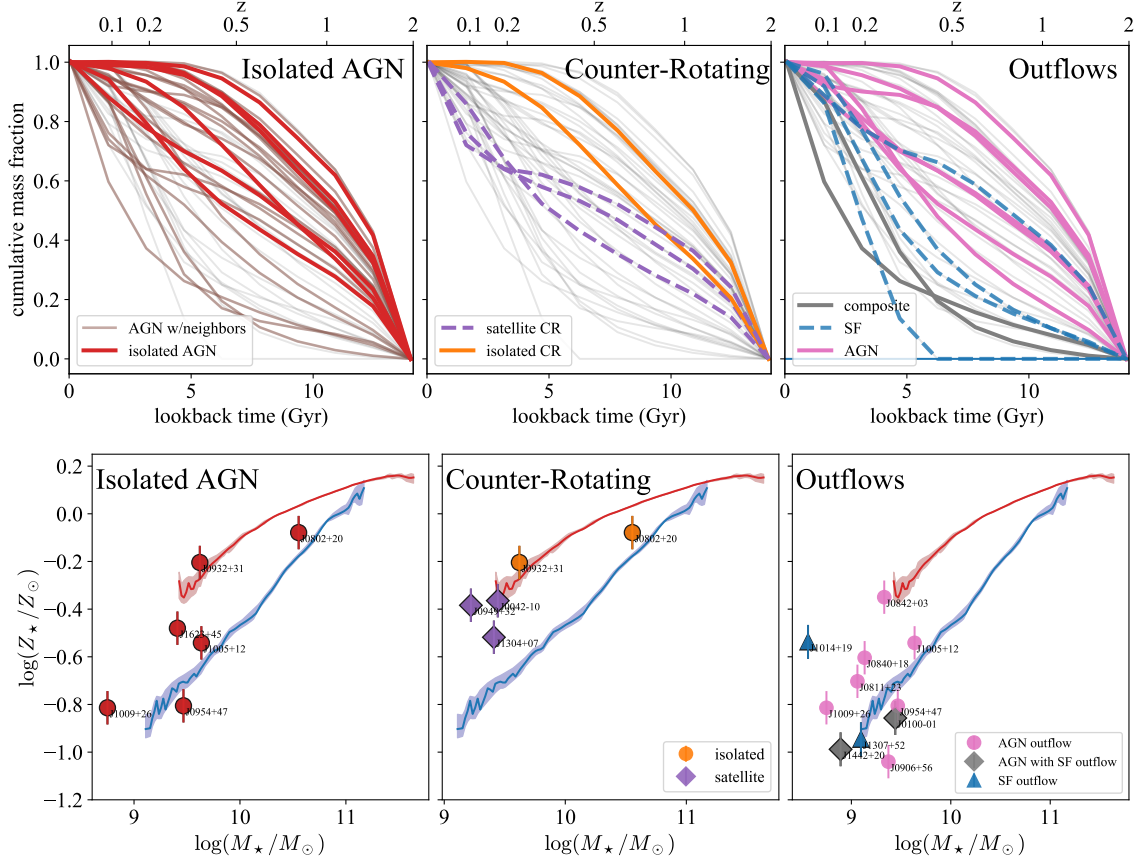


Figure 4.2: Top: The stellar mass growth is traced by the cumulative stellar mass fraction over time. SFHs of all galaxies in the sample are shown as faint gray lines and various groups of interest are highlighted in each panel. Top left: The red lines represent the SFHs of six isolated galaxies with AGN. The AGN galaxies with neighbors are indicated by brown lines and the SFHs for the star forming control sample are shown as faint gray lines. Top middle: The five galaxies in our sample with counter-rotating gas are emphasized. SFHs of counter-rotating galaxies that are satellites of massive ($M_* > 10^{11} M_\odot$) galaxies are shown as purple dotted lines, while isolated counter-rotating galaxy SFHs are plotted in solid orange. Top right: Galaxies with outflows detected via broadened [O III] components are emphasized. SFHs for galaxies with AGN-driven (pink), star formation-driven (blue), and AGN hosting galaxies with star formation-driven outflows (composite; gray) are shown. Bottom: The stellar mass - metallicity relation for active (blue) and passive (red) galaxies is plotted [236]. In each bottom panel, the integrated stellar metal abundances of the galaxies shown in the corresponding top panel are plotted according to the same color schemes.

removes some gas from the galaxy while preventing accretion of new gas. The remaining gas is left to form stars, which depletes the gas reservoir while building up the stellar metal abundance.

4.3.1 Are AGN suppressing star formation in isolated galaxies?

Without the effects of interactions with neighboring galaxies, star formation histories are expected to be governed by secular processes. In Chapter 3, we found that isolated galaxies without AGN tend to have orderly gas disks that co-rotate with their stars, while all six isolated galaxies with AGN have disturbed gas kinematics and redder colors.

In this work, SSP fits reveal that the stellar populations in isolated AGN hosts are on average 1.8 Gyr older than the rest of the AGN in the sample. The top left panel of Figure 4.2 shows the star formation histories of the six isolated AGN (red) compared to AGN host galaxies with neighbors (brown). While AGN in more crowded environments display a wide variety of star formation histories, these six isolated galaxies either grow gradually over time or formed 90% of their stars by $z = 0.5$.

All six isolated galaxies have $(U - B)_{AB}$ colors that place them in the ‘red passive’ category, according to the simplistic color criteria used to differentiate between active and passive mass-metallicity relations in Figure 4.2 [237]. Since our sample selection depends on emission lines, all of the galaxies discussed in this work have detectable ionized gas and thus cannot be considered completely quenched. However, three of these galaxies (J095418.16+471725.1, J100551.19+125740.6 , J100935.66+265648.9; solid red lines) are shedding their gas via AGN-driven outflows, as described in Chapter 2. The rest (J080228.83+203050.2, J093251.11+314145.0, J162335.06+454443.6; dashed red lines) show

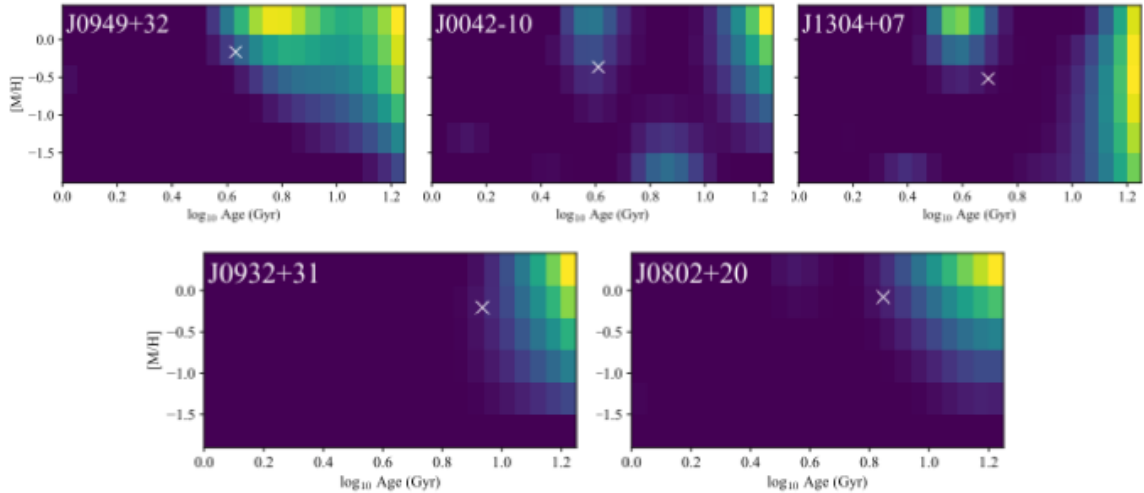


Figure 4.3: The full mass weighted stellar age - stellar metallicity grids for all five counter-rotating galaxies are shown, in order of increasing mass. The three galaxies in the top row are satellites and the two in the bottom are isolated. Each block in the grid is associated with a SSP with the specified stellar age and metallicity. The color scheme represents the mass fraction associated with each SSP, where yellow indicates the largest fraction.

signs of suppressed star formation: they all have formed 90% of their stellar mass by $z \sim 0.2$ and have small $H\alpha$ equivalent widths ($WH\alpha < 6\text{\AA}$). Furthermore, J093251.11+314145.0 has a lower stellar mass than expected based on its rotational velocity, indicating that the star formation within its massive dark matter halo was suppressed (see Chapter 3, Section 3.4.3).

In short, all of the isolated AGN hosts in this sample appear to be passive and gas depleted, or are actively ejecting gas.

4.3.2 The story behind counter-rotation

In order to form a counter-rotating gas disk, it is thought that a galaxy must first clear its existing co-rotating gas. The mechanism for removing co-rotating gas is not fully understood, but a study of low mass counter-rotating gas in Illustris suggests that large

scale outflows or ram pressure stripping from a central galaxy are likely culprits [298]. In Chapter 3, we identified five galaxies with counter-rotating gas. Not only were they much more common than expected, but all of them host AGN. This evidence associates AGN with gas-star counter-rotation, suggesting that AGN may be responsible for clearing these galaxies of their gas. In this section, I examine the average stellar properties and star formation histories of these five galaxies for clues as to how their counter-rotating gas disks came to be.

Since ram pressure stripping by central galaxies is a likely gas removal mechanism, it makes sense to consider galaxy environment when analyzing the SFHs of these five galaxies. Two of the counter-rotating galaxies are isolated and the other three live in rather busy environments. In this section, I refer to these three galaxies as satellites because they are all within 0.6 Mpc of a galaxy with mass $M_{\star} > 10^{11} M_{\odot}$.

The SFHs for the satellite and isolated galaxies with counter-rotating gas are shown in the top middle panel of Figure 4.2. The sample is very small, but there is a clear distinction between the SFHs of the isolated and satellite galaxies. The isolated galaxies grew quickly before $z = 0.5$ and have very little recent star formation, having essentially reached their present day mass by $z = 0.2$. On the other hand, the satellites appear to experience a late burst of star formation, obtaining roughly 40% of their mass after $z = 0.2$. This burst sometimes occurs after a period of relatively slow growth. The five counter-rotating galaxies also have consistently high stellar metal abundances relative to the rest of the AGN in the sample.

With only five galaxies, it is difficult to pinpoint a single process responsible for clearing gas to make way for counter-rotating gas. The presence of AGN in all instances of counter-rotating gas is conspicuous, but a larger sample is needed to fully understand the role of AGN in this narrative. The metal rich stellar populations of these counter-rotating galaxies could indicate that the gas removal mechanism at work has also prevented the infall of new gas for a large portion of these galaxies' lifetimes, stunting their growth through strangulation.

It is unclear from the mass weighted average stellar abundance how these galaxies accumulated their metals. The chemical evolution of these galaxies can best be understood by examining the full age-metal grids of each galaxy, shown in order of increasing mass in Figure 4.3. The three galaxies on top are satellites and the two on the bottom are isolated. The satellite galaxies appear to grow the first 20–40% of their mass in a starburst fueled by gas of varying metallicity. J004214.99-104415.0 and J130434.92+075505.0 then experience a period of little to no growth. Then, they have a late burst of star formation, presumably associated with the recently accreted counter-rotating gas. It is interesting to note that the most recent bursts of SF form from enriched gas. On the other hand, isolated counter-rotating galaxies show no signs of recent star formation bursts associated with their accreted gas.

These different evolutionary tracks are difficult to explain solely with the measurements presented here, but one could hypothesize that the source of counter-rotating gas differs with environment. Perhaps the counter-rotating disks in the satellite galaxies are the results of minor mergers with gas rich, star forming dwarfs. It could be that the

young stars observed in the satellite galaxies are formed ex-situ and then accreted along with the gas, rather than formed as a result of cold gas accretion. Meanwhile, the isolated galaxies may have obtained a small amount of non-star forming gas through less dramatic accretion events. Further investigation into this thought could be conducted by decomposing the stellar kinematics by age and searching for a counter-rotating disk of young stars alongside the gas.

4.3.3 Stellar Activity and Outflows

In Chapter 2, we found that the $u - r$ colors of the 13 galaxies with outflows agree qualitatively with a scenario where AGN-driven outflows mark a transition from blue and star forming to red and quiescent, as is postulated at higher masses ([270], [218], [167], [96], [305], [312]). Here, I investigate whether a more detailed analysis of their SFHs will tell the same story.

In the top right panel of Figure 4.2, we see that galaxies with AGN-driven outflows (pink) have a variety of SFHs, but in general, they have earlier formation times and are growing more slowly at $z = 0$ compared to the other galaxies in the outflow sample. By contrast, star forming galaxies with outflows (blue) assemble later on average than the rest of the sample. The two composite galaxies (gray), which host AGN but have outflows that are likely driven by star formation, are among the fastest growing galaxies in the sample.

In Chapter 2 we speculated that the emission line profiles could hold clues as to the placement of the source in the galaxy, where blueshifted wings are associated with centrally located outflow sources while outflow sources scattered throughout the galaxy would produce symmetrical line profiles (See Chapter 2, Section 5.2 for a more detailed

discussion). The outflows in the composite galaxies are thought to be powered by star formation based on the symmetry of their emission line profiles.

The SFHs measured here support the narrative implied by the $u - r$ photometry. The seven galaxies with intermediate colors tend to have older stellar populations and earlier formation times, while the six bluest galaxies have more recent star formation bursts. This further supports the scenario where star formation driven outflows are found in actively star forming galaxies, while AGN-driven outflows are associated with a galaxy's transition from the blue cloud to the red sequence. The confirmation of rapid stellar mass growth in the composite galaxies further supports the conclusion that their outflows are driven by stellar processes, and lends credence to the idea that the positions of outflow sources can be inferred from their emission line profiles.

4.4 Summary

In this chapter, I used mass-weighted SSP fits to recover star formation and chemical evolution histories for 50 dwarf galaxies. I investigated the integrated properties of various subgroups of the sample to further understand the role that AGN play in governing star formation in dwarf galaxies. My results can be summarized as follows:

1. All isolated galaxies with AGN have colors consistent with passive evolution [237] and either show signs of gas depletion [69] or are in the process of losing their gas[195]. By contrast, isolated galaxies without AGN are all actively star forming, indicating that when only secular processes are involved, AGN are strongly associated with star formation suppression.

2. Though AGN appear to play a role in removing gas to make way for counter-rotating disks, environment appears to play a role in the re-accretion of new material. Isolated counter-rotating galaxies grow gradually from high metallicity gas, forming 80% of their stellar mass before $z = 0.5$. Satellite counter-rotating galaxies form from gas with varying levels of metal enrichment and then grow slowly before experiencing an apparent burst of star formation fueled by high metallicity gas. Isolated galaxies with counter-rotating gas do not have a new burst of star formation associated with new gas accretion. This implies that counter-rotation in isolated galaxies results from accretion of small amounts of non-star forming gas, while counter-rotating gas in satellites may originate from mergers with gas rich, star forming dwarfs.

3. Galaxies with AGN-driven outflows have diverse star formation histories, but have consistently older stellar populations and slower present-day stellar mass growth than those with star formation-driven outflows. In this chapter, I confirm that the composite galaxies, which host AGN yet have outflows likely associated with stellar processes, are indeed undergoing a current burst of star formation. This supports the idea that emission line profiles may be used in conjunction with flux ratio diagnostics to distinguish between AGN and SF driven outflows.

In this chapter, the mass-weighted stellar properties were used to further probe the effects of AGN on the growth of dwarf galaxies. Luminosity-weighted stellar properties are more sensitive to the contributions of younger stellar populations, and could be used to investigate the dominant radiative processes at work in these galaxies. Careful decompositon

of stellar spectra to obtain distinct rotation curves for various populations of stars could also lend insight into the merger histories in the counter-rotating dwarfs.

This analysis could also be extended by examining the evolution of individual elements to explore the processes that enrich the ISM. A spatially resolved study of the gas phase metal abundances would also reveal the present day metal content and transport in these dwarfs.

name	$\log(M_*/M_\odot)$	age (Gyr)	$t_{50}(Gyr)$	$\log(Z_*/Z_\odot)$
J0021+00	9.146986	7.551983	10.520711	-0.589740
J0042-10	9.442602	3.937794	7.683454	-0.364481
J0100-01	9.441348	2.064401	3.268963	-0.856955
J0156-00	9.390523	3.411646	3.292840	-0.638414
J0246-00	9.348598	8.198474	10.681655	-0.366976
J0300+00	8.723645	5.818258	3.837403	-0.626042
NGC 1569	8.560000	3.435674	12.589300	-1.434657
J0755+24	8.851282	3.384052	4.634967	-1.177595
J0802+10	9.600313	8.641875	10.204633	-0.306619
J0802+20	10.553940	6.903988	8.945402	-0.078855
J0811+23	9.060884	7.623616	10.785976	-0.702861
J0812+54	9.285977	5.847416	4.283185	-1.188364
J0840+18	9.133316	8.338386	10.911056	-0.603908
J0842+03	9.330553	4.918787	6.084814	-0.349859
J0851+39	9.277671	1.509083	2.004934	-0.061930
J0906+56	9.372400	5.780641	5.042306	-1.039935
J0911+61	8.946604	1.148056	1.293918	-0.935850
J0921+23	9.268008	4.605948	4.533198	-0.625387
J0932+31	9.620956	8.875524	10.483105	-0.204271
J0948+09	8.730108	9.094378	9.437261	-0.981134
J0949+32	9.220258	6.758339	7.614780	-0.383914
J0954+47	9.466668	9.637536	10.327185	-0.805574
J1002+59	9.600677	7.265508	9.952643	-0.356012
J1005+12	9.635745	5.558454	8.711172	-0.541482
J1009+26	8.749137	5.128555	4.541501	-0.813839
J1014+19	8.563872	4.136424	3.777498	-0.537318
J1143+55	8.924566	3.488165	3.014142	-0.840875
J1223+58	9.392751	9.961965	12.250991	-0.561278
J1304+07	9.410233	4.070558	9.777599	-0.518040
J1307+52	9.096391	3.507890	2.929054	-0.945953
J1315+22	9.197057	5.576337	10.359664	-0.368915
J1343+25	9.185787	9.593189	11.428664	-0.941250
J1401+54	9.567201	8.956039	10.771114	-0.178446
J1402+09	8.832737	7.089637	10.061051	-0.839742
J1405+11	9.226830	4.997284	7.151002	-0.627191
J1407+50	8.721412	8.298145	9.672636	-0.730818
J1412+10	8.992185	3.002057	4.201882	-0.003611
J1442+20	8.891579	2.786269	3.818201	-0.988093
J1458+11	9.908138	6.723958	10.005804	-0.404059
J1511+23	9.684150	4.649176	8.821941	-0.748695
J1546+03	9.487150	3.050479	2.193108	-0.476559

name	$\log(M_*/M_\odot)$	age (Gyr)	$t_{50}(Gyr)$	$\log(Z_*/Z_\odot)$
J1608+12	9.753928	5.432191	9.280954	-0.762544
J1623+39	9.218903	6.269718	9.995369	-1.075628
J1623+45	9.409533	8.847325	10.927397	-0.480009
J1644+43	9.528967	2.862352	3.227272	-0.959610
J1706+33	9.408504	5.647809	8.791064	-0.989041
J1717+33	9.847754	5.120873	6.050567	-1.346557
J1721+28	10.033380	2.596349	2.150411	-0.307855
J1722+28	9.245996	4.494351	5.481613	-0.763320
J2320+15	9.574848	9.024725	10.878865	-0.194280

Table 4.1: The average integrated mass-weighted stellar age, metal abundance, and formation times for all 50 galaxies.

Chapter 5

Summary and Conclusions

It is thought that AGN feedback is the primary mechanism limiting the growth of massive galaxies, while stellar feedback is often invoked to explain star formation suppression in dwarf galaxies. The general conclusion of this work is that AGN activity often has dramatic effects on the gas kinematics of dwarf galaxies, possibly regulating their star formation histories. AGN appear to be important, if not dominant, sources of feedback in the low mass regime and therefore should not be overlooked when investigating dwarf galaxy evolution. Finer points are discussed below:

5.1 AGN are able to expel gas from dwarf galaxies

Broadened wings in the emission line profiles of ionized gas reveal the complex kinematics of a galaxy's gas. In Chapter 1, we decomposed strong emission line profiles in order to better understand the motion of ionized gas in galaxies with and without signs of AGN. Thirteen out of 50 galaxies contained spatially extended broadened components,

tracing a portion of gas moving at higher velocities than the rest of the gas in the galaxy. By fitting multiple Gaussian components to spatially resolved emission lines, we found that all 13 galaxies showed gas velocities sufficient to escape their dark matter halos.

Of these 13 galaxies with outflowing gas, we identified six galaxies with broadened emission line ratios consistent with ionization from AGN. The emission line profiles of these six galaxies differed from the rest in that their broadened wings were blueshifted near the galactic centers, while the rest had symmetrical emission line profiles. We surmised that attenuation from dust would obscure emission from redshifted material escaping from a centrally located source, resulting in emission line profiles with blueshifted wings. On the other hand, outflow sources scattered throughout the galaxy are less affected by dust attenuation and thus yield symmetrical line profiles.

This work presented the first direct kinematic measurement of AGN-driven outflows in the low mass regime, and demonstrated that AGN can drive winds capable of escaping dwarf galaxy dark matter halos.

5.2 AGN can affect global gas kinematics

In Chapter 2, we find a strong association between AGN and disturbed gas. In the absence of neighboring galaxies, gas disturbances are expected to be caused by secular processes. We compare the velocities of the gaseous and stellar component in each galaxy and find that all isolated galaxies with AGN have disturbed gas kinematics. By contrast, isolated galaxies without AGN tend to have orderly gaseous disks that co-rotate with the stellar component.

We also find gas in counter-rotation with the stars in five galaxies in our sample, all of which host AGN. In order for counter-rotation to occur, it is thought that a galaxy first must shed its original gas, either by large outflow events or by ram pressure stripping, and then accrete new gas with different angular momentum from the stars. The strong association between AGN and counter-rotating gas suggests that AGN are the dominant mechanism for gas removal.

5.3 AGN with disturbed gas are associated with star formation suppression

The early work in this project found evidence suggestive of AGN- induced star formation suppression in dwarf galaxies. All six galaxies with AGN-driven outflows have intermediate colors that strike between the blue cloud and the red sequence on the color-mass diagram. This is consistent with a scenario where AGN activity marks a galaxy's transition from blue and star forming to red and passive. Similarly, galaxies with counter-rotating gas tend to have redder colors than the rest of the sample, which is expected if the dwarfs lost their entire gas reservoir before accreting new gas. Furthermore, three galaxies in our sample, all hosting AGN, have maximum rotation velocities indicating they inhabit much more massive dark matter halos than expected from their stellar masses.

These results warrant a detailed investigation into the stellar properties of the dwarf galaxy sample. In Chapter 3, I used SSP modeling to retrieve star formation histories for each galaxy in the sample, to investigate the potential effects of AGN feedback on stellar populations. I found that all isolated galaxies with AGN have mass-weighted stellar ages

of 5Gyr or more, and are either passive and gas depleted or have outflows and thus are in the process of losing their gas.

I also found that galaxies with AGN-driven outflows have diverse star formation histories, but have consistently older stellar populations than those with star formation-driven outflows. Of the galaxies with outflows, two host AGN, yet have symmetrical line profiles and broad component flux ratios falling in the composite region of the BPT diagram. These galaxies also happen to have very young (< 3 Gyr) populations and are growing a larger fraction of their stellar masses at present day than any other AGN in the sample. This lends support to the notion that the outflows in these galaxies are driven by star formation.

Isolated counter-rotating galaxies have star formation histories that differ from those with neighbors. The two counter-rotating galaxies residing in isolation have quickly rising cumulative mass fractions, with little to no present day star formation. On the other hand, the three counter-rotating galaxies that reside in rather busy environments show slow growth between $z = 1 - 0.2$ and a recent burst of star formation, presumably associated with the newly accreted gas. I suspect that galaxies in crowded environments obtain counter-rotating gas through minor mergers with gas-rich, star forming dwarfs, while isolated galaxies accrete small amounts non-star forming gas.

There is still much to learn from this collection of Keck-LRIS data. Gas phase metallicities can provide insight on the present day metal enrichment of the ISM and the

transport of metals between these dwarfs and their surroundings. Rotation curves which decompose young and old stellar populations could reveal counter-rotating stellar disks, providing insight into the merger histories of these objects.

A significant fraction of the AGN in our sample contain outflows, so a systematic search for AGN-driven outflows in a much larger parent sample could reveal the extent to which AGN-driven outflows are present in this mass range. Follow-up observations to obtain multiphase gas kinematic measurements, gas mass measurements, and wider IFU coverage of the ionized gas kinematics would deepen our understanding of the processes at play within these dwarfs. Furthermore, it is possible that the disturbed gas is triggering the AGN, rather than the AGN disturbing the gas. It would be interesting to explore this reverse scenario and ask what activated the AGN in the first place. Follow-up HI observations would be useful for investigating this question.

Detailed, spatially resolved kinematic measurements such as the ones presented in this work provide vital observational constraints needed to extend realistic feedback models into the low-mass regime. Considering the expected prevalence of AGN in dwarf galaxies, their strong effect on dwarf galaxy gas kinematics, and their apparent association with star formation suppression, future generations of simulations should account for this important source of feedback.

Appendix A

A.1 Black Hole Masses

Line broadening from the Broad Line Region (BLR) associated with the AGN is sometimes observed in Balmer emission lines (see Figure 2.4) and can be used to measure BH masses. Due to the small spatial extent of the BLR and the low transition probability of forbidden lines, BLR emission does not contribute to the line profiles of [O III] λ 5007, which we use to trace the kinematics of fast-moving winds throughout the galaxy. In this section, we explore the presence of an *additional* BLR component in H α (purple line in the third panel of Fig. 2.4), associated with the BH itself, not to be confused with the broadened components associated with galaxy-scale outflows (orange lines in Fig. 2.4).

We detect a previously unreported broad H α line in J084234.51+031930.7 and measure its virial mass to be $M_{BH} = 6.92 \times 10^5 M_{\odot}$, using RGG13 Equation 5, which relies on the $R_{BLR} - L$ relation of [24].

$$\log(M_{BH}/M_{\odot}) = \log(\epsilon) + 6.57 + 0.47 \log\left(\frac{L_{H\alpha}}{10^{42} \text{ erg s}^{-1}}\right) + 2.06 \log\left(\frac{\text{FWHM}_{H\alpha}}{10^3 \text{ km s}^{-1}}\right) \quad (\text{A.1})$$

Black hole masses for 5 more AGN in this sample are reported in the literature using this approach, yet once outflow components are included in the [N II], H α narrow line model, we find no additional BLR H α components in the other AGN discussed here. We therefore caution that line broadening due to outflowing gas could masquerade as a BLR broad line, so it is necessary to check for outflow contributions in forbidden lines such as [O III] and model them whenever possible when deriving black hole masses from heavily blended complexes such as H α + [N II].

A.2 Spatial Properties of Outflows

Appendix Figure .1 shows the spatial properties of the outflows of the remaining 12 galaxies, as in Fig. 2.7.

A.3 Inclination Correction

PPXF returns line of sight velocities. In order to translate the line of sight velocities measured in PPXF into rotational velocities, the inclination angle must be accounted for. The inclination angle θ_{inc} of a galaxy is defined as the angle between the line of sight and the normal to the disc. A perfectly round disc, inclined by θ_{inc} is projected as an ellipse in an image, with semimajor axis a and semiminor axis b . Assuming an infinitely thin disc, $\theta_{\text{inc}} = \cos^{-1}(b/a)$. More realistically, we can introduce a thickness parameter $q = c/a$, which describes a circular disc of radius a and thickness c , as illustrated in Figure A.2. The

projection of this shape when imaged is still approximately elliptical, and the inclination angle can more accurately be estimated using

$$\cos^{-1}(\theta_{\text{inc}}) = \frac{(b/a)^2 - q^2}{1 - q^2} \quad (\text{A.2})$$

The ellipticity (b/a) was obtained by a fit to the SDSS r -band image using the Python package photutils [42]. In the absence of any constraint on galaxy morphology, we used a range of $q = 0.1 - 0.2$ [125].

It is straightforward to translate line of sight velocity to circular velocity using the inclination angle:

$$v_{\text{rot}} = \frac{v_{\text{los}}}{\sin(\theta_{\text{inc}})} \quad (\text{A.3})$$

The range of inclination angles then translates to a range of possible v_{rot} values. The v_{los} measurements are corrected using the mean value for θ_{inc} . The minimum and maximum values for θ_{inc} are used to estimate the error introduced to the v_{rot} measurements by the uncertainty in inclination.

We forego inclination correction for two cases (J081145.29+232825.7 and J084234.51+031930.7) where the inclination angle is less than 20 degrees. These galaxies are viewed face-on, and show no distinct rotation. Their gas kinematics imply a stratified narrow line region with a non-rotational, possibly spherical outflow (see Section 3.4.2). If this is the case, line of sight velocities are more physically meaningful than rotational velocities.

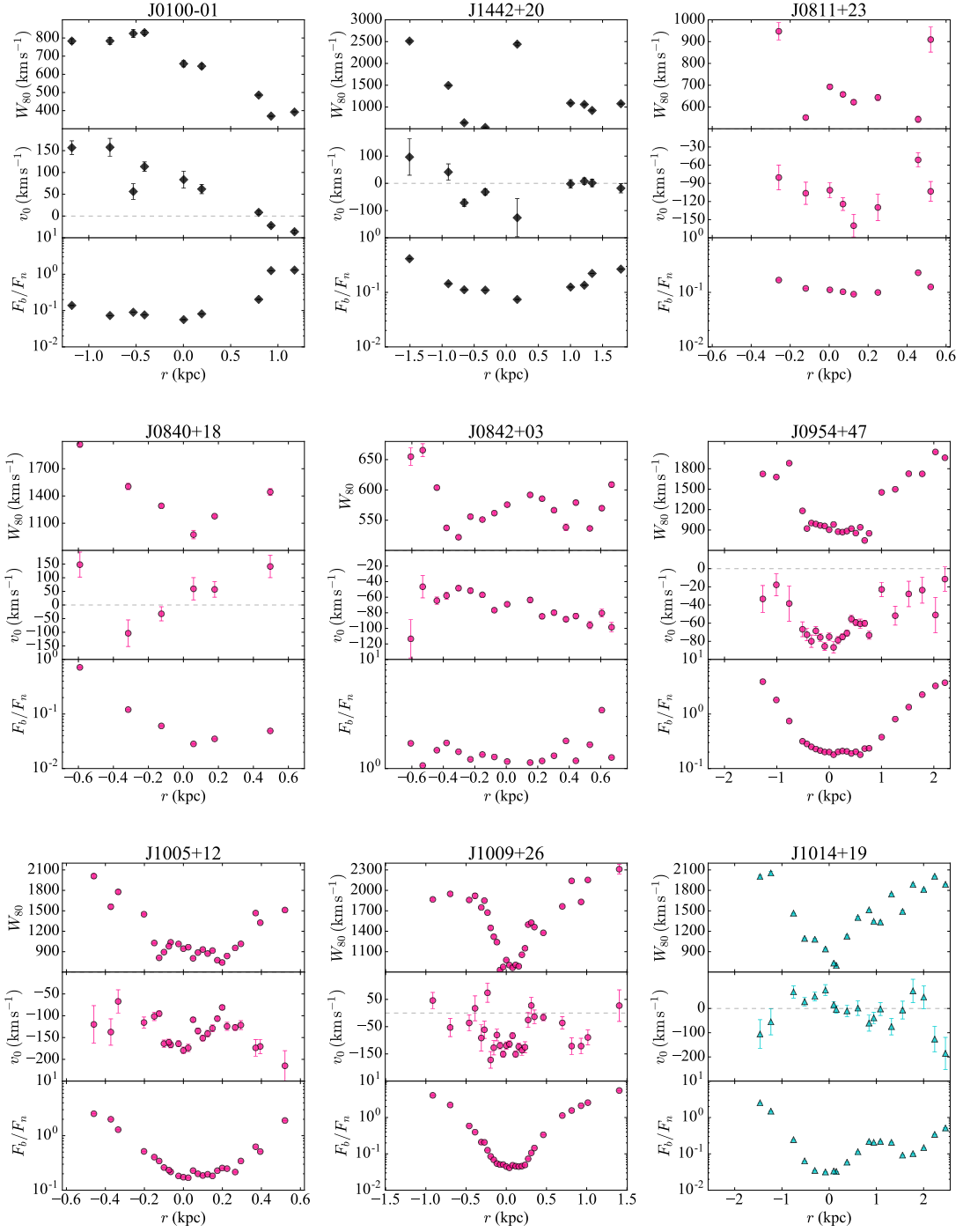
A.4 All rotation curves

In this appendix, we present all 45 rotation curves included in this analysis. Each curve was measured following the process described in Section 3.3. Spatially resolved spectra were extracted as described in Section 3.3.1, and kinematic measurements were obtained by spectral fits performed using PPXF (Section 3.3.3). Each rotation curve consists of three components: stellar velocity (gray stars), gas velocity from Balmer emission lines (orange circles), and gas velocity from forbidden emission lines. Whenever possible, the forbidden emission line velocities are measured from [O III] (teal circles). [O II] (purple circles) were used for spectra obtained using the 5000Å dichroic. When gas emission was faint ($H\beta$ equivalent width less than 0.5Å or [O III] equivalent width less than 2.0 Å), we use longer wavelengths to perform kinematic measurements. In this case, Balmer gas velocities were measured from $H\alpha$ and [S II] (blue circles) were used to measure the forbidden emission line component.

Gray shaded regions denote the rotation curve predicted by assuming an NFW dark matter profile, with halo mass obtained using abundance matching, with the MPA stellar mass as input (see Section 3.4). The spatial axis is normalized by the SDSS r-band petrosian radius, r_{50} .

The velocity measurements and associated errors are corrected for disc inclination as described in Appendix A.3. The angle relative to the normal of the disc and the stellar mass, as listed in the MPA-JHU catalogue, are shown in the bottom left of each curve plot. Δ_{off} is shown on the bottom right.

Asymmetric drift, or the difference between the local circular speed and the mean rotation of the galaxy, acts to reduce the observed rotational velocity due to the presence of randomly oriented and non-circular orbits. In the absence of gas surface density measurements, we do not correct for asymmetric drift.



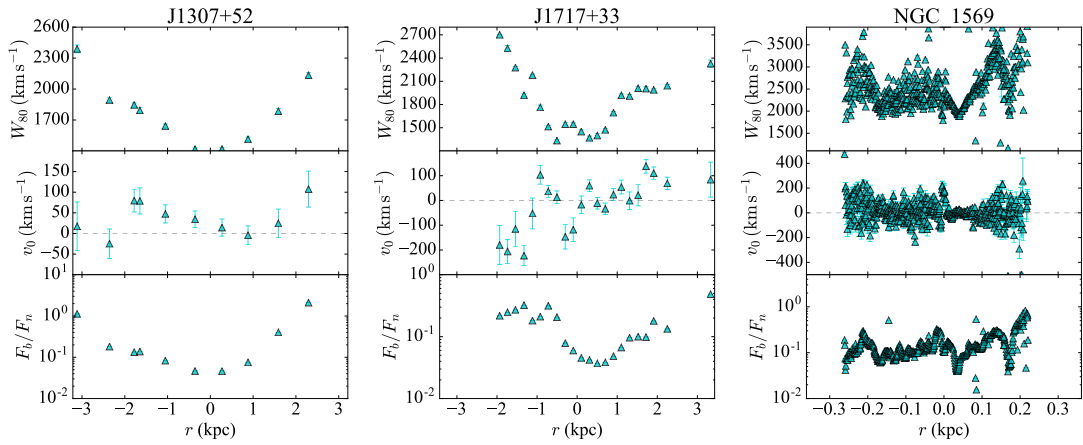


Figure A.1: Spatially resolved properties of outflows are presented for the remaining 12 galaxies, as in Fig. 2.7. Consistent with the scheme used throughout this paper, AGN-driven outflows are plotted with pink circles, star forming with cyan triangles, and AGN with SF outflows with black diamonds.

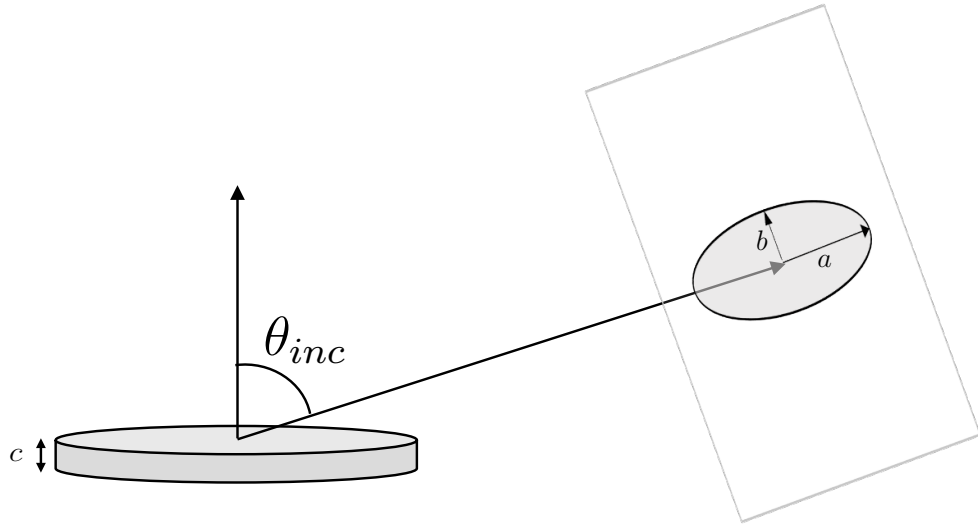


Figure A.2: A diagram to illustrate how a disc with thickness c appears as an ellipse when viewed from the inclination angle θ_{inc} . The inclination angle can be estimated by measuring the ellipse semimajor and minor axes a , b and assuming the disc thickness c .

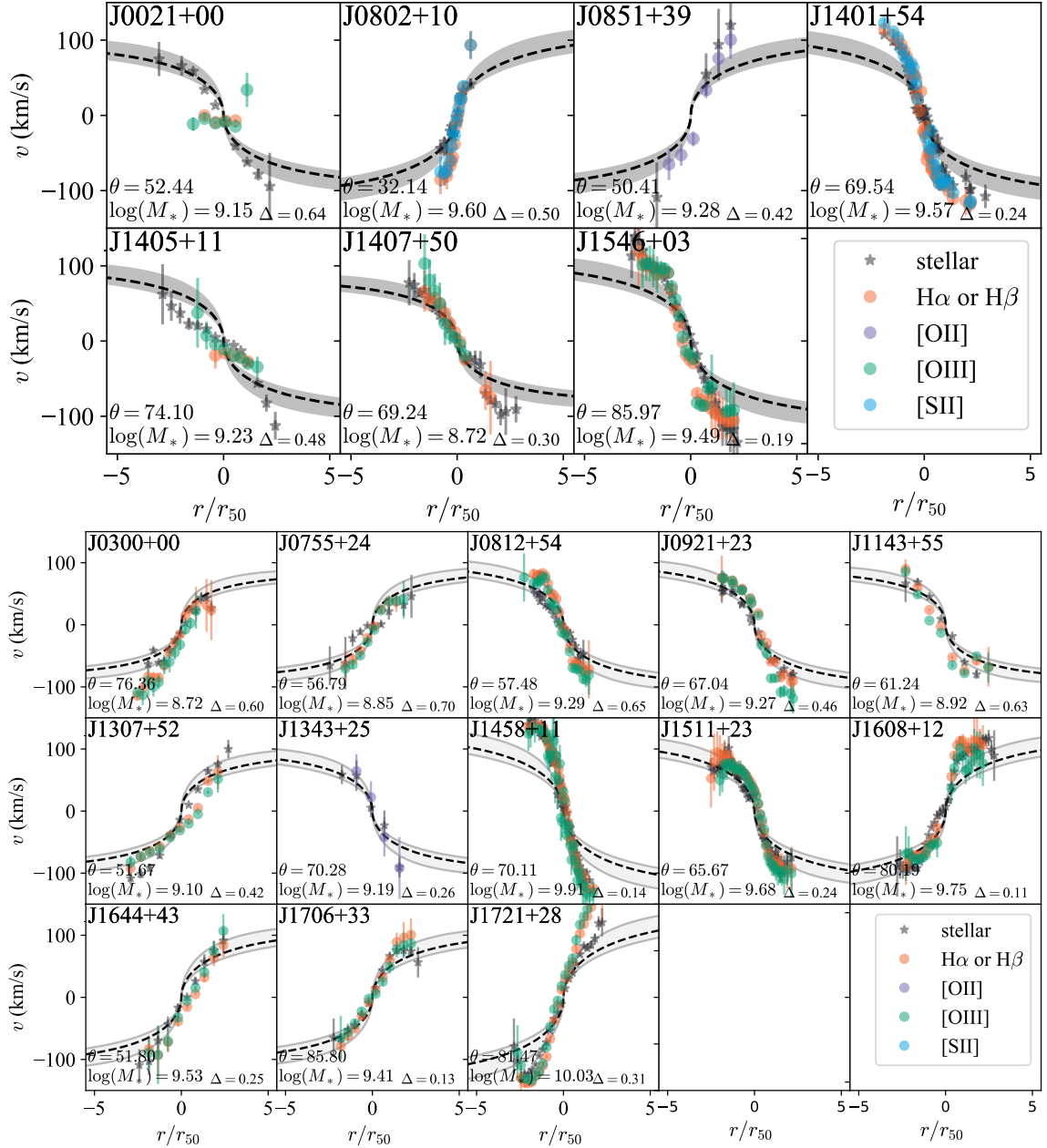


Figure A.3: Twenty of the 45 galaxies with rotation curves have gas that rotates with the stellar component. The shaded regions denote velocity curves following NFW profiles, assuming concentration parameters between $c = 8, 15$. Galaxies hosting AGN are shown in the top panel and star forming galaxies are in the bottom.

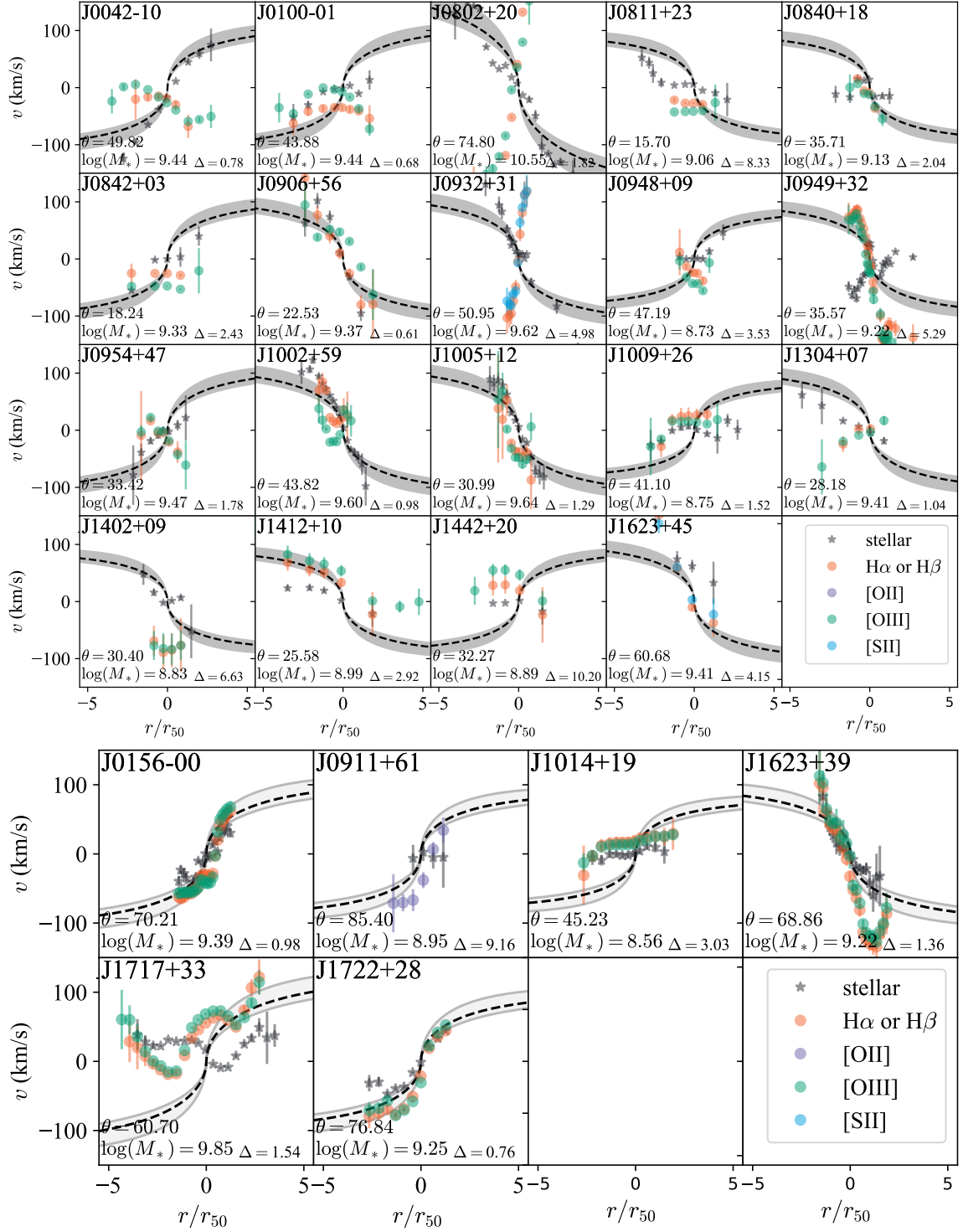


Figure A.4: Twenty-five of the 45 galaxies with rotation curves have disturbed gas. See Section 3.4.2 for a discussion on how we classify galaxies as disturbed. Galaxies hosting AGN are shown in the top group and star forming galaxies are in the bottom.

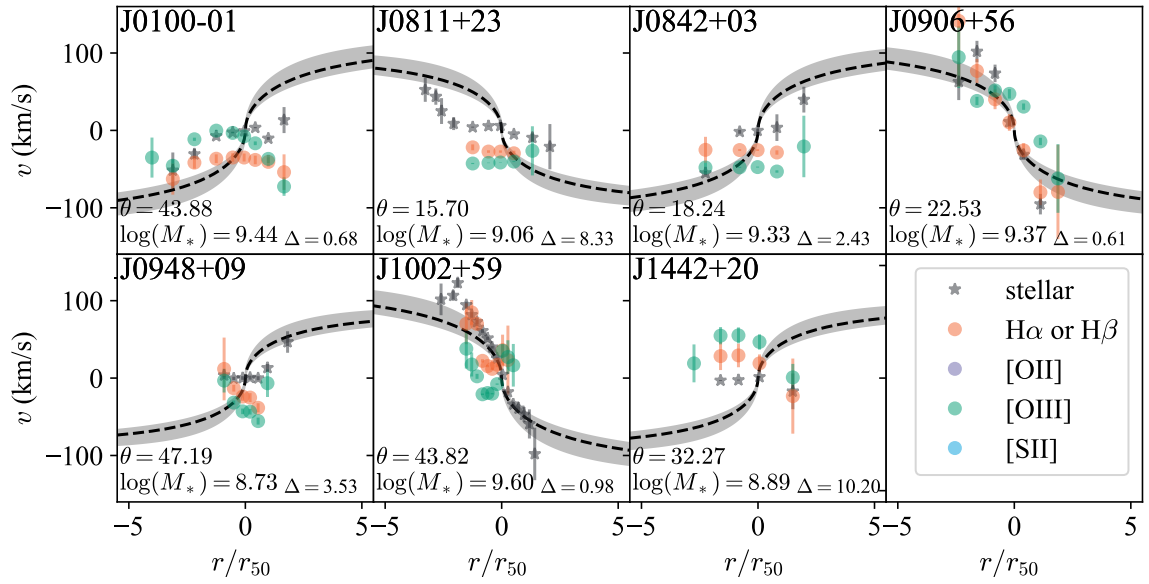


Figure A.5: Eight of the 45 galaxies with rotation curves show stratification in their emission lines. See Section 3.4.2 for a discussion on how we identify line stratification. Line of sight velocity gradients are shown for J0811+23 and J0842+03, as they are considered face-on based on their small inclination angles ($\theta < 20^\circ$) and thus are not corrected for inclination (as described in Appendix A.4). Rotational velocity curves (corrected for disc inclination) are shown for all other galaxies in this figure.

Bibliography

- [1] K. N. Abazajian, J. K. Adelman-McCarthy, M. A. Agüeros, S. S. Allam, C. Allende Prieto, D. An, K. S. J. Anderson, S. F. Anderson, J. Annis, N. A. Bahcall, and et al. The Seventh Data Release of the Sloan Digital Sky Survey. , 182:543–558, June 2009.
- [2] J. J. Adams, J. D. Simon, M. H. Fabricius, R. C. E. van den Bosch, J. C. Barentine, R. Bender, K. Gebhardt, G. J. Hill, J. D. Murphy, R. A. Swaters, J. Thomas, and G. van de Ven. Dwarf Galaxy Dark Matter Density Profiles Inferred from Stellar and Gas Kinematics. , 789:63, July 2014.
- [3] H. Aihara et al. The Eighth Data Release of the Sloan Digital Sky Survey: First Data from SDSS-III. , 193:29, April 2011.
- [4] M. G. Allen, B. A. Groves, M. A. Dopita, R. S. Sutherland, and L. J. Kewley. The MAPPINGS III Library of Fast Radiative Shock Models. , 178:20–55, September 2008.
- [5] Irham Taufik Andika, Mochamad Ikbil Arifyanto, and Wolfram Kollatschny. A study of [o iii]/[o ii] lines ratio in type 1 active galactic nucleus: Influence of radio jets and eddington ratio to narrow line region emission. *Astronomische Nachrichten*, n/a(n/a), 2020.
- [6] H. B. Ann, C. Park, and Y.-Y. Choi. Galactic satellite systems: radial distribution and environment dependence of galaxy morphology. , 389:86–92, September 2008.
- [7] K. Aylor, G. Rude, A. Medling, G. Canalizo, C. E. Max, and R. R. Antonucci. Kinematics of the Central Kiloparsec in Cygnus A from AO Integral Field Spectroscopy. In *American Astronomical Society Meeting Abstracts #221*, volume 221, page 339.16, January 2013.
- [8] V. F. Baldassare, A. E. Reines, E. Gallo, J. E. Greene, O. Graur, M. Geha, K. Hainline, C. M. Carroll, and R. C. Hickox. Multi-epoch Spectroscopy of Dwarf Galaxies with AGN Signatures: Identifying Sources with Persistent Broad H α Emission. , 829:57, September 2016.
- [9] Vivienne F. Baldassare, Marla Geha, and Jenny Greene. A Search for Optical AGN Variability in 35,000 Low-mass Galaxies with the Palomar Transient Factory. , 896(1):10, June 2020.
- [10] I. K. Baldry, K. Glazebrook, J. Brinkmann, Ž. Ivezić, R. H. Lupton, R. C. Nichol, and A. S. Szalay. Quantifying the Bimodal Color-Magnitude Distribution of Galaxies. , 600:681–694, January 2004.

- [11] J. A. Baldwin, M. M. Phillips, and R. Terlevich. Classification parameters for the emission-line spectra of extragalactic objects. , 93:5–19, February 1981.
- [12] J. A. Baldwin, M. M. Phillips, and R. Terlevich. Classification parameters for the emission-line spectra of extragalactic objects. , 93:5–19, February 1981.
- [13] Paramita Barai and Elisabete M. de Gouveia Dal Pino. Intermediate-Mass Black Hole Feedback in Dwarf Galaxies: a View from Cosmological Simulations. *arXiv e-prints*, page arXiv:1811.06576, Nov 2018.
- [14] J. E. Barnes and L. Hernquist. Dynamics of interacting galaxies. , 30:705–742, 1992.
- [15] Dalya Baron, Hagai Netzer, J. Xavier Prochaska, Zheng Cai, Sebastiano Cantalupo, D. Christopher Martin, Mateusz Matuszewski, Anna M. Moore, Patrick Morrissey, and James D. Neill. Direct evidence of AGN feedback: a post-starburst galaxy stripped of its gas by AGN-driven winds. , 480(3):3993–4016, Nov 2018.
- [16] G. Barro, S. M. Faber, P. G. Pérez-González, C. Pacifici, J. R. Trump, D. C. Koo, S. Wuyts, Y. Guo, E. Bell, A. Dekel, L. Porter, J. Primack, H. Ferguson, M. L. N. Ashby, K. Caputi, D. Ceverino, D. Croton, G. G. Fazio, M. Giavalisco, L. Hsu, D. Kocevski, A. Koekemoer, P. Kurczynski, P. Kollipara, J. Lee, D. H. McIntosh, E. McGrath, C. Moody, R. Somerville, C. Papovich, M. Salvato, P. Santini, T. Tal, A. van der Wel, C. C. Williams, S. P. Willner, and A. Zolotov. CANDELS+3D-HST: Compact SFGs at $z \sim 2-3$, the Progenitors of the First Quiescent Galaxies. , 791:52, Aug 2014.
- [17] A. J. Barth, L. C. Ho, R. E. Rutledge, and W. L. W. Sargent. POX 52: A Dwarf Seyfert 1 Galaxy with an Intermediate-Mass Black Hole. , 607:90–102, May 2004.
- [18] E. J. Barton, M. J. Geller, and S. J. Kenyon. Tidally Triggered Star Formation in Close Pairs of Galaxies. , 530:660–679, February 2000.
- [19] P. S. Behroozi, R. H. Wechsler, and C. Conroy. The Average Star Formation Histories of Galaxies in Dark Matter Halos from $z = 0-8$. , 770:57, June 2013.
- [20] Jillian M. Bellovary, Colleen E. Cleary, Ferah Munshi, Michael Tremmel, Charlotte R. Christensen, Alyson Brooks, and Thomas R. Quinn. Multimessenger signatures of massive black holes in dwarf galaxies. , 482(3):2913–2923, Jan 2019.
- [21] N. Bennert, G. Canalizo, B. Jungwiert, A. Stockton, F. Schweizer, C. Y. Peng, and M. Lacy. Evidence for Merger Remnants in Early-Type Host Galaxies of Low-Redshift QSOs. , 677:846–857, April 2008.
- [22] A. J. Benson, R. G. Bower, C. S. Frenk, C. G. Lacey, C. M. Baugh, and S. Cole. What Shapes the Luminosity Function of Galaxies? , 599(1):38–49, December 2003.
- [23] A. J. Benson, C. G. Lacey, C. M. Baugh, S. Cole, and C. S. Frenk. The effects of photoionization on galaxy formation - I. Model and results at $z=0$. , 333:156–176, June 2002.
- [24] M. C. Bentz, K. D. Denney, C. J. Grier, A. J. Barth, B. M. Peterson, M. Vestergaard, V. N. Bennert, G. Canalizo, G. De Rosa, A. V. Filippenko, E. L. Gates, J. E. Greene,

- W. Li, M. A. Malkan, R. W. Pogge, D. Stern, T. Treu, and J.-H. Woo. The Low-luminosity End of the Radius-Luminosity Relationship for Active Galactic Nuclei. , 767:149, April 2013.
- [25] M. C. Bentz, K. Horne, A. J. Barth, V. N. Bennert, G. Canalizo, A. V. Filippenko, E. L. Gates, M. A. Malkan, T. Minezaki, T. Treu, J.-H. Woo, and J. L. Walsh. The Lick AGN Monitoring Project: Velocity-delay Maps from the Maximum-entropy Method for Arp 151. , 720:L46–L51, September 2010.
- [26] M. C. Bentz, J. L. Walsh, A. J. Barth, N. Baliber, N. Bennert, G. Canalizo, A. V. Filippenko, M. Ganeshalingam, E. L. Gates, J. E. Greene, M. G. Hidas, K. D. Hiner, N. Lee, W. Li, M. A. Malkan, T. Minezaki, F. J. D. Serduke, J. H. Shiode, J. M. Silverman, T. N. Steele, D. Stern, R. A. Street, C. E. Thornton, T. Treu, X. Wang, J.-H. Woo, and Y. Yoshii. First Results from the Lick AGN Monitoring Project: The Mass of the Black Hole in Arp 151. , 689:L21–L24, December 2008.
- [27] M. C. Bentz, J. L. Walsh, A. J. Barth, N. Baliber, V. N. Bennert, G. Canalizo, A. V. Filippenko, M. Ganeshalingam, E. L. Gates, J. E. Greene, M. G. Hidas, K. D. Hiner, N. Lee, W. Li, M. A. Malkan, T. Minezaki, Y. Sakata, F. J. D. Serduke, J. M. Silverman, T. N. Steele, D. Stern, R. A. Street, C. E. Thornton, T. Treu, X. Wang, J.-H. Woo, and Y. Yoshii. The Lick AGN Monitoring Project: Broad-line Region Radii and Black Hole Masses from Reverberation Mapping of $H\beta$. , 705:199–217, November 2009.
- [28] M. C. Bentz, J. L. Walsh, A. J. Barth, Y. Yoshii, J.-H. Woo, X. Wang, T. Treu, C. E. Thornton, R. A. Street, T. N. Steele, J. M. Silverman, F. J. D. Serduke, Y. Sakata, T. Minezaki, M. A. Malkan, W. Li, N. Lee, K. D. Hiner, M. G. Hidas, J. E. Greene, E. L. Gates, M. Ganeshalingam, A. V. Filippenko, G. Canalizo, V. N. Bennert, and N. Baliber. The Lick AGN Monitoring Project: Reverberation Mapping of Optical Hydrogen and Helium Recombination Lines. , 716:993–1011, June 2010.
- [29] M. Bernardi, A. Meert, R. K. Sheth, V. Vikram, M. Huertas-Company, S. Mei, and F. Shankar. The massive end of the luminosity and stellar mass functions: dependence on the fit to the light profile. , 436(1):697–704, November 2013.
- [30] M. Bernardi, F. Shankar, J. B. Hyde, S. Mei, F. Marulli, and R. K. Sheth. Galaxy luminosities, stellar masses, sizes, velocity dispersions as a function of morphological type. , 404(4):2087–2122, Jun 2010.
- [31] Keir L. Birchall, M. G. Watson, and J. Aird. X-ray detected AGN in SDSS dwarf galaxies. , 492(2):2268–2284, February 2020.
- [32] M. R. Blanton and S. Roweis. K-Corrections and Filter Transformations in the Ultraviolet, Optical, and Near-Infrared. , 133:734–754, February 2007.
- [33] M. R. Blanton, D. J. Schlegel, M. A. Strauss, J. Brinkmann, D. Finkbeiner, M. Fukugita, J. E. Gunn, D. W. Hogg, Ž. Ivezić, G. R. Knapp, R. H. Lupton, J. A. Munn, D. P. Schneider, M. Tegmark, and I. Zehavi. New York University Value-Added Galaxy Catalog: A Galaxy Catalog Based on New Public Surveys. , 129:2562–2578, June 2005.

- [34] G. R. Blumenthal, S. M. Faber, R. Flores, and J. R. Primack. Contraction of Dark Matter Galactic Halos Due to Baryonic Infall. , 301:27, February 1986.
- [35] G. R. Blumenthal, S. M. Faber, J. R. Primack, and M. J. Rees. Formation of galaxies and large-scale structure with cold dark matter. , 311:517–525, October 1984.
- [36] C. M. Booth and J. Schaye. Dark matter haloes determine the masses of supermassive black holes. , 405:L1–L5, June 2010.
- [37] R. G. Bower, A. J. Benson, R. Malbon, J. C. Helly, C. S. Frenk, C. M. Baugh, S. Cole, and C. G. Lacey. Breaking the hierarchy of galaxy formation. , 370:645–655, August 2006.
- [38] M. Boylan-Kolchin, J. S. Bullock, and M. Kaplinghat. The Milky Way’s bright satellites as an apparent failure of Λ CDM. , 422:1203–1218, May 2012.
- [39] M. Boylan-Kolchin, V. Springel, S. D. M. White, A. Jenkins, and G. Lemson. Resolving cosmic structure formation with the Millennium-II Simulation. , 398:1150–1164, September 2009.
- [40] Michael Boylan-Kolchin, James S. Bullock, and Manoj Kaplinghat. Too big to fail? The puzzling darkness of massive Milky Way subhaloes. , 415(1):L40–L44, July 2011.
- [41] Jeremy D. Bradford, Marla C. Geha, Jenny E. Greene, Amy E. Reines, and Claire M. Dickey. The Effect of AGNs on the Global H I Content of Isolated Low-mass Galaxies. , 861:50, Jul 2018.
- [42] Larry Bradley, Brigitta Sipőcz, Thomas Robitaille, Erik Tollerud, Zè Vinícius, Christoph Deil, Kyle Barbary, Hans Moritz Günther, Mihai Cara, Ivo Busko, Simon Conseil, Michael Droettboom, Azalee Bostroem, E. M. Bray, Lars Andersen Bratholm, Tom Wilson, Matt Craig, Geert Barentsen, Sergio Pascual, Axel Donath, Johnny Greco, Gabriel Perren, P. L. Lim, and Wolfgang Kerzendorf. *astropy/photutils: v0.6*, January 2019.
- [43] Iris Breda, Polychronis Papaderos, Jean Michel Gomes, José Manuel Vilchez, Bodo L. Ziegler, Michaela Hirschmann, Leandro S. M. Cardoso, Patricio Lagos, and Fernando Buitrago. Stellar age gradients and inside-out star formation quenching in galaxy bulges. , 635:A177, March 2020.
- [44] J. Brinchmann, S. Charlot, S. D. M. White, C. Tremonti, G. Kauffmann, T. Heckman, and J. Brinkmann. The physical properties of star-forming galaxies in the low-redshift Universe. , 351:1151–1179, July 2004.
- [45] A. M. Brooks, F. Governato, C. M. Booth, B. Willman, J. P. Gardner, J. Wadsley, G. Stinson, and T. Quinn. The Origin and Evolution of the Mass-Metallicity Relationship for Galaxies: Results from Cosmological N-Body Simulations. , 655(1):L17–L20, January 2007.
- [46] J. M. Budzynski, S. E. Kogosov, I. G. McCarthy, S. L. McGee, and V. Belokurov. The radial distribution of galaxies in groups and clusters. , 423:104–121, June 2012.
- [47] James S. Bullock and Michael Boylan-Kolchin. Small-Scale Challenges to the Λ CDM Paradigm. , 55(1):343–387, August 2017.

- [48] James S. Bullock, Andrey V. Kravtsov, and David H. Weinberg. Reionization and the Abundance of Galactic Satellites. , 539(2):517–521, August 2000.
- [49] K. Bundy, M. A. Bershady, D. R. Law, R. Yan, N. Drory, N. MacDonald, D. A. Wake, B. Cherinka, J. R. Sánchez-Gallego, A.-M. Weijmans, D. Thomas, C. Tremonti, K. Masters, L. Coccato, A. M. Diamond-Stanic, A. Aragón-Salamanca, V. Avila-Reese, C. Badenes, J. Falcón-Barroso, F. Belfiore, D. Bizyaev, G. A. Blanc, J. Bland-Hawthorn, M. R. Blanton, J. R. Brownstein, N. Byler, M. Cappellari, C. Conroy, A. A. Dutton, E. Emsellem, J. Etherington, P. M. Frinchaboy, H. Fu, J. E. Gunn, P. Harding, E. J. Johnston, G. Kauffmann, K. Kinemuchi, M. A. Klaene, J. H. Knapen, A. Leauthaud, C. Li, L. Lin, R. Maiolino, V. Malanushenko, E. Malanushenko, S. Mao, C. Maraston, R. M. McDermid, M. R. Merrifield, R. C. Nichol, D. Oravetz, K. Pan, J. K. Parejko, S. F. Sanchez, D. Schlegel, A. Simmons, O. Steele, M. Steinmetz, K. Thanjavur, B. A. Thompson, J. L. Tinker, R. C. E. van den Bosch, K. B. Westfall, D. Wilkinson, S. Wright, T. Xiao, and K. Zhang. Overview of the SDSS-IV MaNGA Survey: Mapping nearby Galaxies at Apache Point Observatory. , 798:7, January 2015.
- [50] R. C. Rockosi, R. Stover, C. Kibrick, M. Lockwood, D. Peck, M. Cowley, S. Bolte, B. Adkins, S. Alcott, B. L. Allen, G. Brown, W Cabak, D Deich, M Hilyard, K Kassis, J Lanclos, T Lewis, A Pfister, L Phillips, M Robinson, M Saylor, J Thompson, M Ward, C Wei, and Wright. The low-resolution imaging spectrograph red channel ccd upgrade: fully depleted, high-resistivity ccds for keck. *Proc.SPIE*, 7735:7735 – 7735 – 11, 2010.
- [51] F. Calura, A. Pipino, C. Chiappini, F. Matteucci, and R. Maiolino. The evolution of the mass-metallicity relation in galaxies of different morphological types. , 504(2):373–388, September 2009.
- [52] Daniela Calzetti, Lee Armus, Ralph C. Bohlin, Anne L. Kinney, Jan Koornneef, and Thaisa Storchi-Bergmann. The Dust Content and Opacity of Actively Star-forming Galaxies. , 533(2):682–695, April 2000.
- [53] G. Canalizo, N. Bennert, B. Jungwiert, A. Stockton, F. Schweizer, M. Lacy, and C. Peng. Spectacular Shells in the Host Galaxy of the QSO MC2 1635+119. , 669:801–809, November 2007.
- [54] G. Canalizo and A. Stockton. Intermediate-age Stellar Populations in Classical Quasistellar Object Host Galaxies. , 772:132, August 2013.
- [55] G. Canalizo, A. Stockton, M. S. Brotherton, and M. Lacy. Star formation in QSO host galaxies. *New Astronomy Review*, 50:650–656, November 2006.
- [56] G. Canalizo, M. Wold, K. D. Hiner, M. Lazarova, M. Lacy, and K. Aylor. Probing the $M_{\text{BH}}-\sigma_*$ Relation in the Non-local Universe Using Red QSOs. , 760:38, November 2012.
- [57] G. Canalizo, M. Wold, M. Lazarova, and M. Lacy. Quasar Black Hole Masses from Velocity Dispersions. In S. K. Chakrabarti & A. S. Majumdar, editor, *American Institute of Physics Conference Series*, volume 1053 of *American Institute of Physics Conference Series*, pages 63–66, October 2008.

- [58] J. M. Cann, S. Satyapal, N. P. Abel, L. Blecha, R. F. Mushotzky, C. S. Reynolds, and N. J. Secrest. The Limitations of Optical Spectroscopic Diagnostics in Identifying Active Galactic Nuclei in the Low-mass Regime. , 870:L2, January 2019.
- [59] M. Cappellari. Improving the full spectrum fitting method: accurate convolution with Gauss-Hermite functions. , 466:798–811, April 2017.
- [60] B. Catinella, D. Schiminovich, G. Kauffmann, S. Fabello, J. Wang, and et al. The GALEX Arcibo SDSS Survey - I. Gas fraction scaling relations of massive galaxies and first data release. , 403:683–708, April 2010.
- [61] G. Chabrier. The Galactic Disk Mass Function: Reconciliation of the Hubble Space Telescope and Nearby Determinations. , 586:L133–L136, April 2003.
- [62] J. Chen. Color dependence in the spatial distribution of satellite galaxies. , 484:347–354, June 2008.
- [63] J. Chen, A. V. Kravtsov, F. Prada, E. S. Sheldon, A. A. Klypin, M. R. Blanton, J. Brinkmann, and A. R. Thakar. Constraining the Projected Radial Distribution of Galactic Satellites with the Sloan Digital Sky Survey. , 647:86–101, August 2006.
- [64] Edmond Cheung, Kevin Bundy, Michele Cappellari, Sébastien Peirani, Wiphu Rujopakarn, Kyle Westfall, Renbin Yan, Matthew Bershady, Jenny E. Greene, Timothy M. Heckman, Niv Drory, David R. Law, Karen L. Masters, Daniel Thomas, David A. Wake, Anne-Marie Weijmans, Kate Rubin, Francesco Belfiore, Benedetta Vulcani, Yan-Mei Chen, Kai Zhang, Joseph D. Gelfand , Dmitry Bizyaev, A. Roman-Lopes, and Donald P. Schneider. Suppressing star formation in quiescent galaxies with supermassive black hole winds. , 533:504–508, May 2016.
- [65] E. Choi, J. P. Ostriker, T. Naab, and P. H. Johansson. Radiative and Momentum-based Mechanical Active Galactic Nucleus Feedback in a Three-dimensional Galaxy Evolution Code. , 754:125, August 2012.
- [66] C. Cicone, R. Maiolino, E. Sturm, J. Graciá-Carpio, C. Feruglio, R. Neri, S. Aalto, R. Davies, F. Fiore, J. Fischer, S. García-Burillo, E. González-Alfonso, S. Hailey-Dunsheath, E. Piconcelli, and S. Veilleux. Massive molecular outflows and evidence for AGN feedback from CO observations. , 562:A21, Feb 2014.
- [67] Claudia Cicone, Marcella Brusa, Cristina Ramos Almeida, Giovanni Cresci, Bernd Husemann, and Vincenzo Mainieri. The largely unconstrained multiphase nature of outflows in AGN host galaxies. *Nature Astronomy*, 2:176–178, Feb 2018.
- [68] R. Cid Fernandes, R. M. González Delgado, R. García Benito, E. Pérez, A. L. de Amorim, S. F. Sánchez, B. Husemann, J. Falcón Barroso, R. López-Fernández, P. Sánchez-Blázquez, N. Vale Asari, A. Vazdekis, C. J. Walcher, and D. Mast. Resolving galaxies in time and space. II. Uncertainties in the spectral synthesis of datacubes. , 561:A130, January 2014.
- [69] R. Cid Fernandes, G. Stasińska, A. Mateus, and N. Vale Asari. A comprehensive classification of galaxies in the Sloan Digital Sky Survey: how to tell true from fake AGN? , 413:1687–1699, May 2011.

- [70] A. Cimatti, M. Brusa, M. Talia, M. Mignoli, G. Rodighiero, J. Kurk, P. Cassata, C. Halliday, A. Renzini, and E. Daddi. Active Galactic Nucleus Feedback at $z \sim 2$ and the Mutual Evolution of Active and Inactive Galaxies. , 779:L13, December 2013.
- [71] B. Coelho, S. Antón, C. Lobo, and B. Ribeiro. Red bulgeless galaxies in SDSS DR7. Are there any AGN hosts? , 436:2426–2434, December 2013.
- [72] A. L. Coil, J. A. Newman, D. Croton, M. C. Cooper, M. Davis, S. M. Faber, B. F. Gerke, D. C. Koo, N. Padmanabhan, R. H. Wechsler, and B. J. Weiner. The DEEP2 Galaxy Redshift Survey: Color and Luminosity Dependence of Galaxy Clustering at $z \sim 1$. , 672:153–176, January 2008.
- [73] M. Colless, G. Dalton, S. Maddox, W. Sutherland, P. Norberg, S. Cole, J. Bland-Hawthorn, and Bridges. The 2dF Galaxy Redshift Survey: spectra and redshifts. , 328:1039–1063, December 2001.
- [74] C. Conroy, J. E. Gunn, and M. White. The Propagation of Uncertainties in Stellar Population Synthesis Modeling. I. The Relevance of Uncertain Aspects of Stellar Evolution and the Initial Mass Function to the Derived Physical Properties of Galaxies. , 699:486–506, July 2009.
- [75] C. Conroy and R. H. Wechsler. Connecting Galaxies, Halos, and Star Formation Rates Across Cosmic Time. , 696:620–635, May 2009.
- [76] C. Conroy, R. H. Wechsler, and A. V. Kravtsov. The Hierarchical Build-Up of Massive Galaxies and the Intracluster Light since $z = 1$. , 668:826–838, October 2007.
- [77] Charlie Conroy. Modeling the Panchromatic Spectral Energy Distributions of Galaxies. , 51(1):393–455, August 2013.
- [78] E. Contini, G. De Lucia, Á. Villalobos, and S. Borgani. On the formation and physical properties of the intracluster light in hierarchical galaxy formation models. , 437:3787–3802, February 2014.
- [79] S. Côté, C. Carignan, and K. C. Freeman. The Various Kinematics of Dwarf Irregular Galaxies in Nearby Groups and Their Dark Matter Distributions. , 120:3027–3059, December 2000.
- [80] D. M. Crenshaw, H. R. Schmitt, S. B. Kraemer, R. F. Mushotzky, and J. P. Dunn. Radial Velocity Offsets Due to Mass Outflows and Extinction in Active Galactic Nuclei. , 708:419–426, January 2010.
- [81] S. M. Croom, K. Rhook, E. A. Corbett, B. J. Boyle, H. Netzer, N. S. Loaring, L. Miller, P. J. Outram, T. Shanks, and R. J. Smith. The correlation of line strength with luminosity and redshift from composite quasi-stellar object spectra. , 337(1):275–292, November 2002.
- [82] D. J. Croton, V. Springel, S. D. M. White, G. De Lucia, C. S. Frenk, L. Gao, A. Jenkins, G. Kauffmann, J. F. Navarro, and N. Yoshida. The many lives of active galactic nuclei: cooling flows, black holes and the luminosities and colours of galaxies. , 365:11–28, January 2006.

- [83] C. E. Cunha, M. Lima, H. Oyaizu, J. Frieman, and H. Lin. Estimating the redshift distribution of photometric galaxy samples - II. Applications and tests of a new method. , 396:2379–2398, July 2009.
- [84] Julianne J. Dalcanton, Peter Yoachim, and Rebecca A. Bernstein. The Formation of Dust Lanes: Implications for Galaxy Evolution. , 608(1):189–207, June 2004.
- [85] G. Dashyan, J. Silk, G. A. Mamon, Y. Dubois, and T. Hartwig. AGN feedback in dwarf galaxies? *ArXiv e-prints*, October 2017.
- [86] Romeel Davé, Kristian Finlator, Benjamin D. Oppenheimer, Mark Fardal, Neal Katz, Dušan Kereš, and David H. Weinberg. The nature of submillimetre galaxies in cosmological hydrodynamic simulations. , 404(3):1355–1368, May 2010.
- [87] R. L. Davies, B. Groves, L. J. Kewley, A. M. Medling, P. Shastri, J. Maithil, P. Kharb, J. Banfield, F. Longbottom, M. A. Dopita, E. J. Hampton, J. Scharwächter, R. Sutherland, C. Jin, I. Zaw, B. James, and S. Juneau. Dissecting galaxies: separating star formation, shock excitation and AGN activity in the central region of NGC 613. , 470:4974–4988, October 2017.
- [88] W. J. G. de Blok. The Core-Cusp Problem. *Advances in Astronomy*, 2010:789293, January 2010.
- [89] W. J. G. de Blok and A. Bosma. High-resolution rotation curves of low surface brightness galaxies. , 385:816–846, April 2002.
- [90] W. J. G. de Blok, S. S. McGaugh, A. Bosma, and V. C. Rubin. Mass Density Profiles of Low Surface Brightness Galaxies. , 552:L23–L26, May 2001.
- [91] D. S. De Young. Star formation in radio galaxies at large redshift. , 342:L59–L62, July 1989.
- [92] T. Di Matteo, V. Springel, and L. Hernquist. Energy input from quasars regulates the growth and activity of black holes and their host galaxies. , 433:604–607, February 2005.
- [93] C. Dickey, M. Geha, A. Wetzel, and K. El-Badry. AGN All the Way Down? AGN-like Line Ratios are Common In the Lowest-Mass Isolated Quiescent Galaxies. *arXiv e-prints*, February 2019.
- [94] Ruth Digby, Julio F. Navarro, Azadeh Fattahi, Christine M. Simpson, Kyle A. Oman, Facundo A. Gomez, Carlos S. Frenk, Robert J. J. Grand, and Ruediger Pakmor. The star formation histories of dwarf galaxies in Local Group cosmological simulations. , 485(4):5423–5437, June 2019.
- [95] K. Dolag, S. Borgani, G. Murante, and V. Springel. Substructures in hydrodynamical cluster simulations. , 399:497–514, October 2009.
- [96] E. Donoso, Lin Yan, C. Tsai, P. Eisenhardt, D. Stern, R. J. Assef, D. Leisawitz, T. H. Jarrett, and S. A. Stanford. Origin of 12 μm Emission across Galaxy Populations from WISE and SDSS Surveys. , 748:80, Apr 2012.
- [97] M. A. Dopita and R. S. Sutherland. Spectral Signatures of Fast Shocks. II. Optical Diagnostic Diagrams. , 455:468, December 1995.

- [98] Y. Dubois, S. Peirani, C. Pichon, J. Devriendt, R. Gavazzi, C. Welker, and M. Volonteri. The HORIZON-AGN simulation: morphological diversity of galaxies promoted by AGN feedback. , 463:3948–3964, December 2016.
- [99] H. Ebeling, L. N. Stephenson, and A. C. Edge. Jellyfish: Evidence of Extreme Ram-pressure Stripping in Massive Galaxy Clusters. , 781:L40, February 2014.
- [100] I. Ebrova, B. Jungwiert, G. Canalizo, N. Bennert, and L. Jilkova. Shell Galaxies: Dynamical Friction, Gradual Satellite Decay and Merger Dating. *ArXiv e-prints*, August 2009.
- [101] S. L. Ellison, D. R. Patton, L. Simard, and A. W. McConnachie. Galaxy Pairs in the Sloan Digital Sky Survey. I. Star Formation, Active Galactic Nucleus Fraction, and the Mass-Metallicity Relation. , 135:1877–1899, May 2008.
- [102] S. L. Ellison, D. R. Patton, L. Simard, A. W. McConnachie, I. K. Baldry, and J. T. Mendel. Galaxy pairs in the Sloan Digital Sky Survey - II. The effect of environment on interactions. , 407:1514–1528, September 2010.
- [103] Andrew Emerick, Greg L. Bryan, and Mordecai-Mark Mac Low. Stellar Radiation Is Critical for Regulating Star Formation and Driving Outflows in Low-mass Dwarf Galaxies. , 865(2):L22, October 2018.
- [104] C. Evoli, P. Salucci, A. Lapi, and L. Danese. The H I Content of Local Late-type Galaxies. , 743:45, December 2011.
- [105] A. C. Fabian. Observational Evidence of Active Galactic Nuclei Feedback. , 50:455–489, September 2012.
- [106] J. Falcón-Barroso, P. Sánchez-Blázquez, A. Vazdekis, E. Ricciardelli, N. Cardiel, A. J. Cenarro, J. Gorgas, and R. F. Peletier. An updated MILES stellar library and stellar population models. , 532:A95, August 2011.
- [107] I. Ferrero, M. G. Abadi, J. F. Navarro, L. V. Sales, and S. Gurovich. The dark matter haloes of dwarf galaxies: a challenge for the Λ cold dark matter paradigm? , 425:2817–2823, October 2012.
- [108] A. V. Filippenko and J. P. Halpern. NGC 7213 : a key to the nature of liners ? , 285:458–476, October 1984.
- [109] A. V. Filippenko and W. L. W. Sargent. Discovery of an extremely low luminosity Seyfert 1 nucleus in the dwarf galaxy NGC 4395. , 342:L11–L14, July 1989.
- [110] F. Fiore, C. Feruglio, F. Shankar, M. Bischetti, A. Bongiorno, M. Brusa, S. Carniani, C. Cicone, F. Duras, A. Lamastra, V. Mainieri, A. Marconi, N. Menci, R. Maiolino, E. Piconcelli, G. Vietri, and L. Zappacosta. AGN wind scaling relations and the co-evolution of black holes and galaxies. , 601:A143, May 2017.
- [111] Ricardo A. Flores and Joel R. Primack. Observational and Theoretical Constraints on Singular Dark Matter Halos. , 427:L1, May 1994.
- [112] A. S. Font, R. G. Bower, I. G. McCarthy, A. J. Benson, C. S. Frenk, J. C. Helly, C. G. Lacey, C. M. Baugh, and S. Cole. The colours of satellite galaxies in groups and clusters. , 389:1619–1629, October 2008.

- [113] D. Foreman-Mackey, D. W. Hogg, D. Lang, and J. Goodman. emcee: The mcmc hammer. *PASP*, 125:306–312, 2013.
- [114] V. Gaibler, S. Khochfar, M. Krause, and J. Silk. Jet-induced star formation in gas-rich galaxies. , 425:438–449, September 2012.
- [115] Carme Gallart, Matteo Monelli, Lucio Mayer, Antonio Aparicio, Giuseppina Battaglia, Edouard J. Bernard, Santi Cassisi, Andrew A. Cole, Andrew E. Dolphin, Igor Drozdovsky, Sebastian L. Hidalgo, Julio F. Navarro, Stefania Salvadori, Evan D. Skillman, Peter B. Stetson, and Daniel R. Weisz. The ACS LCID Project: On the Origin of Dwarf Galaxy Types—A Manifestation of the Halo Assembly Bias? , 811(2):L18, October 2015.
- [116] Anna Gallazzi, Stéphane Charlot, Jarle Brinchmann, Simon D. M. White, and Christy A. Tremonti. The ages and metallicities of galaxies in the local universe. , 362(1):41–58, September 2005.
- [117] L. Gao, G. De Lucia, S. D. M. White, and A. Jenkins. Galaxies and subhaloes in Λ CDM galaxy clusters. , 352:L1–L5, August 2004.
- [118] L. Gao, C. S. Frenk, M. Boylan-Kolchin, A. Jenkins, V. Springel, and S. D. M. White. The statistics of the subhalo abundance of dark matter haloes. , 410:2309–2314, February 2011.
- [119] L. Gao, J. F. Navarro, S. Cole, C. S. Frenk, S. D. M. White, V. Springel, A. Jenkins, and A. F. Neto. The redshift dependence of the structure of massive Λ cold dark matter haloes. , 387:536–544, June 2008.
- [120] L. Gao, S. D. M. White, A. Jenkins, F. Stoehr, and V. Springel. The subhalo populations of Λ CDM dark haloes. , 355:819–834, December 2004.
- [121] Junqiang Ge, Renbin Yan, Michele Cappellari, Shude Mao, Hongyu Li, and Youjun Lu. Recovering stellar population parameters via two full-spectrum fitting algorithms in the absence of model uncertainties. , 478(2):2633–2649, August 2018.
- [122] M. Geha, M. R. Blanton, R. Yan, and J. L. Tinker. A Stellar Mass Threshold for Quenching of Field Galaxies. , 757:85, September 2012.
- [123] S. Genel, M. Vogelsberger, V. Springel, D. Sijacki, D. Nelson, G. Snyder, V. Rodriguez-Gomez, P. Torrey, and L. Hernquist. Introducing the Illustris project: the evolution of galaxy populations across cosmic time. , 445:175–200, November 2014.
- [124] Armando Gil de Paz, Samuel Boissier, Barry F. Madore, Mark Seibert, Young H. Joe, Alessandro Boselli, Ted K. Wyder, David Thilker, Luciana Bianchi, Soo-Chang Rey, R. Michael Rich, Tom A. Barlow, Tim Conrow, Karl Forster, Peter G. Friedman, D. Christopher Martin, Patrick Morrissey, Susan G. Neff, David Schiminovich, Todd Small, José Donas, Timothy M. Heckman, Young-Wook Lee, Bruno Milliard, Alex S. Szalay, and Sukyoung Yi. The GALEX Ultraviolet Atlas of Nearby Galaxies. *The Astrophysical Journal Supplement Series*, 173:185–255, Dec 2007.
- [125] Riccardo Giovanelli, Martha P. Haynes, John J. Salzer, Gary Wegner, Luiz N. da Costa, and Wolfram Freudling. Extinction in SC Galaxies. , 107:2036, June 1994.

- [126] R. M. González Delgado, E. Pérez, R. Cid Fernández, R. García-Benito, A. L. de Amorim, S. F. Sánchez, B. Husemann, C. Cortijo-Ferrero, R. López Fernández, P. Sánchez-Blázquez, S. Bekeraite, C. J. Walcher, J. Falcón-Barroso, A. Gallazzi, G. van de Ven, J. Alves, J. Bland-Hawthorn, R. C. Kennicutt, D. Kupko, M. Lyubenova, D. Mast, M. Mollá, R. A. Marino, A. Quirrenbach, J. M. Vílchez, and L. Wisotzki. The star formation history of CALIFA galaxies: Radial structures. , 562:A47, February 2014.
- [127] F. Governato, C. Brook, L. Mayer, A. Brooks, G. Rhee, J. Wadsley, P. Jonsson, B. Willman, G. Stinson, T. Quinn, and P. Madau. Bulgeless dwarf galaxies and dark matter cores from supernova-driven outflows. , 463:203–206, January 2010.
- [128] J. E. Greene. Low-mass black holes as the remnants of primordial black hole formation. *Nature Communications*, 3:1304, December 2012.
- [129] J. E. Greene and L. C. Ho. A New Sample of Low-Mass Black Holes in Active Galaxies. , 670:92–104, November 2007.
- [130] J. E. Greene, N. L. Zakamska, L. C. Ho, and A. J. Barth. Feedback in Luminous Obscured Quasars. , 732:9, May 2011.
- [131] B. A. Groves, T. M. Heckman, and G. Kauffmann. Emission-line diagnostics of low-metallicity active galactic nuclei. , 371:1559–1569, October 2006.
- [132] H. Guo, Z. Zheng, I. Zehavi, H. Xu, D. J. Eisenstein, D. H. Weinberg, N. A. Bahcall, A. A. Berlind, J. Comparat, C. K. McBride, A. J. Ross, D. P. Schneider, R. A. Skibba, M. E. C. Swanson, J. L. Tinker, R. Tojeiro, and D. A. Wake. The clustering of galaxies in the SDSS-III Baryon Oscillation Spectroscopic Survey: modeling of the luminosity and colour dependence in the Data Release 10. *ArXiv e-prints*, January 2014.
- [133] Q. Guo, S. Cole, V. Eke, and C. Frenk. The satellite luminosity functions of galaxies in Sloan Digital Sky Survey. , 417:370–381, October 2011.
- [134] Q. Guo, S. Cole, V. Eke, and C. Frenk. Satellite galaxy number density profiles in the Sloan Digital Sky Survey. , 427:428–441, November 2012.
- [135] Q. Guo, S. Cole, V. Eke, C. Frenk, and J. Helly. Spatial and luminosity distributions of galactic satellites. , 434:1838–1848, September 2013.
- [136] Q. Guo and S. White. Numerical resolution limits on subhalo abundance matching. , 437:3228–3235, February 2014.
- [137] Q. Guo, S. White, R. E. Angulo, B. Henriques, G. Lemson, M. Boylan-Kolchin, P. Thomas, and C. Short. Galaxy formation in WMAP1 and WMAP7 cosmologies. *MNRAS*, 428:1351–1365, January 2013.
- [138] Q. Guo, S. White, M. Boylan-Kolchin, G. De Lucia, G. Kauffmann, G. Lemson, C. Li, V. Springel, and S. Weinmann. From dwarf spheroidals to cD galaxies: simulating the galaxy population in a Λ CDM cosmology. , 413:101–131, May 2011.
- [139] Q. Guo, S. White, C. Li, and M. Boylan-Kolchin. How do galaxies populate dark matter haloes? , 404:1111–1120, May 2010.

- [140] C. M. Harrison, D. M. Alexander, J. R. Mullaney, and A. M. Swinbank. Kiloparsec-scale outflows are prevalent among luminous AGN: outflows and feedback in the context of the overall AGN population. , 441:3306–3347, July 2014.
- [141] Timothy M. Heckman and Philip N. Best. The coevolution of galaxies and supermassive black holes: Insights from surveys of the contemporary universe. *Annual Review of Astronomy and Astrophysics*, 52(1):589–660, Aug 2014. Saved from BrowZine: <http://thirdiron.com/download>.
- [142] B. M. B. Henriques, S. D. M. White, G. Lemson, P. A. Thomas, Q. Guo, G.-D. Marleau, and R. A. Overzier. Confronting theoretical models with the observed evolution of the galaxy population out to $z=4$. , 421:2904–2916, April 2012.
- [143] B. M. B. Henriques, S. D. M. White, P. A. Thomas, R. E. Angulo, Q. Guo, G. Lemson, and V. Springel. Simulations of the galaxy population constrained by observations from $z=3$ to the present day: implications for galactic winds and the fate of their ejecta. , 431:3373–3395, June 2013.
- [144] K. D. Hiner and G. Canalizo. Kinematics of Stellar Populations in Poststarburst Galaxies. , 799:59, January 2015.
- [145] K. D. Hiner, G. Canalizo, M. Lacy, A. Sajina, L. Armus, S. Ridgway, and L. Storrie-Lombardi. An Infrared Comparison of Type-1 and Type-2 Quasars. , 706:508–515, November 2009.
- [146] K. D. Hiner, G. Canalizo, M. Wold, M. S. Brotherton, and S. L. Cales. Black-hole-Bulge Relationship of Post-starburst Quasars at $z \sim 0.3$. , 756:162, September 2012.
- [147] G. Hinshaw, D. Larson, E. Komatsu, D. N. Spergel, and et al. Nine-year Wilkinson Microwave Anisotropy Probe (WMAP) Observations: Cosmological Parameter Results. , 208:19, October 2013.
- [148] Paul W. Hodge. Dwarf Galaxies. , 9:35, January 1971.
- [149] E. Holmberg. A study of physical groups of galaxies. *Arkiv for Astronomi*, 5:305–343, 1969.
- [150] Chia-Yu Hu. Supernova-driven winds in simulated dwarf galaxies. , 483(3):3363–3381, March 2019.
- [151] S. Huang, M. P. Haynes, R. Giovanelli, and J. Brinchmann. The Arecibo Legacy Fast ALFA Survey: The Galaxy Population Detected by ALFALFA. , 756:113, September 2012.
- [152] G. Iorio, F. Fraternali, C. Nipoti, E. Di Teodoro, J. I. Read, and G. Battaglia. LITTLE THINGS in 3D: robust determination of the circular velocity of dwarf irregular galaxies. , 466:4159–4192, April 2017.
- [153] W. Ishibashi, A. C. Fabian, and R. E. A. Canning. Can AGN feedback-driven star formation explain the size evolution of massive galaxies? , 431:2350–2355, May 2013.
- [154] Joachim Janz, Samantha J. Penny, Alister W. Graham, Duncan A. Forbes, and Roger L. Davies. Implications for the origin of early-type dwarf galaxies - the discovery of rotation in isolated, low-mass early-type galaxies. , 468:2850–2864, Jul 2017.

- [155] T. H. Jarrett, M. Cohen, F. Masci, E. Wright, D. Stern, D. Benford, A. Blain, S. Carey, R. M. Cutri, P. Eisenhardt, C. Lonsdale, A. Mainzer, K. Marsh, D. Padgett, S. Petty, M. Ressler, M. Skrutskie, S. Stanford, J. Surace, C. W. Tsai, S. Wheelock, and D. L. Yan. The Spitzer-WISE Survey of the Ecliptic Poles. , 735:112, July 2011.
- [156] C. Y. Jiang, Y. P. Jing, and C. Li. The Distribution of Faint Satellites around Central Galaxies in the Canada-France-Hawaii Telescope Legacy Survey. , 760:16, November 2012.
- [157] Y.-F. Jiang, J. E. Greene, L. C. Ho, T. Xiao, and A. J. Barth. The Host Galaxies of Low-mass Black Holes. , 742:68, December 2011.
- [158] E. J. Johnston, A. Aragón-Salamanca, M. R. Merrifield, and A. G. Bedregal. Spectroscopic bulge-disc decomposition: a new method to study the evolution of lenticular galaxies. , 422:2590–2599, May 2012.
- [159] E. J. Johnston, A. Aragon-Salamanca, M. R. Merrifield, and A. G. Bedregal. Clues to the Formation of Lenticular Galaxies Using Spectroscopic Bulge-Disk Decomposition. *ArXiv e-prints*, September 2013.
- [160] X. Kang and F. C. van den Bosch. New Constraints on the Efficiencies of Ram Pressure Stripping and the Tidal Disruption of Satellite Galaxies. , 676:L101–L104, April 2008.
- [161] Ivan Yu. Katkov, Olga K. Sil’chenko, and Victor L. Afanasiev. Decoupled gas kinematics in isolated S0 galaxies. , 438(4):2798–2803, March 2014.
- [162] Harley Katz, Marius Ramsøy, Joakim Rosdahl, Taysun Kimm, Jérémy Blaizot, Martin G. Haehnelt, Léo Michel-Dansac, Thibault Garel, Clotilde Laigle, Julien Devriendt, and Adrienne Slyz. How to Quench a Dwarf Galaxy: The Impact of Inhomogeneous Reionization on Dwarf Galaxies and Cosmic Filaments. , March 2020.
- [163] G. Kauffmann, T. M. Heckman, C. Tremonti, J. Brinchmann, S. Charlot, S. D. M. White, S. E. Ridgway, J. Brinkmann, M. Fukugita, P. B. Hall, Ž. Ivezić, G. T. Richards, and D. P. Schneider. The host galaxies of active galactic nuclei. , 346:1055–1077, December 2003.
- [164] Sugata Kaviraj, Garreth Martin, and Joseph Silk. AGN in dwarf galaxies: frequency, triggering processes and the plausibility of AGN feedback. , page L103, Jun 2019.
- [165] L. J. Kewley, M. A. Dopita, R. S. Sutherland, C. A. Heisler, and J. Trevena. Theoretical Modeling of Starburst Galaxies. , 556:121–140, July 2001.
- [166] Lisa J. Kewley and Sara L. Ellison. Metallicity Calibrations and the Mass-Metallicity Relation for Star-forming Galaxies. , 681(2):1183–1204, Jul 2008.
- [167] A. Khalatyan, A. Cattaneo, M. Schramm, S. Gottlöber, M. Steinmetz, and L. Wisotzki. Is AGN feedback necessary to form red elliptical galaxies? , 387:13–30, Jun 2008.
- [168] T. Kimm, R. S. Somerville, S. K. Yi, F. C. van den Bosch, S. Salim, F. Fontanot, P. Monaco, H. Mo, A. Pasquali, R. M. Rich, and X. Yang. The correlation of star formation quenching with internal galaxy properties and environment. , 394:1131–1147, April 2009.

- [169] T. Kimm, S. K. Yi, and S. Khochfar. The Impact of Gas Stripping and Stellar Mass Loss on Satellite Galaxy Evolution. , 729:11, March 2011.
- [170] Anatoly Klypin, Andrey V. Kravtsov, Octavio Valenzuela, and Francisco Prada. Where Are the Missing Galactic Satellites? , 522(1):82–92, September 1999.
- [171] E. Komatsu, K. M. Smith, J. Dunkley, C. L. Bennett, B. Gold, G. Hinshaw, N. Jarosik, D. Larson, M. R. Nolte, L. Page, D. N. Spergel, M. Halpern, R. S. Hill, A. Kogut, M. Limon, S. S. Meyer, N. Odegard, G. S. Tucker, J. L. Weiland, E. Wollack, and E. L. Wright. Seven-year Wilkinson Microwave Anisotropy Probe (WMAP) Observations: Cosmological Interpretation. , 192(2):18, February 2011.
- [172] J. Kormendy, R. Bender, and M. E. Cornell. Supermassive black holes do not correlate with galaxy disks or pseudobulges. , 469:374–376, January 2011.
- [173] J. Kormendy, N. Drory, R. Bender, and M. E. Cornell. Bulgeless Giant Galaxies Challenge Our Picture of Galaxy Formation by Hierarchical Clustering. , 723:54–80, November 2010.
- [174] John Kormendy and Luis C. Ho. Coevolution (or not) of supermassive black holes and host galaxies. *Annual Review of Astronomy and Astrophysics*, 51(1):511–653, 2013.
- [175] Sophie Koudmani, Debora Sijacki, Martin A. Bourne, and Matthew C. Smith. Fast and energetic AGN-driven outflows in simulated dwarf galaxies. , 484:2047–2066, Apr 2019.
- [176] A. V. Kravtsov, O. Y. Gnedin, and A. A. Klypin. The Tumultuous Lives of Galactic Dwarfs and the Missing Satellites Problem. , 609:482–497, July 2004.
- [177] Mikkel T. Kristensen, Kevin Pimbblet, and Samantha Penny. Environments of dwarf galaxies with optical AGN characteristics. , June 2020.
- [178] F. La Franca, F. Onori, F. Ricci, E. Sani, M. Brusa, R. Maiolino, S. Bianchi, A. Bongiorno, F. Fiore, A. Marconi, and C. Vignali. Extending virial black hole mass estimates to low-luminosity or obscured AGN: the cases of NGC 4395 and MCG -01-24-012. , 449:1526–1535, May 2015.
- [179] E. Laag, S. Croft, G. Canalizo, and M. Lacy. The Multi-wavelength Extreme Starburst Sample of Luminous Galaxies Part I: Sample Characteristics. *ArXiv e-prints*, October 2010.
- [180] D. G. Lambas, P. B. Tissera, M. S. Alonso, and G. Coldwell. Galaxy pairs in the 2dF survey - I. Effects of interactions on star formation in the field. , 346:1189–1196, December 2003.
- [181] I. Lamperti, M. Koss, B. Trakhtenbrot, K. Schawinski, C. Ricci, K. Oh, H. Landt, R. Riffel, A. Rodríguez-Ardila, N. Gehrels, F. Harrison, N. Masetti, R. Mushotzky, E. Treister, Y. Ueda, and S. Veilleux. BAT AGN Spectroscopic Survey - IV: Near-Infrared Coronal Lines, Hidden Broad Lines, and Correlation with Hard X-ray Emission. , 467:540–572, May 2017.

- [182] M. Lares, D. G. Lambas, and M. J. Domínguez. Properties of Satellite Galaxies in the SDSS Photometric Survey: Luminosities, Colors, and Projected Number Density Profiles. , 142:13–+, July 2011.
- [183] M. S. Lazarova, G. Canalizo, M. Lacy, and A. Sajina. The Nature of LoBAL QSOs. I. SEDs and Mid-infrared Spectral Properties. , 755:29, August 2012.
- [184] G. Lemson and the Virgo Consortium. Halo and Galaxy Formation Histories from the Millennium Simulation: Public release of a VO-oriented and SQL-queryable database for studying the evolution of galaxies in the LambdaCDM cosmogony. *arXiv e-prints*, pages astro-ph/0608019, August 2006.
- [185] C. Li, G. Kauffmann, T. M. Heckman, Y. P. Jing, and S. D. M. White. Interaction-induced star formation in a complete sample of 10^5 nearby star-forming galaxies. , 385:1903–1914, April 2008.
- [186] C. Li, G. Kauffmann, Y. P. Jing, S. D. M. White, G. Börner, and F. Z. Cheng. The dependence of clustering on galaxy properties. , 368:21–36, May 2006.
- [187] C. Li and S. D. M. White. The distribution of stellar mass in the low-redshift Universe. , 398:2177–2187, October 2009.
- [188] Y.-S. Li, G. De Lucia, and A. Helmi. On the nature of the Milky Way satellites. , 401:2036–2052, January 2010.
- [189] Chris J. Lintott, Kevin Schawinski, William Keel, Hanny van Arkel, Nicola Bennert, Edward Edmondson, Daniel Thomas, Daniel J. B. Smith, Peter D. Herbert, Matt J. Jarvis, Shanil Virani, Dan Andreescu, Steven P. Bamford, Kate Land, Phil Murray, Robert C. Nichol, M. Jordan Raddick, Anže Slosar, Alex Szalay, and Jan Vandenberg. Galaxy Zoo: ‘Hanny’s Voorwerp’, a quasar light echo? , 399(1):129–140, Oct 2009.
- [190] E. L. Łokas and G. A. Mamon. Properties of spherical galaxies and clusters with an NFW density profile. , 321:155–166, February 2001.
- [191] S. J. Lorrimer, C. S. Frenk, R. M. Smith, S. D. M. White, and D. Zaritsky. The Distribution of Satellite Galaxies. , 269:696, August 1994.
- [192] M. R. Lovell, V. Eke, C. S. Frenk, L. Gao, A. Jenkins, T. Theuns, J. Wang, S. D. M. White, A. Boyarsky, and O. Ruchayskiy. The haloes of bright satellite galaxies in a warm dark matter universe. , 420:2318–2324, March 2012.
- [193] Mark R. Lovell, Carlos S. Frenk, Vincent R. Eke, Adrian Jenkins, Liang Gao, and Tom Theuns. The properties of warm dark matter haloes. , 439(1):300–317, March 2014.
- [194] R. Mandelbaum, C. M. Hirata, T. Broderick, U. Seljak, and J. Brinkmann. Ellipticity of dark matter haloes with galaxy-galaxy weak lensing. , 370:1008–1024, August 2006.
- [195] Christina M. Manzano-King, Gabriela Canalizo, and Laura V. Sales. AGN-Driven Outflows in Dwarf Galaxies. , 884(1):54, Oct 2019.
- [196] E. Mármol-Queraltó, I. Trujillo, P. G. Pérez-González, J. Varela, and G. Barro. Satellites around massive galaxies since z 2. , 422:2187–2194, May 2012.

- [197] C. L. Martin. The Impact of Star Formation on the Interstellar Medium in Dwarf Galaxies. II. The Formation of Galactic Winds. , 506:222–252, October 1998.
- [198] Crystal L. Martin. The impact of star formation on the interstellar medium in dwarf galaxies. ii. the formation of galactic winds. *The Astrophysical Journal*, 506(1):222, Oct 1998.
- [199] D. Christopher Martin, Ted K. Wyder, David Schiminovich, Tom A. Barlow, Karl Forster, Peter G. Friedman, Patrick Morrissey, Susan G. Neff, Mark Seibert, Todd Small, Barry Y. Welsh, Luciana Bianchi, José Donas, Timothy M. Heckman, Young-Wook Lee, Barry F. Madore, Bruno Milliard, R. Michael Rich, Alex S. Szalay, and Sukyoung K. Yi. The UV-Optical Galaxy Color-Magnitude Diagram. III. Constraints on Evolution from the Blue to the Red Sequence. *The Astrophysical Journal Supplement Series*, 173:342–356, Dec 2007.
- [200] I. Martín-Navarro and M. Mezcuá. Exploring the Limits of AGN Feedback: Black Holes and the Star Formation Histories of Low-mass Galaxies. , 855(2):L20, Mar 2018.
- [201] Davide Martizzi, Romain Teyssier, and Ben Moore. Cusp-core transformations induced by AGN feedback in the progenitors of cluster galaxies. , 432(3):1947–1954, Jul 2013.
- [202] Sergey Mashchenko, James Wadsley, and H. M. P. Couchman. Stellar Feedback in Dwarf Galaxy Formation. *Science*, 319(5860):174, Jan 2008.
- [203] Richard M. McDermid, Katherine Alatalo, Leo Blitz, Frédéric Bournaud, Martin Bureau, Michele Cappellari, Alison F. Crocker, Roger L. Davies, Timothy A. Davis, P. T. de Zeeuw, Pierre-Alain Duc, Eric Emsellem, Sadegh Khochfar, Davor Krajinović, Harald Kuntschner, Raffaella Morganti, Thorsten Naab, Tom Oosterloo, Marc Sarzi, Nicholas Scott, Paolo Serra, Anne-Marie Weijmans, and Lisa M. Young. The ATLAS^{3D} Project - XXX. Star formation histories and stellar population scaling relations of early-type galaxies. , 448(4):3484–3513, April 2015.
- [204] R. McElroy, S. M. Croom, M. Pracy, R. Sharp, I.-T. Ho, and A. M. Medling. IFU observations of luminous type II AGN - I. Evidence for ubiquitous winds. , 446:2186–2204, January 2015.
- [205] A. M. Medling, S. M. Ammons, C. E. Max, R. I. Davies, H. Engel, and G. Canalizo. Mass of the Southern Black Hole in NGC 6240 from Laser Guide Star Adaptive Optics. , 743:32, December 2011.
- [206] Mar Mezcuá. Dwarf galaxies might not be the birth sites of supermassive black holes. *Nature Astronomy*, 3:6–7, Jan 2019.
- [207] B. Moore, S. Ghigna, F. Governato, G. Lake, T. Quinn, J. Stadel, and P. Tozzi. Dark Matter Substructure within Galactic Halos. , 524:L19–L22, October 1999.
- [208] Ben Moore. Evidence against dissipation-less dark matter from observations of galaxy haloes. , 370(6491):629–631, August 1994.
- [209] E. C. Moran, K. Shahinyan, H. R. Sugarman, D. O. Vélez, and M. Eracleous. Black Holes At the Centers of Nearby Dwarf Galaxies. , 148:136, December 2014.

- [210] Edward C. Moran, Alexei V. Filippenko, and Ryan Chornock. “Hidden” Seyfert 2 Galaxies and the X-Ray Background. , 579(2):L71–L74, Nov 2002.
- [211] B. P. Moster, T. Naab, and S. D. M. White. Galactic star formation and accretion histories from matching galaxies to dark matter haloes. , page 321, December 2012.
- [212] B. P. Moster, T. Naab, and S. D. M. White. Galactic star formation and accretion histories from matching galaxies to dark matter haloes. , 428:3121–3138, February 2013.
- [213] B. P. Moster, R. S. Somerville, C. Maulbetsch, F. C. van den Bosch, A. V. Macciò, T. Naab, and L. Oser. Constraints on the Relationship between Stellar Mass and Halo Mass at Low and High Redshift. , 710:903–923, February 2010.
- [214] F. Müller-Sánchez, E. K. S. Hicks, M. Malkan, R. Davies, P. C. Yu, S. Shaver, and B. Davis. The Keck/OSIRIS Nearby AGN Survey (KONA) I. The Nuclear K-band Properties of Nearby AGN. *ArXiv e-prints*, May 2017.
- [215] T. Murayama and Y. Taniguchi. Where Is the Coronal Line Region in Active Galactic Nuclei? , 497:L9–L12, April 1998.
- [216] T. Naab and A. Burkert. Statistical Properties of Collisionless Equal- and Unequal-Mass Merger Remnants of Disk Galaxies. , 597:893–906, November 2003.
- [217] D. Nagai and A. V. Kravtsov. The Radial Distribution of Galaxies in A Cold Dark Matter Clusters. , 618:557–568, January 2005.
- [218] K. Nandra, A. Georgakakis, C. N. A. Willmer, M. C. Cooper, D. J. Croton, M. Davis, S. M. Faber, D. C. Koo, E. S. Laird, and J. A. Newman. AEGIS: The Color-Magnitude Relation for X-Ray-selected Active Galactic Nuclei. , 660:L11–L14, May 2007.
- [219] J. F. Navarro, C. S. Frenk, and S. D. M. White. The Structure of Cold Dark Matter Halos. , 462:563, May 1996.
- [220] J. F. Navarro, C. S. Frenk, and S. D. M. White. A Universal Density Profile from Hierarchical Clustering. , 490:493, December 1997.
- [221] A. M. Nierenberg, M. W. Auger, T. Treu, P. J. Marshall, and C. D. Fassnacht. Luminous Satellites of Early-type Galaxies. I. Spatial Distribution. , 731:44, April 2011.
- [222] A. M. Nierenberg, M. W. Auger, T. Treu, P. J. Marshall, C. D. Fassnacht, and M. T. Busha. Luminous Satellites. II. Spatial Distribution, Luminosity Function, and Cosmic Evolution. , 752:99, June 2012.
- [223] K. Oh, M. Sarzi, K. Schawinski, and S. K. Yi. Improved and Quality-assessed Emission and Absorption Line Measurements in Sloan Digital Sky Survey Galaxies. , 195:13, August 2011.
- [224] Se-Heon Oh, Chris Brook, Fabio Governato, Elias Brinks, Lucio Mayer, W. J. G. de Blok, Alyson Brooks, and Fabian Walter. The Central Slope of Dark Matter Cores in Dwarf Galaxies: Simulations versus THINGS. , 142(1):24, July 2011.

- [225] Se-Heon Oh, Deidre A. Hunter, Elias Brinks, Bruce G. Elmegreen, Andreas Schruba, Fabian Walter, Michael P. Rupen, Lisa M. Young, Caroline E. Simpson, Megan C. Johnson, Kimberly A. Herrmann, Dana Ficut-Vicas, Phil Cigan, Volker Heesen, Trisha Ashley, and Hong-Xin Zhang. High-resolution Mass Models of Dwarf Galaxies from LITTLE THINGS. , 149(6):180, June 2015.
- [226] J. B. Oke, J. G. Cohen, M. Carr, J. Cromer, A. Dingizian, F. H. Harris, S. Labrecque, R. Lucinio, W. Schaal, H. Epps, and J. Miller. The keck low-resolution imaging spectrometer. *Publications of the Astronomical Society of the Pacific*, 107:375, apr 1995.
- [227] K. A. Oman, J. F. Navarro, A. Fattahi, C. S. Frenk, T. Sawala, S. D. M. White, R. Bower, R. A. Crain, M. Furlong, M. Schaller, J. Schaye, and T. Theuns. The unexpected diversity of dwarf galaxy rotation curves. , 452:3650–3665, October 2015.
- [228] R. Pakmor, F. Marinacci, and V. Springel. Magnetic Fields in Cosmological Simulations of Disk Galaxies. , 783:L20, March 2014.
- [229] Benjamin Panter, Raul Jimenez, Alan F. Heavens, and Stephane Charlot. The cosmic evolution of metallicity from the SDSS fossil record. , 391(3):1117–1126, December 2008.
- [230] E. Papastergis, A. Cattaneo, S. Huang, R. Giovanelli, and M. P. Haynes. A Direct Measurement of the Baryonic Mass Function of Galaxies and Implications for the Galactic Baryon Fraction. , 759:138, November 2012.
- [231] E. Papastergis, R. Giovanelli, M. P. Haynes, and F. Shankar. Is there a ”too big to fail” problem in the field? , 574:A113, February 2015.
- [232] D. Park, J.-H. Woo, T. Treu, A. J. Barth, M. C. Bentz, V. N. Bennert, G. Canalizo, A. V. Filippenko, E. Gates, J. E. Greene, M. A. Malkan, and J. Walsh. The Lick AGN Monitoring Project: Recalibrating Single-epoch Virial Black Hole Mass Estimates. , 747:30, March 2012.
- [233] D. R. Patton, R. G. Carlberg, R. O. Marzke, C. J. Pritchett, L. N. da Costa, and P. S. Pellegrini. New Techniques for Relating Dynamically Close Galaxy Pairs to Merger and Accretion Rates: Application to the Second Southern Sky Redshift Survey. , 536:153–172, June 2000.
- [234] P. J. E. Peebles. Large-scale background temperature and mass fluctuations due to scale-invariant primeval perturbations. , 263:L1–L5, December 1982.
- [235] C. Y. Peng, L. C. Ho, C. D. Impey, and H.-W. Rix. Detailed Structural Decomposition of Galaxy Images. , 124:266–293, July 2002.
- [236] Y. Peng, R. Maiolino, and R. Cochrane. Strangulation as the primary mechanism for shutting down star formation in galaxies. , 521(7551):192–195, May 2015.
- [237] Ying-jie Peng, Simon J. Lilly, Katarina Kovač, Micol Bolzonella, Lucia Pozzetti, Alvio Renzini, Gianni Zamorani, Olivier Ilbert, Christian Knobel, Angela Iovino, Christian Maier, Olga Cucciati, Lidia Tasca, C. Marcella Carollo, John Silverman, Pawel Kampanyk, Loic de Ravel, David Sanders, Nicholas Scoville, Thierry Contini, Vincenzo Mainieri, Marco Scodreggio, Jean-Paul Kneib, Olivier Le Fèvre, Sandro Bardelli, Angela Bongiorno, Karina Caputi, Graziano Coppia, Sylvain de la Torre, Paolo Franzetti,

- Bianca Garilli, Fabrice Lamareille, Jean-Francois Le Borgne, Vincent Le Brun, Marco Mignoli, Enrique Perez Montero, Roser Pello, Elena Ricciardelli, Masayuki Tanaka, Laurence Tresse, Daniela Vergani, Niraj Welikala, Elena Zucca, Pascal Oesch, Umami Abbas, Luke Barnes, Rongmon Bordoloi, Dario Bottini, Alberto Cappi, Paolo Casata, Andrea Cimatti, Marco Fumana, Gunther Hasinger, Anton Koekemoer, Alexei Leauthaud, Dario Maccagni, Christian Marinoni, Henry McCracken, Pierdomenico Memeo, Baptiste Meneux, Preethi Nair, Cristiano Porciani, Valentina Presotto, and Roberto Scaramella. Mass and Environment as Drivers of Galaxy Evolution in SDSS and zCOSMOS and the Origin of the Schechter Function. , 721(1):193–221, September 2010.
- [238] S. J. Penny, K. L. Masters, R. Smethurst, R. C. Nichol, C. M. Krawczyk, D. Bizyaev, O. Greene, C. Liu, M. Marinelli, S. B. Rembold, R. A. Riffel, G. d. S. Ilha, D. Wylezalek, B. H. Andrews, K. Bundy, N. Drory, D. Oravetz, and K. Pan. SDSS-IV MaNGA: evidence of the importance of AGN feedback in low-mass galaxies. , 476:979–998, May 2018.
- [239] S. Phillipps and T. Shanks. On the variation of galaxy correlations with luminosity. , 229:621–626, December 1987.
- [240] A. Pillepich, P. Madau, and L. Mayer. Building Late-Type Spiral Galaxies by In-Situ and Ex-Situ Star Formation. *ArXiv e-prints*, July 2014.
- [241] A. Pillepich, D. Nelson, L. Hernquist, V. Springel, R. Pakmor, P. Torrey, R. Weinberger, S. Genel, J. P. Naiman, F. Marinacci, and M. Vogelsberger. First results from the IllustrisTNG simulations: the stellar mass content of groups and clusters of galaxies. , 475:648–675, March 2018.
- [242] Planck Collaboration, P. A. R. Ade, N. Aghanim, M. Arnaud, M. Ashdown, F. Atrio-Barandela, J. Aumont, C. Baccigalupi, A. Balbi, A. J. Banday, and et al. Planck intermediate results. XI. The gas content of dark matter halos: the Sunyaev-Zeldovich-stellar mass relation for locally brightest galaxies. *AA*, 557:A52, September 2013.
- [243] M. Prescott et al. Galaxy and Mass Assembly (GAMA): the red fraction and radial distribution of satellite galaxies. , 417:1374–1386, October 2011.
- [244] V. Presotto, M. Girardi, M. Nonino, A. Mercurio, C. Grillo, P. Rosati, A. Biviano, and M. Annunziatella. Intra Cluster Light properties in the CLASH-VLT cluster MACS J1206.2-0847. *ArXiv e-prints*, March 2014.
- [245] J. I. Read, M. I. Wilkinson, N. Wyn Evans, G. Gilmore, and Jan T. Kleyna. The importance of tides for the Local Group dwarf spheroidals. , 367(1):387–399, March 2006.
- [246] Martin J. Rees. Black hole models for active galactic nuclei. *Annual Review of Astronomy and Astrophysics*, 22(1):471–506, 1984.
- [247] A. E. Reines, J. E. Greene, and M. Geha. Dwarf Galaxies with Optical Signatures of Active Massive Black Holes. , 775:116, October 2013.

- [248] A. E. Reines, R. M. Plotkin, T. D. Russell, M. Mezcua, J. J. Condon, G. R. Sivakoff, and K. E. Johnson. A Candidate Massive Black Hole in the Low-metallicity Dwarf Galaxy Pair Mrk 709. , 787:L30, June 2014.
- [249] A. E. Reines, G. R. Sivakoff, K. E. Johnson, and C. L. Brogan. An actively accreting massive black hole in the dwarf starburst galaxy Henize2-10. , 470:66–68, February 2011.
- [250] A. E. Reines and M. Volonteri. Relations between Central Black Hole Mass and Total Galaxy Stellar Mass in the Local Universe. , 813:82, November 2015.
- [251] J. A. Rich, L. J. Kewley, and M. A. Dopita. Composite Spectra in Merging U/LIRGs Caused by Shocks. , 781:L12, January 2014.
- [252] M. Rocha, A. H. G. Peter, and J. Bullock. Infall times for Milky Way satellites from their present-day kinematics. , 425:231–244, September 2012.
- [253] Miguel Rocha, Annika H. G. Peter, James S. Bullock, Manoj Kaplinghat, Shea Garrison-Kimmel, Jose Oñorbe, and Leonidas A. Moustakas. Cosmological simulations with self-interacting dark matter - I. Constant-density cores and substructure. , 430(1):81–104, March 2013.
- [254] A. Rodríguez-Ardila, S. M. Viegas, M. G. Pastoriza, and L. Prato. Near-Infrared Coronal Lines in Narrow-Line Seyfert 1 Galaxies. , 579:214–226, November 2002.
- [255] Vicente Rodriguez-Gomez, Shy Genel, Mark Vogelsberger, Debora Sijacki, Annalisa Pillepich, Laura V. Sales, Paul Torrey, Greg Snyder, Dylan Nelson, Volker Springel, Chung-Pei Ma, and Lars Hernquist. The merger rate of galaxies in the Illustris simulation: a comparison with observations and semi-empirical models. , 449(1):49–64, May 2015.
- [256] J. Rodríguez Zaurín, C. N. Tadhunter, M. Rose, and J. Holt. The importance of warm, AGN-driven outflows in the nuclear regions of nearby ULIRGs. , 432:138–166, June 2013.
- [257] D. S. Rupke, S. Veilleux, and D. B. Sanders. Keck Absorption-Line Spectroscopy of Galactic Winds in Ultraluminous Infrared Galaxies. , 570:588–609, May 2002.
- [258] D. S. N. Rupke, K. Gültekin, and S. Veilleux. Quasar-mode Feedback in Nearby Type 1 Quasars: Ubiquitous Kiloparsec-scale Outflows and Correlations with Black Hole Properties. , 850:40, November 2017.
- [259] D. S. N. Rupke and S. Veilleux. The Multiphase Structure and Power Sources of Galactic Winds in Major Mergers. , 768:75, May 2013.
- [260] A. Saintonge, G. Kauffmann, C. Kramer, L. J. Tacconi, C. Buchbender, and et al. COLD GASS, an IRAM legacy survey of molecular gas in massive galaxies - I. Relations between H₂, H I, stellar content and structural properties. , 415:32–60, July 2011.
- [261] L. Sales and D. G. Lambas. Anisotropy in the distribution of satellites around primary galaxies in the 2dF Galaxy Redshift Survey: the Holmberg effect. , 348:1236–1240, March 2004.

- [262] L. Sales and D. G. Lambas. Satellite number density profiles of primary galaxies in the 2dFGRS. , 356:1045–1052, January 2005.
- [263] L. V. Sales, F. Marinacci, V. Springel, and M. Petkova. Stellar feedback by radiation pressure and photoionization. , 439:2990–3006, April 2014.
- [264] L. V. Sales, J. F. Navarro, M. G. Abadi, and M. Steinmetz. Cosmic ménage à trois: the origin of satellite galaxies on extreme orbits. , 379:1475–1483, August 2007.
- [265] L. V. Sales, J. F. Navarro, M. G. Abadi, and M. Steinmetz. Satellites of simulated galaxies: survival, merging and their relation to the dark and stellar haloes. , 379:1464–1474, August 2007.
- [266] L. V. Sales, J. F. Navarro, D. G. Lambas, S. D. M. White, and D. J. Croton. Satellite galaxies and fossil groups in the Millennium Simulation. , 382:1901–1916, December 2007.
- [267] L. V. Sales, J. F. Navarro, J. Schaye, C. Dalla Vecchia, V. Springel, and C. M. Booth. Feedback and the structure of simulated galaxies at redshift $z=2$. , 409:1541–1556, December 2010.
- [268] L. V. Sales, J. F. Navarro, J. Schaye, C. Dalla Vecchia, V. Springel, M. R. Haas, and A. Helmi. The origin of extended disc galaxies at $z=2$. , 399:L64–L68, October 2009.
- [269] L. V. Sales, M. Vogelsberger, S. Genel, P. Torrey, D. Nelson, V. Rodriguez-Gomez, W. Wang, A. Pillepich, D. Sijacki, V. Springel, and L. Hernquist. The colors of satellite galaxies in the Illustris Simulation. *ArXiv e-prints*, October 2014.
- [270] Samir Salim, R. Michael Rich, Stephane Charlot, Jarle Brinchmann, Benjamin D. Johnson, David Schiminovich, Mark Seibert, Ryan Mallery, Timothy M. Heckman, Karl Forster, Peter G. Friedman, D. Christopher Martin, Patrick Morrissey, Susan G. Neff, Todd Small, Ted K. Wyder, Luciana Bianchi, Jose Donas, Young-Wook Lee, Barry F. Madore, Bruno Milliard, Alex S. Szalay, Barry Y. Welsh, and Sukyoung K. Yi. UV star formation rates in the local universe. *The Astrophysical Journal Supplement Series*, 173(2):267–292, dec 2007.
- [271] P. Sánchez-Blázquez, R. F. Peletier, J. Jiménez-Vicente, N. Cardiel, A. J. Cenarro, J. Falcón-Barroso, J. Gorgas, S. Selam, and A. Vazdekis. Medium-resolution Isaac Newton Telescope library of empirical spectra. , 371(2):703–718, September 2006.
- [272] Isabel M. E. Santos-Santos, Julio F. Navarro, Andrew Robertson, Alejandro Benítez-Llambay, Kyle A. Oman, Mark R. Lovell, Carlos S. Frenk, Aaron D. Ludlow, Azadeh Fattahi, and Adam Ritz. Baryonic clues to the puzzling diversity of dwarf galaxy rotation curves. , 495(1):58–77, April 2020.
- [273] L. F. Sartori, K. Schawinski, E. Treister, B. Trakhtenbrot, M. Koss, M. Shirazi, and K. Oh. The search for active black holes in nearby low-mass galaxies using optical and mid-IR data. , 454:3722–3742, December 2015.
- [274] S. Satyapal, N. Abel, N. Secrest, A. Singh, and S. Ellison. Challenges in Finding AGNs in the Low Luminosity Regime. In *Active Galactic Nuclei: What’s in a Name?*, page 82, August 2016.

- [275] S. Satyapal, N. P. Abel, and N. J. Secret. Star-forming Galaxies as AGN Imposters? A Theoretical Investigation of the Mid-infrared Colors of AGNs and Extreme Starbursts. , 858:38, May 2018.
- [276] S. Satyapal, N. J. Secret, W. McAlpine, S. L. Ellison, J. Fischer, and J. L. Rosenberg. Discovery of a Population of Bulgeless Galaxies with Extremely Red Mid-IR Colors: Obscured AGN Activity in the Low-mass Regime? , 784:113, April 2014.
- [277] C. Scannapieco, M. Wadepuhl, O. H. Parry, J. F. Navarro, A. Jenkins, V. Springel, R. Teyssier, E. Carlson, H. M. P. Couchman, R. A. Crain, C. Dalla Vecchia, C. S. Frenk, C. Kobayashi, P. Monaco, G. Murante, T. Okamoto, T. Quinn, J. Schaye, G. S. Stinson, T. Theuns, J. Wadsley, S. D. M. White, and R. Woods. The Aquila comparison project: the effects of feedback and numerical methods on simulations of galaxy formation. , 423:1726–1749, June 2012.
- [278] K. Schawinski, C. M. Urry, B. D. Simmons, L. Fortson, S. Kaviraj, W. C. Keel, C. J. Lintott, K. L. Masters, R. C. Nichol, M. Sarzi, R. Skibba, E. Treister, K. W. Willett, O. I. Wong, and S. K. Yi. The green valley is a red herring: Galaxy Zoo reveals two evolutionary pathways towards quenching of star formation in early- and late-type galaxies. , 440:889–907, May 2014.
- [279] J. Schaye, R. A. Crain, R. G. Bower, M. Furlong, M. Schaller, T. Theuns, C. Dalla Vecchia, C. S. Frenk, I. G. McCarthy, J. C. Helly, A. Jenkins, Y. M. Rosas-Guevara, S. D. M. White, M. Baes, C. M. Booth, P. Camps, J. F. Navarro, Y. Qu, A. Rahmati, T. Sawala, P. A. Thomas, and J. Trayford. The EAGLE project: simulating the evolution and assembly of galaxies and their environments. , 446:521–554, January 2015.
- [280] D. J. Schlegel, D. P. Finkbeiner, and M. Davis. Maps of Dust Infrared Emission for Use in Estimation of Reddening and Cosmic Microwave Background Radiation Foregrounds. , 500:525–553, June 1998.
- [281] A. C. Seth, R. van den Bosch, S. Mieske, H. Baumgardt, M. D. Brok, J. Strader, N. Neumayer, I. Chilingarian, M. Hilker, R. McDermid, L. Spitler, J. Brodie, M. J. Frank, and J. L. Walsh. A supermassive black hole in an ultra-compact dwarf galaxy. , 513:398–400, September 2014.
- [282] M. Shirazi and J. Brinchmann. Strongly star forming galaxies in the local Universe with nebular He II λ 4686 emission. , 421:1043–1063, April 2012.
- [283] D. Sijacki, M. Vogelsberger, S. Genel, V. Springel, P. Torrey, G. F. Snyder, D. Nelson, and L. Hernquist. The Illustris simulation: the evolving population of black holes across cosmic time. , 452:575–596, September 2015.
- [284] J. Silk. Feedback by Massive Black Holes in Gas-rich Dwarf Galaxies. , 839:L13, April 2017.
- [285] J. Silk and G. A. Mamon. The current status of galaxy formation. *Research in Astronomy and Astrophysics*, 12:917–946, August 2012.
- [286] J. Silk and M. J. Rees. Quasars and galaxy formation. , 331:L1–L4, March 1998.

- [287] B. D. Simmons, C. Lintott, K. Schawinski, E. C. Moran, A. Han, S. Kaviraj, K. L. Masters, C. M. Urry, K. W. Willett, S. P. Bamford, and R. C. Nichol. Galaxy Zoo: bulgeless galaxies with growing black holes. , 429:2199–2211, March 2013.
- [288] Joshua D. Simon, Alberto D. Bolatto, Adam Leroy, Leo Blitz, and Elinor L. Gates. High-Resolution Measurements of the Halos of Four Dark Matter-Dominated Galaxies: Deviations from a Universal Density Profile. , 621(2):757–776, March 2005.
- [289] R. M. Smith, V. J. Martínez, and M. J. Graham. A Sample of Field Ellipticals. , 617:1017–1021, December 2004.
- [290] Rachel S. Somerville and Romeel Davé. Physical Models of Galaxy Formation in a Cosmological Framework. , 53:51–113, August 2015.
- [291] K. T. Soto, C. L. Martin, M. K. M. Prescott, and L. Armus. The Emission-line Spectra of Major Mergers: Evidence for Shocked Outflows. , 757:86, September 2012.
- [292] M. Sparre, C. C. Hayward, R. Feldmann, C.-A. Faucher-Giguère, A. L. Muratov, D. Kereš, and P. F. Hopkins. (Star)bursts of FIRE: observational signatures of bursty star formation in galaxies. *ArXiv e-prints*, October 2015.
- [293] H. W. W. Spoon and J. Holt. Discovery of Strongly Blueshifted Mid-Infrared [Ne III] and [Ne V] Emission in ULIRGs. , 702:L42–L46, September 2009.
- [294] V. Springel. E pur si muove: Galilean-invariant cosmological hydrodynamical simulations on a moving mesh. , 401:791–851, January 2010.
- [295] V. Springel, J. Wang, M. Vogelsberger, A. Ludlow, A. Jenkins, A. Helmi, J. F. Navarro, C. S. Frenk, and S. D. M. White. The Aquarius Project: the subhaloes of galactic haloes. , 391:1685–1711, December 2008.
- [296] V. Springel, S. D. M. White, A. Jenkins, C. S. Frenk, N. Yoshida, L. Gao, J. Navarro, R. Thacker, D. Croton, J. Helly, J. A. Peacock, S. Cole, P. Thomas, H. Couchman, A. Evrard, J. Colberg, and F. Pearce. Simulations of the formation, evolution and clustering of galaxies and quasars. , 435:629–636, June 2005.
- [297] V. Springel, S. D. M. White, G. Tormen, and G. Kauffmann. Populating a cluster of galaxies - I. Results at $[formmu]z=0$. , 328:726–750, December 2001.
- [298] Tjitske K. Starckenburg, Laura. V. Sales, Shy Genel, Christina Manzano-King, Gabriela Canalizo, and Lars Hernquist. On the Origin of Star-Gas Counterrotation in Low-mass Galaxies. , 878(2):143, Jun 2019.
- [299] D. Stern, R. J. Assef, D. J. Benford, A. Blain, R. Cutri, A. Dey, P. Eisenhardt, R. L. Griffith, T. H. Jarrett, S. Lake, F. Masci, S. Petty, S. A. Stanford, C.-W. Tsai, E. L. Wright, L. Yan, F. Harrison, and K. Madsen. Mid-infrared Selection of Active Galactic Nuclei with the Wide-Field Infrared Survey Explorer. I. Characterizing WISE-selected Active Galactic Nuclei in COSMOS. , 753:30, July 2012.
- [300] N. R. Stickley and G. Canalizo. The Evolution of Stellar Velocity Dispersion during Dissipationless Galaxy Mergers. , 747:33, March 2012.
- [301] N. R. Stickley and G. Canalizo. Stellar Velocity Dispersion in Dissipative Galaxy Mergers with Star Formation. , 786:12, May 2014.

- [302] David K. Strickland and Ian R. Stevens. Starburst-driven galactic winds - i. energetics and intrinsic x-ray emission. *Monthly Notices of the Royal Astronomical Society*, 314(3):511, May 2000.
- [303] R. A. Swaters, B. F. Madore, F. C. van den Bosch, and M. Balcells. The Central Mass Distribution in Dwarf and Low Surface Brightness Galaxies. , 583:732–751, February 2003.
- [304] T. Tal, D. A. Wake, and P. G. van Dokkum. Observations of Dark and Luminous Matter: The Radial Distribution of Satellite Galaxies around Massive Red Galaxies. , 751:L5, May 2012.
- [305] P. Taylor and C. Kobayashi. The effects of AGN feedback on present-day galaxy properties in cosmological simulations. , 448:1835–1846, April 2015.
- [306] R. Teyssier, A. Pontzen, Y. Dubois, and J. I. Read. Cusp-core transformations in dwarf galaxies: observational predictions. , 429:3068–3078, March 2013.
- [307] Aniruddha R. Thakar and Barbara S. Ryden. Formation of Massive Counterrotating Disks in Spiral Galaxies. , 461:55, April 1996.
- [308] Adam D. Thomas, Michael A. Dopita, Lisa J. Kewley, Brent A. Groves, Ralph S. Sutherland, Andrew M. Hopkins, and Guillermo A. Blanc. Interrogating Seyferts with NebulaBayes: Spatially Probing the Narrow-line Region Radiation Fields and Chemical Abundances. , 856(2):89, Apr 2018.
- [309] D. Thomas, F. Brimiouille, R. Bender, U. Hopp, L. Greggio, C. Maraston, and R. P. Saglia. A counter-rotating core in the dwarf elliptical galaxy VCC 510. , 445(1):L19–L22, January 2006.
- [310] Eline Tolstoy, Vanessa Hill, and Monica Tosi. Star-Formation Histories, Abundances, and Kinematics of Dwarf Galaxies in the Local Group. , 47(1):371–425, September 2009.
- [311] P. Torrey, M. Vogelsberger, S. Genel, D. Sijacki, V. Springel, and L. Hernquist. A model for cosmological simulations of galaxy formation physics: multi-epoch validation. , 438:1985–2004, March 2014.
- [312] James W. Trayford, Tom Theuns, Richard G. Bower, Robert A. Crain, Claudia del P. Lagos, Matthieu Schaller, and Joop Schaye. It is not easy being green: the evolution of galaxy colour in the EAGLE simulation. , 460:3925–3939, Aug 2016.
- [313] Maxime Trebitsch, Marta Volonteri, Yohan Dubois, and Piero Madau. Escape of ionizing radiation from high-redshift dwarf galaxies: role of AGN feedback. , 478:5607–5625, Aug 2018.
- [314] C. A. Tremonti, T. M. Heckman, G. Kauffmann, J. Brinchmann, S. Charlot, S. D. M. White, M. Seibert, E. W. Peng, D. J. Schlegel, A. Uomoto, M. Fukugita, and J. Brinkmann. The Origin of the Mass-Metallicity Relation: Insights from 53,000 Star-forming Galaxies in the Sloan Digital Sky Survey. , 613:898–913, October 2004.

- [315] C. Q. Trinh, E. J. Barton, J. S. Bullock, M. C. Cooper, A. R. Zentner, and R. H. Wechsler. Groups of two galaxies in SDSS: implications of colours on star formation quenching time-scales. , 436:635–649, November 2013.
- [316] V. U, A. Medling, D. Sanders, C. Max, L. Armus, K. Iwasawa, A. Evans, L. Kewley, and G. Fazio. The Inner Kiloparsec of Mrk 273 with Keck Adaptive Optics. , 775:115, October 2013.
- [317] V. U, A. M. Medling, H. Inami, L. Armus, T. Díaz-Santos, V. Charmandaris, J. Howell, S. Stierwalt, G. C. Privon, S. T. Linden, D. B. Sanders, C. E. Max, A. S. Evans, L. Barcos-Muñoz, C. W. K. Chiang, P. Appleton, G. Canalizo, G. Fazio, K. Iwasawa, K. Larson, J. Mazzarella, E. Murphy, J. Rich, and J. Surace. Keck OSIRIS AO LIRG Analysis (KOALA): Feedback in the Nuclei of Luminous Infrared Galaxies. , 871:166, February 2019.
- [318] F. Valdes, R. Gupta, J. A. Rose, H. P. Singh, and D. J. Bell. The Indo-US Library of Coudé Feed Stellar Spectra. , 152:251–259, June 2004.
- [319] F. C. van den Bosch, D. Aquino, X. Yang, H. J. Mo, A. Pasquali, D. H. McIntosh, S. M. Weinmann, and X. Kang. The importance of satellite quenching for the build-up of the red sequence of present-day galaxies. , 387:79–91, June 2008.
- [320] F. C. van den Bosch, P. Norberg, H. J. Mo, and X. Yang. Probing dark matter haloes with satellite kinematics. , 352:1302–1314, August 2004.
- [321] F. C. van den Bosch, X. Yang, H. J. Mo, and P. Norberg. The abundance and radial distribution of satellite galaxies. , 356:1233–1248, February 2005.
- [322] R. C. E. van den Bosch and P. T. de Zeeuw. Estimating black hole masses in triaxial galaxies. , 401:1770–1780, January 2010.
- [323] J. van Eymeren, C. Trachternach, B. S. Koribalski, and R.-J. Dettmar. Non-circular motions and the cusp-core discrepancy in dwarf galaxies. , 505:1–20, October 2009.
- [324] S. van Wassenhove, M. Volonteri, M. G. Walker, and J. R. Gair. Massive black holes lurking in Milky Way satellites. , 408:1139–1146, October 2010.
- [325] S. Veilleux. A search for variations of forbidden Fe VII 6087-A lines and forbidden Fe X 6375-A lines in high-ionization Seyfert galaxies. , 95:1695–1705, June 1988.
- [326] S. Veilleux, G. Cecil, and J. Bland-Hawthorn. Galactic Winds. , 43:769–826, September 2005.
- [327] M. Vogelsberger, S. Genel, D. Sijacki, P. Torrey, V. Springel, and L. Hernquist. A model for cosmological simulations of galaxy formation physics. , 436:3031–3067, December 2013.
- [328] M. Vogelsberger, S. Genel, V. Springel, P. Torrey, D. Sijacki, D. Xu, G. Snyder, S. Bird, D. Nelson, and L. Hernquist. Properties of galaxies reproduced by a hydrodynamic simulation. , 509:177–182, May 2014.
- [329] M. Vogelsberger, S. Genel, V. Springel, P. Torrey, D. Sijacki, D. Xu, G. Snyder, D. Nelson, and L. Hernquist. Introducing the Illustris Project: simulating the coevolution of dark and visible matter in the Universe. , 444:1518–1547, October 2014.

- [330] M. Vogelsberger, S. Genel, V. Springel, P. Torrey, D. Sijacki, D. Xu, G. Snyder, D. Nelson, and L. Hernquist. Introducing the Illustris Project: simulating the coevolution of dark and visible matter in the Universe. , 444:1518–1547, October 2014.
- [331] M. Volonteri. Formation of supermassive black holes. , 18:279–315, July 2010.
- [332] Jakob Walcher, Brent Groves, Tamás Budavári, and Daniel Dale. Fitting the integrated spectral energy distributions of galaxies. , 331:1–52, January 2011.
- [333] M. G. Walker and J. Peñarrubia. A Method for Measuring (Slopes of) the Mass Profiles of Dwarf Spheroidal Galaxies. , 742:20, November 2011.
- [334] J. L. Walsh, T. Minezaki, M. C. Bentz, A. J. Barth, N. Baliber, W. Li, D. Stern, V. N. Bennert, T. M. Brown, G. Canalizo, A. V. Filippenko, E. L. Gates, J. E. Greene, M. A. Malkan, Y. Sakata, R. A. Street, T. Treu, J.-H. Woo, and Y. Yoshii. The Lick AGN Monitoring Project: Photometric Light Curves and Optical Variability Characteristics. , 185:156–170, November 2009.
- [335] J. Wang, G. De Lucia, M. G. Kitzbichler, and S. D. M. White. The dependence of galaxy formation on cosmological parameters: can we distinguish between the WMAP1 and WMAP3 parameter sets? , 384:1301–1315, March 2008.
- [336] J. Wang, C. S. Frenk, J. F. Navarro, L. Gao, and T. Sawala. The missing massive satellites of the Milky Way. , page 3369, July 2012.
- [337] L. Wang, C. Li, G. Kauffmann, and G. De Lucia. Modelling and interpreting the dependence of clustering on the spectral energy distributions of galaxies. , 377:1419–1430, June 2007.
- [338] W. Wang, Y. P. Jing, C. Li, T. Okumura, and J. Han. Galaxy Clustering and Projected Density Profiles as Traced by Satellites in Photometric Surveys: Methodology and Luminosity Dependence. , 734:88, June 2011.
- [339] W. Wang, L. V. Sales, B. M. B. Henriques, and S. D. M. White. Satellite abundances around bright isolated galaxies - II. Radial distribution and environmental effects. , 442:1363–1378, August 2014.
- [340] W. Wang and S. D. M. White. Satellite abundances around bright isolated galaxies. , 424:2574–2598, August 2012.
- [341] D. F. Watson, A. A. Berlind, C. K. McBride, D. W. Hogg, and T. Jiang. The Extreme Small Scales: Do Satellite Galaxies Trace Dark Matter? , 749:83, April 2012.
- [342] S. M. Weinmann, G. Kauffmann, F. C. van den Bosch, A. Pasquali, D. H. McIntosh, H. Mo, X. Yang, and Y. Guo. Environmental effects on satellite galaxies: the link between concentration, size and colour profile. , 394:1213–1228, April 2009.
- [343] S. M. Weinmann, G. Kauffmann, A. von der Linden, and G. De Lucia. Cluster galaxies die hard. , 406:2249–2266, August 2010.
- [344] S. M. Weinmann, T. Lisker, Q. Guo, H. T. Meyer, and J. Janz. Dwarf galaxy populations in present-day galaxy clusters - I. Abundances and red fractions. , 416:1197–1214, September 2011.

- [345] S. M. Weinmann, F. C. van den Bosch, X. Yang, and H. J. Mo. Properties of galaxy groups in the Sloan Digital Sky Survey - I. The dependence of colour, star formation and morphology on halo mass. , 366:2–28, February 2006.
- [346] S. M. Weinmann, F. C. van den Bosch, X. Yang, H. J. Mo, D. J. Croton, and B. Moore. Properties of galaxy groups in the Sloan Digital Sky Survey - II. Active galactic nucleus feedback and star formation truncation. , 372:1161–1174, November 2006.
- [347] Daniel R. Weisz, Evan D. Skillman, Sebastian L. Hidalgo, Matteo Monelli, Andrew E. Dolphin, Alan McConnachie, Edouard J. Bernard, Carme Gallart, Antonio Aparicio, Michael Boylan-Kolchin, Santi Cassisi, Andrew A. Cole, Henry C. Ferguson, Mike Irwin, Nicolas F. Martin, Lucio Mayer, Kristen B. W. McQuinn, Julio F. Navarro, and Peter B. Stetson. Comparing M31 and Milky Way Satellites: The Extended Star Formation Histories of Andromeda II and Andromeda XVI. , 789(1):24, July 2014.
- [348] A. R. Wetzel, J. L. Tinker, and C. Conroy. Galaxy evolution in groups and clusters: star formation rates, red sequence fractions and the persistent bimodality. , 424:232–243, July 2012.
- [349] A. R. Wetzel, J. L. Tinker, C. Conroy, and F. C. van den Bosch. Galaxy evolution in groups and clusters: satellite star formation histories and quenching time-scales in a hierarchical Universe. , 432:336–358, June 2013.
- [350] Andrew R. Wetzel, Philip F. Hopkins, Ji-hoon Kim, Claude-André Faucher-Giguère, Dušan Kereš, and Eliot Quataert. Reconciling Dwarf Galaxies with Λ CDM Cosmology: Simulating a Realistic Population of Satellites around a Milky Way-mass Galaxy. , 827(2):L23, August 2016.
- [351] C. Wheeler, J. I. Phillips, M. C. Cooper, M. Boylan-Kolchin, and J. S. Bullock. The surprising inefficiency of dwarf satellite quenching. *ArXiv e-prints*, February 2014.
- [352] S. D. M. White and M. J. Rees. Core condensation in heavy halos - A two-stage theory for galaxy formation and clustering. , 183:341–358, May 1978.
- [353] S. D. M. White and M. J. Rees. Core condensation in heavy halos - A two-stage theory for galaxy formation and clustering. , 183:341–358, May 1978.
- [354] Simon D. M. White and Carlos S. Frenk. Galaxy Formation through Hierarchical Clustering. , 379:52, September 1991.
- [355] R. Wojtak and G. A. Mamon. Physical properties underlying observed kinematics of satellite galaxies. , 428:2407–2417, January 2013.
- [356] J.-H. Woo, T. Treu, A. J. Barth, S. A. Wright, J. L. Walsh, M. C. Bentz, P. Martini, V. N. Bennert, G. Canalizo, A. V. Filippenko, E. Gates, J. Greene, W. Li, M. A. Malkan, D. Stern, and T. Minezaki. The Lick AGN Monitoring Project: The $M_{BH} - \sigma_*$ Relation for Reverberation-mapped Active Galaxies. , 716:269–280, June 2010.
- [357] Jong-Hak Woo, Donghoon Son, and Hyun-Jin Bae. Delayed or No Feedback? Gas Outflows in Type 2 AGNs. III. , 839(2):120, Apr 2017.
- [358] A. H. Wright, A. S. G. Robotham, S. P. Driver, M. Alpaslan, S. K. Andrews, I. K. Baldry, J. Bland -Hawthorn, S. Brough, M. J. I. Brown, M. Colless, E. da Cunha,

- L. J. M. Davies, Alister W. Graham, B. W. Holwerda, A. M. Hopkins, P. R. Kafle, L. S. Kelvin, J. Loveday, S. J. Maddox, M. J. Meyer, A. J. Moffett, P. Norberg, S. Phillipps, K. Rowlands, E. N. Taylor, L. Wang, and S. M. Wilkins. Galaxy And Mass Assembly (GAMA): the galaxy stellar mass function to $z = 0.1$ from the r-band selected equatorial regions. , 470(1):283–302, September 2017.
- [359] E. L. Wright. A Cosmology Calculator for the World Wide Web. , 118:1711–1715, December 2006.
- [360] X. Yang, H. J. Mo, and F. C. van den Bosch. The Subhalo-Satellite Connection and the Fate of Disrupted Satellite Galaxies. , 693:830–838, March 2009.
- [361] D. G. York et al. The Sloan Digital Sky Survey: Technical Summary. , 120:1579–1587, September 2000.
- [362] H. J. Zahid, G. I. Dima, R.-P. Kudritzki, L. J. Kewley, M. J. Geller, H. S. Hwang, J. D. Silverman, and D. Kashino. The Universal Relation of Galactic Chemical Evolution: The Origin of the Mass-Metallicity Relation. , 791:130, August 2014.
- [363] I. Zehavi, Z. Zheng, D. H. Weinberg, M. R. Blanton, N. A. Bahcall, A. A. Berlind, J. Brinkmann, J. A. Frieman, J. E. Gunn, R. H. Lupton, R. C. Nichol, W. J. Percival, D. P. Schneider, R. A. Skibba, M. A. Strauss, M. Tegmark, and D. G. York. Galaxy Clustering in the Completed SDSS Redshift Survey: The Dependence on Color and Luminosity. , 736:59, July 2011.
- [364] D. H. Zhao, Y. P. Jing, H. J. Mo, and G. Börner. Accurate Universal Models for the Mass Accretion Histories and Concentrations of Dark Matter Halos. , 707:354–369, December 2009.